ATOMIC PROCESSES
INDUCED BY ELECTRONIC EXCITATION
IN INSULATING CRYSTALS

By

Yang Cai

A thesis submitted to
the School of Graduate Studies and Research
in partial fulfillment of the requirements
for the degree of Doctor of Philosophy

Department of Physics

University of Ottawa
Ottawa, Ontario

National Library of Canada

Acquisitions and Bibliographic Services Branch

395 Wellington Street
Ottawa, Ontario
K1A 0N4

Bibliothèque nationale du Canada

Direction des acquisitions et des services bibliographiques

395, rue Wellington
Ottawa (Ontario)
K1A 0N4

Your file Votre référence

Our file Notre référence

ISBN 0-612-15704-0

UNIVERSITÉ D'OTTAWA
UNIVERSITY OF OTTAWA

DEDICATED TO MY PARENTS

Baorong Wu and Jianhua Tsai

Abstract

We have studied two examples of atomic processes induced by electronic excitation in insulating crystals. One is the bistable defect system in CdF_2:M^{3+}, the other is the athermal halogen atom desorption.

The bistable (shallow-deep) defect systems associated with trivalent impurities (In, Ga, Y and Sc) in CdF_2 are examined. The equilibrium lattice relaxation around the defect and the wavefunction of the electron bound to the impurities are determined by minimizing the energy of the defects. The impurity-fluorine interatomic potentials determined using the electron-gas model of Gordon and Kim are used, and the defect electron is treated by the extended-ion method. In order to compare the deep and shallow states using the same discrete lattice model, a very large cluster of atoms is treated. Two groups of trivalent impurity centers are found. With In and Ga, there is a low, but clearly identified, potential barrier which separates the deep level from the shallow one. In Sc and Y, only a simple shallow level state is obtained. The analysis of the result shows that the difference is to be attributed to the short-range potential of the trivalent impurity centers. On the basis of present work, we predict that Tl^{3+} would exhibit similar bistable behaviour.

Energetic halogen atom desorption observed from certain alkali halide crystal under electron or photon stimulation is being investigated. The relaxed structure of the localized one-center (Frenkel-type free exciton) and two-center (self-trapped exciton: STE) electronic excitations are studied. It is shown that the triplet STE state undergoes an instability on and near the surface similar to that in the bulk. For the first and second layers' STE below the (100) surface, the excited electron localizes with preference closer to the surface. Further below, there is no preference. Only when the off-center relaxation of the STE propels Br_2^- toward the surface can there be a desorption. The third layer STE in KBr leads to desorption with a possible kinetic energy of about 1 eV, the trajectory undergoes deviation as the ejected Br^0 clears the surface. In NaBr, the APES of third layer's STE encounters a barrier as in the bulk, no energetic desorption is expected in NaBr as the experiment shows. The presence of a In^+ adjacent to a STE in the third layer, on the side closer to the surface, results in the excited electron localizing on the Br site nearer to the surface and on In^+, pushing the V_k center deeper into the

bulk. We believe that this causes the observed inhibition of Br^0 desorption in In-doped KBr. In CaF_2, though the excited electron localizing on the surface for the first layer's STE below the (111) surface, the F atom desorption is still expected due to the different lattice structure with the ejecta's trajectory undergoing correction to approach the normal of the surface.

In all the examples studied here, the large atomic displacement is induced by the excited electron.

Acknowledgements

I feel privileged to have had this opportunity to express my great thanks to Dr. K.S. Song for making my dream to study in Canada and to get a Ph.D. degree come true, and for all of his help, encouragement and support during my studies.

I would like to thank Professor L.F. Chen for his constructive discussion and tutoring.

I would like to thank Dr. G. Slater for providing me the values of zero points and weight factors of Gauss-Laguerre polynomials of order 80.

I would like to thank Mr. Ronald Marshall for taking time to polish the English writing of this thesis.

I would also like to thank Nanjing University, where I got my B.Sc. and M.Sc. degrees, and Nanjing Normal University, where I worked for five years.

Thanks to all the professors and support stuff of the department. Thanks to all my friends.

Contents

List of Tables

List of Figures

Part I

Bistable Defect System

Chapter 1. Introduction

Cadmium fluoride, CdF_2, has the well-known fluorite structure as shown in Fig. 1.1. It's Bravais lattice is FCC with a basis of three ions, Cd^{2+} at (0,0,0) and two F^-s at (1/4, 1/4, 1/4) and (3/4, 3/4, 3/4), respectively. The fluorine atoms are on the corners of a cube with the body-centered interstitial site occupied by a cadmium atom or empty alternatively. Thus the fluorine atoms have tetrahedral coordination with the cadmiums while the cadmium atoms have octahedral coordination with the fluorines. The lattice constant, a_0, is 5.365 Å [1], which is the unit cell dimension, twice the length of the cube. The pure crystal is highly insulating with a resistivity of the order of $10^7\Omega$-cm at room temperature, and has a large band gap E_G=6.0eV [2].

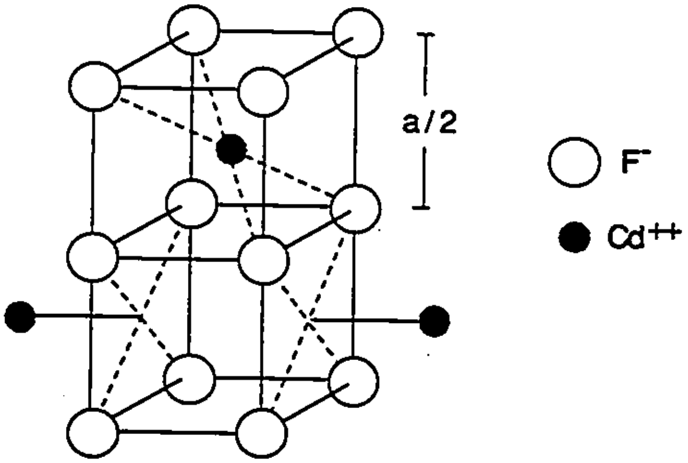

Figure 1.1: Fluorite Crystal Structure

CdF_2 has been doped with numerous trivalent dopants, such as Sc, Y and rare earth (RE) ions. If the dopants are introduced into the system in the form of trifluorides, an extra fluorine ion, F^-, which occupies the interstitial site, will be in the lattice to compensate for the extra charge of each trivalent dopant present to maintain neutrality. The bulk properties of the system are qualitatively unchanged for low-dopant concentrations, 0.1% or less. In 1961 Kingsley and Prenner [3, 4] discovered that when trivalent metal doped CdF_2 is annealed in cadmium-metal vapour the insulating and transparent crystal becomes semiconducting (n-type) and coloured, with the resistivity decreasing to $1\Omega\cdot$cm. They concluded that during the thermal annealing the interstitial fluorines, which were compensating the trivalent dopant, diffused to the surface and combined with the Cd metal to form molecules. Two electrons were liberated into the crystal for each CdF_2 molecule formed on the surface. It is those electrons which are thought to give the semiconducting state. At low concentration of dopants, 0.1% or less, the dopant-dopant distance is much larger than the lattice constant. The lattice configuration consists of an isolated trivalent ion with an electron around it.

Most of the trivalent metals in CdF_2 produce stable shallow hydrogenic donor states [2, 6]. Among the trivalent dopants, In [7, 8, 9, 10] and Ga [11] have shown unusual bistable behaviour. In room temperature absorption spectra of $CdF_2{:}In^{3+}$ two strongly asymmetric bands are seen (Fig. 1.2). One of these is in the visible light range (VIS), peaked at 3.2 eV, and another in the mid-infrared (IR), at about 0.2 eV. The IR band, which is similar to that observed for the stable shallow Y donor [12, 13], is attributed to the photoionization of shallow donors. For the VIS band, the photoconductivity cross section has the identical shape as the VIS absorption band, thus proving its photoionization origin. At low temperature, after

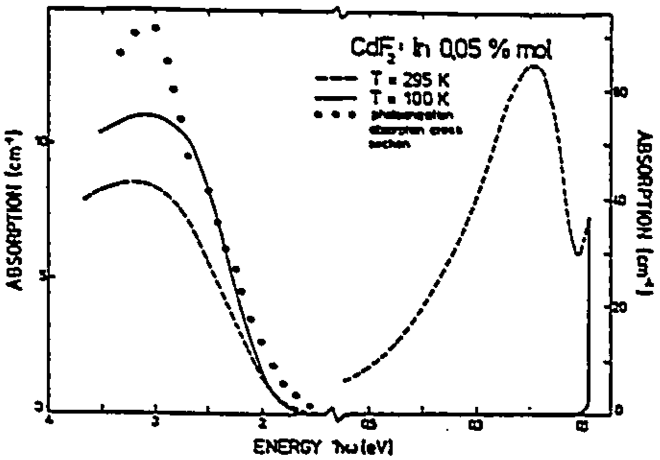

Figure 1.2: Absorption Spectrum of CdF_2:In^{3+}

From U. Piekara *et al.* [5]. Note a change in the energy scale.

cooling the crystal in darkness, only the 3-eV band is seen; while after illuminating the crystal with light near the VIS band, the 0.2-eV band increases at the expense of the 3-eV band until its complete bleaching. J.E. Dmochowski and J.M. Langer *et al.* [10] concluded that the 0.2-eV band indicates a weakly localized $In^{3+}+e^-$ state, and the 3-eV band a localized In^{2+} state. The optical and thermal ionization energies corresponding to these two ground states and the energy barrier separating them are listed in Table 1.1. From the table it is clear that the ground In^{2+} state is very localized because of the enormous Stokes shift (E_{opt}-E_{th}=1.7eV). The absorption spectra of CdF_2:Ga^{3+} has similar asymmetric bands peaked at 4 eV and 0.17 eV, respectively [11] (Fig 1.3). It is believed that Ga is a second bistable impurity center in CdF_2, but details haven't been published.

Table 1.1: Experimental Results for CdF_2:In^{3+}

band	state	optical ionization energy (eV)	thermal ionization energy (eV)	barrier (eV)
IR	$In^{3+}+e^-$	0.18[a]	0.14	
VIS	In^{2+}	1.9	0.25	0.17

[a] From F. Trautweiler *et al.* [8]. Other data are from U. Piekara *et al.* [5]. All thermal energies refer to 0 K. The energy barrier is slightly temperature dependent, this is the value at 100 K.

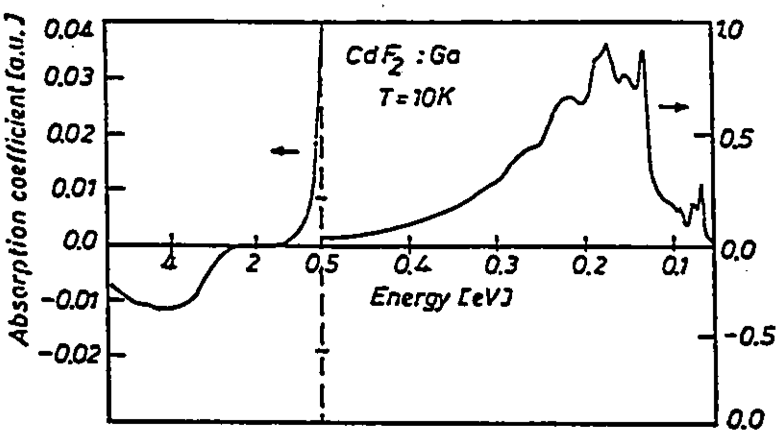

Figure 1.3: Absorption Spectrum of CdF_2:Ga^{3+}

From J.E. Dmochowski *et al.* [11]. Note a change in the energy scale.

The unusual behaviour of In donors in CdF_2 crystal has shown for the first time experimentally that an electron can be bound by a defect on either a very localized orbit or a delocalized one. These two states are separated by a vibronic barrier which results from a drastic change in localization during electron transfer between these two states. The most general framework for the theoretical description of bistability occurring in crystal defects has been developed by Toyozawa [14]. The main point of Toyozawa's model is that all the electron states in solids are either strongly localized (self-trapping, S type) or delocalized (free, F type in Toyozawa's notation). In the case of an electron bound to a charged impurity, the electron always has a delocalized shallow state and in addition many have a localized deep minimum stabilized by combined action of the impurity potential and the electron-phonon interaction. If the thermal ionization energies for these two states are of the same order, then they should be separated by a barrier. Bistability here is produced by the same center in either highly localized or delocalized orbits. The discontinuity in localization results from the competition between the long-range (Coulombic) and short-range (electron-phonon coupling) forces [15].

Based on a simple configuration coordinate (c.c.) model, Piekara and Langer [5] have presented a qualitative description of the lattice relaxation around the In^{3+} impurity center in the shallow and deep levels. Fig 1.4 shows the configuration-coordinate diagram of In impurity in CdF_2, where the configuration-coordinate Q represents a relative position of the ions surrounding In impurity. When $In^{3+}+e^-$ shallow donor is ionized, the equilibrium configuration does not change (Q_s position), there is no or only a very small difference between optical and thermal ionization energies for this state. The situation is quite different when the localized In^{2+} state is ionized. During the thermal ionization both the configuration coordinate and

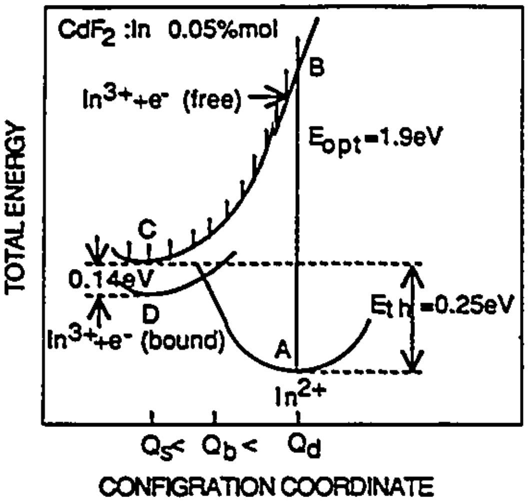

Figure 1.4: Configuration-Coordinate Diagram of In Impurity in CdF_2

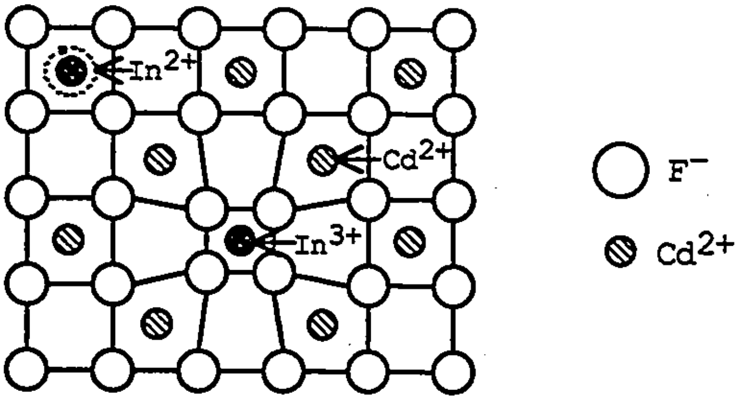

Figure 1.5: Microscopic Model for CdF_2:M^{3+}

electron wavefunction change ($Q_d \rightarrow Q_s$, the wavefunction becomes delocalized). The thermal ionization energy is small. The optical ionization of localized In^{2+} state is a Franck-Condon transition. Therefore, the optical ionization energy is much larger compared with the thermal ionization energy (large Stokes shift). An immediate consequence of the proposed model is the bistability of the photoinduced state at low temperature. After cooling the crystal in darkness, the defect system will be in the localized In^{2+} level (the lowest state, A). Absorption occurs primarily to B, the ionized state with the same configuration as in A. So that only the 3-eV band will be seen. When the system is in state B, nonradiative processes occur rapidly, the system relaxes irreversibly to C, the bottom of the ionized state. Since the minimum of a parabola of the shallow state lies outside a parabola of the In^{2+} state, a potential barrier at Q_b causes In^{3+}+e^- shallow level to be bistable at very low temperature.

Dmochowski and Langer *et al.*.[16] have also introduced a microscopic model to describe the lattice distortion in the shallow and deep levels. It is expected that there is a symmetric, local lattice collapse in the shallower M^{3+} state due to a change of the core screening after ionization of the defect, and that the lattice position in the deeper M^{2+} state remains almost the same as in the perfect lattice (Fig 1.5).

In this work, we present a study of the structure of the M^{3+} impurity with an excited electron bound to it (with M=In, Ga, Sc and Y). Both In (Ga) and Y (Sc) are trivalent impurities in the same row. We shall attempt to study the mechanism which leads to the different behaviours of stable Y (Sc) and bistable In (Ga) donors. The discrete structure of the lattice and detailed interaction between the excited electron and the impurity atom as well as the surrounding atoms of

Cd^{2+} and F^- are explicitly taken into account within the approach of the extended-ion method. In order to compare the shallow and deep level states on the same footing, an identical treatment is applied to both states. The interaction of the electron with the surrounding atoms is represented as in a one-electron Hartree-Fock approach. The energy of the distorted lattice is made up of the electrostatic Coulomb energy, which we calculated by interpolating the Madelung potential, and the short range repulsive interaction of the ion core, which we represent using the Born-Mayer potential. The polarization energy is calculated for ionic displacement explicitly up to the 4^{th} shell by relaxing ions, and for the electronic polarization by using point dipole model upto about 500 atoms. The adiabatic potential energy is determined as a function of the c.c. chosen (the nearest M^{3+}-F^- distance) by minimizing the total energy of the defect system. The defect electron is represented by a linear combination of several floating Gaussians (FGO) which can represent both a diffuse and a compact state.

As expected, we find a strongly relaxed lattice environment (relative to a perfect lattice without impurities) associated with the shallow (diffuse electron wavefunction) level, and an almost undistorted lattice environment for the deep (compact state) level. The most significant result is that the short range potential of the impurity atom core plays an important role in the appearance of the bistable state, the lack of the deep level for Y and Sc donors seems due to internal differences of the two groups of trivalent atoms.

We will describe the method used and the parameters fitted in Chapter 2 and then present and discuss the results of our calculations in Chapter 3.

Chapter 2. Method of Calculation

In this study the principal task is to determine the adiabatic potential energy of the defect system. It is therefore assumed throughout that ions move more slowly than the defect electron. Because of the symmetry, ions around the impurity move radially. So that we calculate the total energy as a function of the position of ion shells around the impurity. The total energy is taken to be the sum of:

(i) the electrostatic Coulomb energy of the ions in the lattice;
(ii) the short range repulsive energy between ions;
(iii) the energy of the defect electron;
(iv) the polarization energy of the crystal.

As our principal interest is in determining the structure, both electronic and lattice, of the defect system, we minimize the total energy with regard to the chosen configuration coordinate (c.c. hereafter). In this way we find either a bistable or simple stable defect level. The choice of the c.c. usually depends on the nature of the problem. In our work the ions of the first 3 shells around the impurity are allowed to move.. The c.c. is the nearest M^{3+}-F^- distance, i.e. the distance between the impurity and the first F^- shell around it. Corresponding to each value of the c.c., the next 2 shells' ions are allowed to relax to give the lowest adiabatic potential energy.

We consider the interaction of the defect with a cluster of about 1800 ions surrounding the impurity in calculating the electron energy, since the wavefunction of the shallow level is very diffuse. Though such a large cluster is not necessary for a deep state, to be consistent this large cluster is used for both the shallow and the deep state. And we consider the interaction of the defect with a cluster of about 500 ions for calculating the polarization energy, the cluster is chosen such that the energy converges in this region. We take the zero of energy to be the energy of the perfect lattice, the perfect lattice being all ions at their undisplaced positions and without the impurity. The energy which is evaluated is therefore the change in the various terms relative to the zero described above.

2.1 Lattice Coulomb Energy

The electrostatic Coulomb energy is calculated by considering an infinite lattice of point charges. The lattice Coulomb energy is the sum of the Madelung energy of all the individual ions. Care must be taken so as not to double count interactions.

For ions that remain at their perfect lattice sites the potential is simply the Madelung constant α_M divided by the nearest-neighbour distance. For ions that have been displaced from their perfect lattice sites, the Madelung potential is expanded in cubic harmonics. This is to replace the slowly converging Coulomb potential

$$V(\vec{r}) = \sum_i \frac{q_i}{|\vec{r} - \vec{R}_i|} \tag{2.1}$$

by a rapidly convergent sum over cubic harmonics:

$$V(\vec{r}) = \sum_{l=0}^{\infty} \frac{e}{d_{nn}} b_l Y_l(\theta_r, \phi_r) \left(\frac{r}{d_{nn}}\right)^l . \tag{2.2}$$

Where $\vec{R}_i$ and q_i are the lattice site and charge of ion i, respectively, d is the nearest-neighbour cation-anion distance, b_l are the coefficients specific to a given lattice structure, and $Y_l(\theta_r, \phi_r)$ are cubic harmonics of order l. Then this potential

Table 2.1: Madelung Potential Interpolation Coefficients

Coefficient	Cation Site	Anion Site	B.C.I. Site
b_0	-3.276110	1.762675	-0.249239
b_3	0.000000	21.603238	0.000000
b_4	1.399145	-2.270779	3.142413
b_6	-0.483126	0.392747	-0.302367
b_7	0.000000	-11.830096	0.000000
b_8	-0.278946	0.077396	0.124153
b_{10}	0.267278	0.000000	0.319207

Madelung potential interpolation coefficients for fluorite structure (atomic units). B.C.I. means body-centered interstitial site.

produced by an infinite lattice can be interpolated in any general direction using one set of coefficients and therefore be calculated at any point within the unit cell.

The interpolation formula assumes that all other ions are at their perfect lattice sites, so that the interpolated potential is corrected for the displacement of the other ions that have been moved. The corrected energy is calculated and added to the total. The coefficients for the flourite structure employed here are listed in Table 2.1.

2.2 Repulsive Energy

For the short range repulsive interactions of ions we use a Born-Mayer type potential,

$$V_{ij} = A_{ij} exp(-r/\rho_{ij}) \tag{2.3}$$

for cation-anion pairs and a Buckingham potential, which includes a van der Waals part

$$V_{--} = A_{--} exp(-r/\rho_{--}) - C_{--}/r^6 \tag{2.4}$$

for anion-anion pairs. The F^--F^- interaction is apparently attractive at large interionic separations [17, 18]. Where r is the separation of ions i and j, A_{ij}, ρ_{ij}, A_{--}, ρ_{--} and C_{--} are constants characteristic of each pair. The cation-cation interaction has been excluded since the distance between positive ions is much larger than the cation-anion separation. Also, the ionic radius of the cations is smaller than that of the anions. The short range repulsion is obtained by summing the potentials over the nearest neighbours of the ion being moved.

A major difficulty with interionic potentials is that there is no crystal data for the impurity-fluorine potential. Gordon-Kim's [19] semiclassical treatment, in which the interactions between closed-shell atoms and molecules were successfully calculated in the regions both of the attractive well and of the repulsive wall at shorter distances, enables one to readily determine the repulsive energy versus distance assuming that there is no bond formation.

It has been established that the binding in CdF_2 crystal is largely ionic. In such a crystal, the ions can be considered to be free ions for the purpose of calculating the repulsive interactions between constituents. First Cd^{2+}, F^-, In^{3+}, Y^{3+}, Ga^{3+} and Sc^{3+} charge distributions were calculated with the SCF (self consistent field) program based on the Hartree-Fock-Roothan method. And then the interionic potentials were determined with Gordon-Kim approach and fitted to the form of Born-Mayer potential for cation-anion pairs or Buckingham potential for anion-anion pairs. The results are presented in Table 2.2 and Fig. 2.1.

As in Ref. [20] it is assumed that there exists a relation between A_i and the ionic radius of trivalent r_i

$$A_i \approx (r_i + r_F)^{-2} exp[(r_i + r_F)/\rho] \;, \tag{2.5}$$

where r_F is the F^- ionic radius; ρ is a constant for these trivalent ions. From Fig. 2.1

Table 2.2: Born-Mayer Pair Potential Coefficients

Ion Pairs	$A(a.u.)$	$\rho(a.u.)$	$C(a.u.)$
Cd^{2+}-F^-	257.76	0.4641	
In^{3+}-F^-	263.30	0.4583	
Y^{3+}-F^-	230.86	0.4654	
Ga^{3+}-F^-	133.17	0.4709	
Sc^{3+}-F^-	159.16	0.4605	
F^--F^-	61.901	0.5202	23.771

The fitting formula $V = A\ exp(-r/\rho)$ is applied for metal-fluorine short range interaction, and $V = A\ exp(-r/\rho) - C/r^6$ for fluorine-fluorine interaction. A, ρ and C are in atomic units.

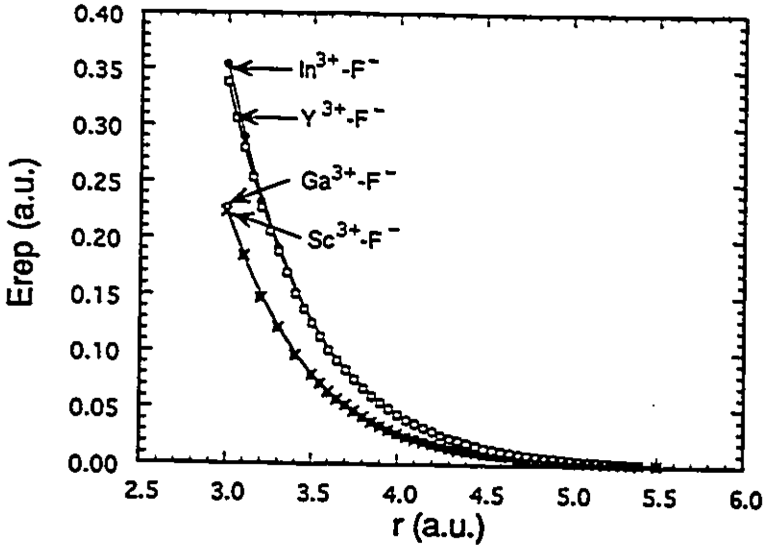

Figure 2.1: Interionic Potentials of M^{3+}-F^-

M=In, Ga, Y and Sc. The potentials are obtained with Gordon-Kim [19] method.

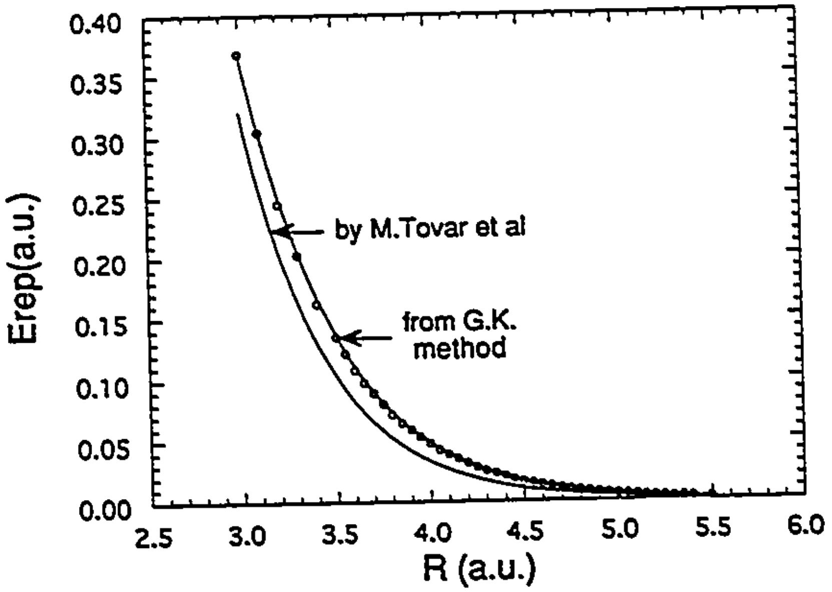

Figure 2.2: Interionic Potentials of Cd^{2+}-F^-

Cd^{2+}-F^- interionic potential of present work obtained with Gordon-Kim [19] method and the one by M. Tovar *et al.* [20] from the lattice parameter and elastic constants.

one can see that the potential curves of In^{3+}-F^- and Y^{3+}-F^- are almost the same, and so are those of Ga^{3+}-F^- and Sc^{3+}-F^-. From Table 2.2 one can see that all the impurities have quite close ρ's, and In^{3+} and Y^{3+} have about the same A_i for they are of about the same size, so do Ga^{3+} and Sc^{3+}.

Tovar, Ramos and Fainstein [20] calculated the coefficients of cadmium fluoride from the elastic constants. Their results and our calculations are listed in Table 2.3. Also Fig. 2.2 and Fig. 2.4 show some interionic potentials of Cd^{2+}-F^-, F^--F^- and Y^{3+}-F^- with various different methods.

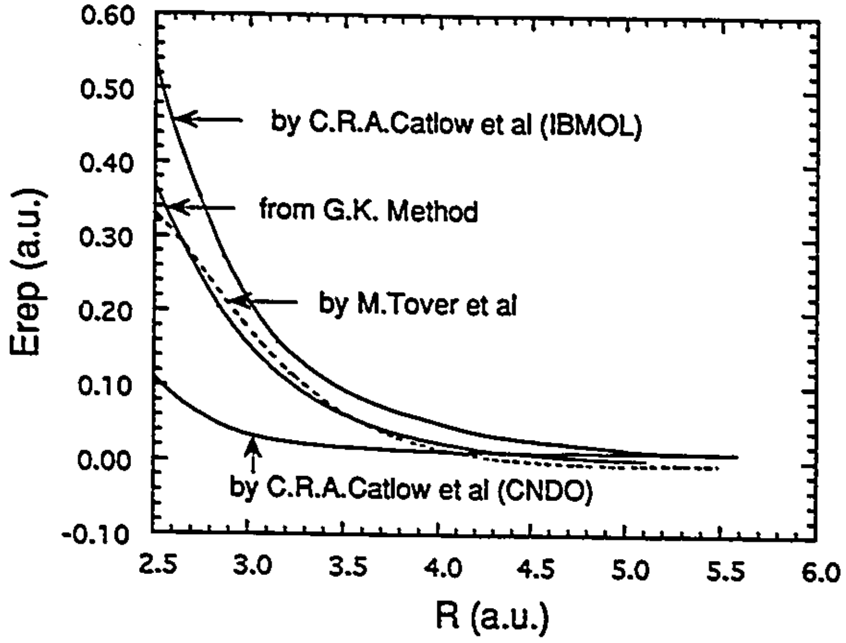

Figure 2.3: Interionic Potentials of F$^-$-F$^-$

F$^-$-F$^-$ interionic potential of present work obtained with Gordon-Kim [19] method and those obtained by M. Tovar *et al.* [20] and by C.R.A. Catlow *et al.* [21]. In the work of C.R.A. Catlow *et al.*, two methods were used which are semiempirical CNDO (Complete Neglect of Differential Overlap) and Hartree-Fock (IBMOL V program for *ab initio* calculations).

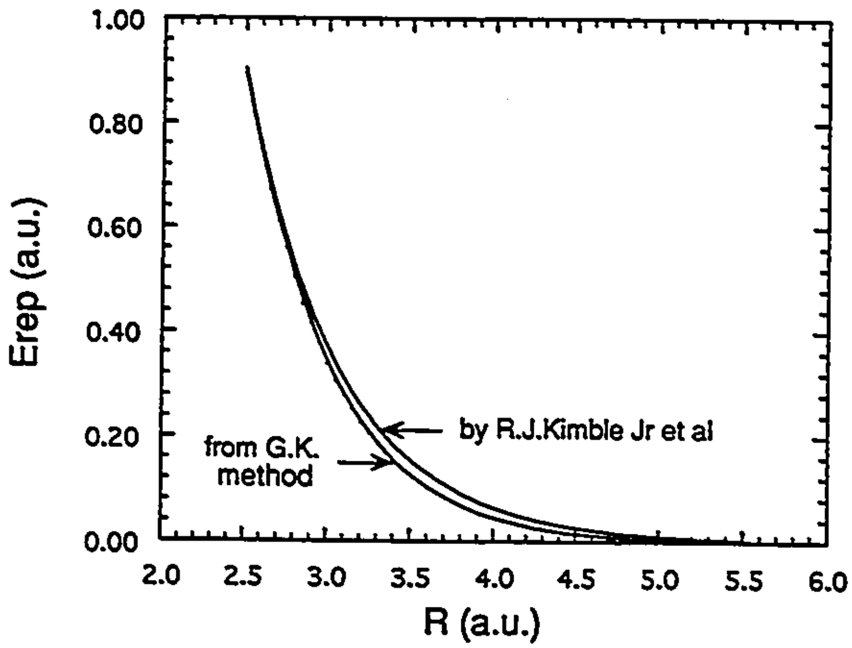

Figure 2.4: Interionic Potentials of Y^{3+}-F^-

Y^{3+}-F^- interionic potential of present work obtained with Gordon-Kim [19] method and the one by R.J. Kimble Jr *et al.* [22], in which the Born-Mayer pair potential coefficient of Y^{3+}-F^- is taken to be the same as the one of Er^{3+}-F^- according to the relationship shown in equation 2.5 and about the same ionic size of Y^{3+} and Er^{3+}, the coefficient of Er^{3+}-F^- is computed using dielectric relaxation techniques and shell model potentials.

Table 2.3: Born-Mayer Coefficients of Cd^{2+}-F^- and F^--F^- from Different Methods

	Cd^{2+}-F^-		F^--F_-		
(atomic units)	A_{ca}	ρ_{ca}	A_{aa}	ρ_{aa}	C
Tovar, Ramos & Fainstein [20]	287.98	0.4412	160.62	0.5204	241.09
Present work (G-K method)	257.76	0.4641	61.901	0.5202	23.771

Subscript "*ca*" stands for cation-anion, and "*aa*" for anion-anion. All values are in atomic units.

To test the short range pair potential parameters listed above (Table 2.3), the elastic constants [1] of the crystal were evaluated using the relations given in Ref. [17]. The relationships are:

$$\beta^{-1} = \frac{1}{3r_0}[(A_1 + 2B_1) + (A_2 + 2B_2)] , \tag{2.6}$$

$$C_{11} = \left[\frac{1}{3}(A_1 + 2B_1) + A_2 - 3.05120 Z_1 Z_2 \left(\frac{e^2}{2v}\right)\right] / r_0 , \tag{2.7}$$

$$C_{12} = \left[\frac{1}{3}(A_1 - B_1) + 3.46510 Z_1 Z_2 \left(\frac{e^2}{2v}\right)\right] / r_0 , \tag{2.8}$$

$$C_{44} = \left[\frac{1}{3}(A_1 + 2B_1) + B_2 + 1.52560 Z_1 Z_2 \left(\frac{e^2}{2v}\right)\right] / r_0 . \tag{2.9}$$

Where β is the compressibility, C_{11}, C_{12} and C_{44} are three independent second-order elastic moduli of cubic metal fluorites; Z_1 and Z_2 are net charges of the cation and anion, respectively; e is the electron charge; $r_0 = a_0/2$ is the nearest fluorine-fluorine distance, and $v = 2r_0^3$ is the unit-cell volume, a_0 is the lattice constant; A_1, B_1, A_2

and B_2 are defined as following:

$$A_1 = \left(\frac{e^2}{2v}\right)^{-1} \left|\frac{\partial^2 \phi_1(r')}{\partial r'^2}\right|_{r'=r'_0} = \frac{A_{ca}}{\rho_{ca}^2} e^{-r'_0/\rho_{ca}} , \tag{2.10}$$

$$B_1 = \left(\frac{e^2}{2v}\right)^{-1} \left|\frac{1}{r'}\frac{\partial \phi_1(r')}{\partial r'}\right|_{r'=r'_0} = -\frac{A_{ca}}{r'_0 \rho_{ca}} e^{-r'_0/\rho_{ca}} , \tag{2.11}$$

$$A_2 = \left(\frac{e^2}{2v}\right)^{-1} \left|\frac{\partial^2 \phi_2(r)}{\partial r^2}\right|_{r=r_0} = \frac{A_{aa}}{\rho_{aa}^2} e^{-r_0/\rho_{aa}} - 42\frac{C}{r_0^8} , \tag{2.12}$$

$$B_2 = \left(\frac{e^2}{2v}\right)^{-1} \left|\frac{1}{r}\frac{\partial \phi_2(r)}{\partial r}\right|_{r=r_0} = -\frac{A_{aa}}{r_0 \rho_{aa}} e^{-r_0/\rho_{aa}} + 6\frac{C}{r_0^8} , \tag{2.13}$$

where $r'_0 = \frac{\sqrt{3}}{4}a_0$ is the nearest metal-fluorine distance; A_{ca} and ρ_{ca} as well as A_{aa}, ρ_{aa} and C are the Born-Mayer coefficients for cation-anion and anion-anion pairs, respectively; and

$$\begin{aligned} \phi_1(r') &= A_c e^{-r'/\rho_c} , \\ \phi_2(r) &= A_a e^{-r/\rho_a} - \frac{C}{r^6} . \end{aligned}$$

The fitted elastic constants are listed in Table 2.4, which can be used as a rough evaluation of the pair potential coefficients. Note that even those coefficients which are deduced from the elastic constants do not give very good fit in terms of the formulae given above.

Table 2.4: Fitting of the Elastic Constants

$a_0 = 10.142(a.u.)$	Experiment	Tovar, Ramos & Fainstein	Present work
$\beta(10^{-12}$ cm^2/dyn)	0.873	0.768	0.653
$C_{11}(10^{11}$ dyn/cm^2)	19.79	20.99	24.01
$C_{12}(10^{11}$ dyn/cm^2)	7.29	11.14	11.48
$C_{44}(10^{11}$ dyn/cm^2)	2.49	9.04	9.70

Elastic constants for CdF_2 crystals fitted from the Born-Mayer pair potential coefficients obtained with different methods. The experimental data are from Pederson and Brewer [1].

2.3 Electron Energy

The many e^- formulation of a defect in ionic crystal presents several major problems, which include solving Hartree-Fock equations of a large number of electrons in the cluster of atoms and the defect; taking care of the ions outside the cluster; working on the problem at the boundary of the cluster; and minimizing the total energy by relaxing the cluster of atoms. A significant simplification has been applied by using the one electron approach for the defect electron, since the core orbitals are not expected to change significantly in the presence of a defect. In insulators with wide forbidden energy gaps, certain defect electrons occupy excited state orbitals which are more diffuse than all of the occupied state orbitals. The F center electron in ionic crystals and the excited electron of the self-trapped exciton (STE) are examples of this. The extended-ion approach has been developed for such systems. "Extended-ion" implies that the method was formulated as an improvement on the "point ion" approximation [23], in which any reference to the structure of atoms was neglected.

Instead of solving the coupled Hartree-Fock equations for all the electrons of the system, the extended-ion method addresses only the Hartree-Fock equations representing the defect electron. The other electrons, which are deeper in energy and in more compact valence band and core orbitals, are assumed to be the same as in the perfect crystal, and therefore assumed to be known. This approach is sometimes known as the "one-electron Hartree-Fock" method, because the other electrons merely contribute to the potential seen by the defect electron, and there is no iterative procedure to reach self-consistency as in the full Hartree-Fock procedure. A suitable form of the basis function is chosen and then it is orthogonalized to all occupied state wavefunctions. Using this orthogonalized basis function, the one-electron Hartree-Fock equation is solved variationally. In this approach, besides the overlap integrals required by the orthogonalization, the screened Coulomb energy and exchange integrals between the defect electron and all the core orbital electrons have to be evaluated.

Earlier a versatile version of the extended-ion method [24, 25, 26, 27] has been developed. The interaction of the electron with the deep core orbital of the lattice ions is treated with the ion-size parameters originally formulated by Bartram *et al.* [28, 29], while the outer *s*, *p*, and *d* orbital are calculated directly through interpolation formulae. The use of floating 1*s* Gaussian orbital (FGO) makes it practical to evaluate various short range terms (screened Coulomb, exchange and overlap integral) efficiently. It also gives us the required flexibility to place the Gaussian centers at appropriate positions in the crystal to best represent the defect electron states.

We start from the Schrödinger equation

$$H\Psi = E\Psi \ , \tag{2.14}$$

$$H = -\frac{1}{2}\nabla^2 + V_{pi}(\vec{r}) + V_{sc}(\vec{r}) + V_{ex}(\vec{r}) \,. \tag{2.15}$$

Where V_{pi}, V_{sc} and V_{ex} are point ion potential, screened Coulomb potential and exchange potential, respectively,

$$\begin{aligned} V_{pi}(\vec{r}) &= -\sum_{\gamma}\frac{\tilde{Z}_\gamma}{|\vec{r}-\vec{R}_\gamma|} \,, \\ V_{sc}(\vec{r}) &= -\sum_{\gamma}\frac{Z_\gamma - \tilde{Z}_\gamma}{|\vec{r}-\vec{R}_\gamma|} + \sum_{\gamma,\lambda}{}' \langle\chi_{\gamma,\lambda}(\vec{r}_1)|\frac{1}{|\vec{r}-\vec{r}_1|}|\chi_{\gamma,\lambda}(\vec{r}_1)\rangle \,, \\ V_{ex}(\vec{r}) &= -\sum_{\gamma,\lambda}{}' |\chi_{\gamma,\lambda}(\vec{r})\rangle\frac{1+\vec{\sigma}_1\cdot\vec{\sigma}_2}{2|\vec{r}-\vec{r}_1|}\langle\chi_{\gamma,\lambda}(\vec{r}_1)| \,. \end{aligned} \tag{2.16}$$

$\vec{r}$ is the defect electron position vector, $\vec{R}_\gamma$ is the γth lattice site, $\chi_{\gamma,\lambda}$ is the λth occupied atomic orbital on the γth atom, Z_γ is the nuclear charge, $\tilde{Z}_\gamma$ is the total charge of the ion or atom. The summation in γ includes all the lattice sites. Atomic units ($e = \hbar = m = 1$) are used throughout.

$\sum'$ means summing over all states with different spins. For a pair of electron with same γ, λ, but different σ: $\vec{\sigma}_1 \cdot \vec{\sigma}_2 = -1$, the exchange term is zero, and the Coulomb term remains the same. So it can be summed over all states with the same spin

$$\begin{aligned} V_{sc}(\vec{r}) &= -\sum_{\gamma}\frac{Z_\gamma - \tilde{Z}_\gamma}{|\vec{r}-\vec{R}_\gamma|} + 2\sum_{\gamma,\lambda}\langle\chi_{\gamma,\lambda}(\vec{r}_1)|\frac{1}{|\vec{r}-\vec{r}_1|}|\chi_{\gamma,\lambda}(\vec{r}_1)\rangle \,, \\ V_{ex}(\vec{r}) &= -\sum_{\gamma,\lambda}|\chi_{\gamma,\lambda}(\vec{r})\rangle\frac{1}{|\vec{r}-\vec{r}_1|}\langle\chi_{\gamma,\lambda}(\vec{r}_1)| \,. \end{aligned} \tag{2.17}$$

The defect electron wave function Ψ is expected to have much the same oscillatory behavior in the regions of surrounding ions as the ion core functions, we thus replace Ψ by a pseudo-wavefunction ψ, which is orthogonal to all the ionic orbitals

$$|\psi\rangle = |\phi\rangle - \sum_{\gamma,\lambda} |\chi_{\gamma,\lambda}\rangle\langle\chi_{\gamma,\lambda}|\phi\rangle \ . \tag{2.18}$$

Since ϕ is arbitrary, one is allowed to impose constraints on it such as the requirement that ϕ be a smooth function, slowly varying in the region of the core orbitals. (We will see this is required in the ion size parameters below.) We use a linear combination of floating 1s Gaussians ($e^{-\alpha r^2}$) to represent ϕ, since we can calculate various terms of equation 2.15 analytically, and treat as many different symmetries of excited states as we want by placing Gaussian bases judiciously on or around the defect center.

Therefore we have

$$\phi = \sum_i c_i \phi_i = \sum_i c_i \left(\frac{2\alpha_i}{\pi}\right)^{\frac{3}{4}} e^{-\alpha_i|\vec{r}-\vec{R}_i|^2} \ , \tag{2.19}$$

where ϕ_i is a normalized Gaussian, α_i is the Gaussians' exponent and $\vec{R}_i$ is the Gaussians' position, both are parameters to be optimized. c_i's are the coefficients of the linear combination which are found when the secular determinant is solved.

The problem now is solving the secular equation for the state ϕ and its energy E:

$$|H_{ij} - ES_{ij}| = 0 \ , \tag{2.20}$$

where

$$\begin{aligned} H_{ij} &= \langle\phi_i|H|\phi_j\rangle - \sum_{\gamma,\lambda}\langle\phi_i|H|\chi_{\gamma,\lambda}\rangle\langle\chi_{\gamma,\lambda}|\phi_j\rangle - \sum_{\gamma,\lambda}\langle\phi_i|\chi_{\gamma,\lambda}\rangle\langle\chi_{\gamma,\lambda}|H|\phi_j\rangle \\ &\quad + \sum_{\gamma,\lambda}\sum_{\gamma',\lambda'}\langle\phi_i|\chi_{\gamma,\lambda}\rangle\langle\chi_{\gamma',\lambda'}|\phi_j\rangle\langle\chi_{\gamma,\lambda}|H|\chi_{\gamma',\lambda'}\rangle \\ &= \langle\phi_i|T|\phi_j\rangle + \langle\phi_i|V_{pi}(\vec{r})|\phi_j\rangle + \langle\phi_i|V_{sc}(\vec{r}) + V_{ex}(\vec{r})|\phi_j\rangle \\ &\quad - \sum_{\gamma,\lambda}(E^0_{\gamma,\lambda} + \Delta E_\gamma)\langle\phi_i|\chi_{\gamma,\lambda}\rangle\langle\chi_{\gamma,\lambda}|\phi_j\rangle \ , \end{aligned} \tag{2.21}$$

and

$$\begin{aligned} S_{ij} &= \langle\phi_i|\phi_j\rangle - 2\sum_{\gamma,\lambda}\langle\phi_i|\chi_{\gamma,\lambda}\rangle\langle\chi_{\gamma,\lambda}|\phi_j\rangle \\ &\quad + \sum_{\gamma,\lambda}\sum_{\gamma',\lambda'}\langle\phi_i|\chi_{\gamma,\lambda}\rangle\langle\chi_{\gamma',\lambda'}|\phi_j\rangle\langle\chi_{\gamma,\lambda}|\chi_{\gamma',\lambda'}\rangle \\ &= \langle\phi_i|\phi_j\rangle - \sum_{\gamma,\lambda}\langle\phi_i|\chi_{\gamma,\lambda}\rangle\langle\chi_{\gamma,\lambda}|\phi_j\rangle \ . \end{aligned} \tag{2.22}$$

Here we have used equation 2.15 and

$$\langle\chi_{\gamma',\lambda'}|\chi_{\gamma,\lambda}\rangle = \delta_{\gamma\gamma'}\delta_{\lambda\lambda'} \ , \tag{2.23}$$

as well as

$$\begin{aligned} H|\chi_{\gamma,\lambda}\rangle &= E_{\gamma,\lambda}|\chi_{\gamma,\lambda}\rangle \\ &= (E^0_{\gamma,\lambda} + \Delta E_\gamma)|\chi_{\gamma,\lambda}\rangle \ . \end{aligned} \tag{2.24}$$

Equation 2.23 and equation 2.24 are based on the approximation that there is no overlap between cores on different ions. Here $E_{\gamma,\lambda}$ is the energy of the λth core orbital on the γth atom. It is the free atomic core energy $E^0_{\gamma,\lambda}$ (e.g. taken from the Clementi-Roetti table [30]), shifted by the potential produced by the rest of the lattice ΔE_γ, which is calculated as described in Section 2.1.

The first two terms of equation 2.21 are the kinetic energy and point-ion potential, respectively. The first term of equation 2.22 is the Gaussian overlap. The calculation of these terms is straightforward. The derivation of these expressions is given in Appendix A.

The last two terms of equation 2.21 and the last term of equation 2.22 represent the detailed contribution of all electrons belonging to each ion. The core orbitals in the lattice should be different from those in vacuum. An anion surrounded by cations in the lattice, is sitting at a potential well which makes the wavefunction slightly more compact. A cation, on the other hand, is at a potential barrier which makes the wavefunction slightly more diffuse. This effect is more pronounced for anions than cations. Thus for cations, we used the atomic orbitals of Clementi and Roetti [30]. For anions, the orbitals were recalculated with the SCF (self-consistent field) program in the presence of a square potential well.

2.3.1 Treatment of deep core electrons (ion size parameters)

Because of the large number of integrals of various kinds in the Fock operator (equation 2.21), several pseudopotential approaches have been proposed (Kübler and Friauf 1965, Bartram *et al.* 1968) [31, 28]. The one formulated by Bartram *et al.* has proved particularly convenient in various applications. Bartram's pseudopotential is based on the assumption that the smooth pseudo -wavefunction varies slowly over the region occupied by an atomic core, which we have imposed on our Gaussian ϕ_i (see above). Since ϕ_i is slowly varying, when expanded as a multipolar series about the site $\vec{R}_i$, the ϕ_i and it's first derivative can be taken to be constants. The integrations over the core orbitals are then performed to come up with the so-called ion-size parameters. Note that these parameters are properties of each individual ion and have no dependence on the pseudo- wavefunction used, provided that it is slowly-varying.

In the multipolar series expansion of ϕ about the site $\vec{R}_i$, the angular part of the integral can be readily evaluated, and the radial part can be further expanded in a Taylor's series about the same site. After some manipulation, the two lowest order ion-size terms can be expressed as (The derivation is given in Appendix B)

$$\sum_{\gamma,\lambda} \langle \phi_i | \chi_{\gamma,\lambda} \rangle \langle \chi_{\gamma,\lambda} | \phi_j \rangle = \sum_{\gamma} (f_1 B_\gamma + f_2 K'_\gamma + f_3 K_\gamma) \ , \tag{2.25}$$

and

$$\begin{aligned} & \langle \phi_i | V_{sc}(\vec{r}) + V_{ex}(\vec{r}) | \phi_j \rangle - \sum_{\gamma,\lambda} (E^0_{\gamma,\lambda} + \Delta E_\gamma) \langle \phi_i | \chi_{\gamma,\lambda} \rangle \langle \chi_{\gamma,\lambda} | \phi_j \rangle \\ = \ & \sum_{\gamma} (f_1 A_\gamma + f_2 J'_\gamma + f_3 J_\gamma) + \sum_{\gamma} \Delta E_\gamma (f_1 B_\gamma + f_2 K'_\gamma + f_3 K_\gamma) \ . \end{aligned} \tag{2.26}$$

The A, J', J, B, K', K are the so-called ion-size parameters which have different values for different types of ions. A and B are the lowest order terms formulated by Bartram *et al.* [28], and J and K are the next order terms introduced by Zwicker. J' and K', which are neglected in Zwicker's work [29], are parameters of the same order as the J and K. A, J', J represent the short range potential ($V_{sc} + V_{ex}$), while B, K', K represent the overlaps of the Gaussians with the core orbitals. B and K' concern s orbital only, and K concerns p orbital only, while A, J' and J are involved in all shells. The f_1, f_2 and f_3 are expansion terms of the Gaussian ϕ, they are functions depending only on the Gaussians and the vector joining them to the ion site.

In Table 2.5 we list the deep core and outer shells for the lattice ions F^- and Cd^{2+}, as well as the impurities In^{3+}, Ga^{3+}, Y^{3+} and Sc^{3+}. In Table 2.6 we present the values of the six ion-size parameters for them.

It has been found that when all of the orbitals of an ion are included in the calculation of ion-size parameters, the convergence is questionable, the second order terms K', K, J', J may be as large or even larger than the first order terms A and B. The reason is that the outermost shell orbitals are not compact enough compared to the pseudowavefunction, so that the slow varying approximation of ϕ breaks down.

Table 2.5: Deep Core and Outer Shells

Ion	Deep core	Outer shells
F^-	$1s^2$	$2s^2$, $2p^6$
Cd^{2+}	$1s^2 2s^2 3s^2 2p^6 3p^6 3d^{10}$	$4s^2$, $4p^6$, $4d^{10}$
In^{3+}	$1s^2 2s^2 3s^2 2p^6 3p^6 3d^{10}$	$4s^2$, $4p^6$, $4d^{10}$
Y^{3+}	$1s^2 2s^2 3s^2 2p^6 3p^6 3d^{10}$	$4s^2$, $4p^6$
Ga^{3+}	$1s^2 2s^2 2p^6$	$3s^2$, $3p^6$, $3d^{10}$
Sc^{3+}	$1s^2 2s^2 2p^6$	$3s^2$, $3p^6$

Table 2.6: Deep Core Ion Size Parameters

Ion	A	B	J	K	J'	K'
Cd^{2+}	38.07419	1.32768	3.02034	0.14148	3.32894	0.13107
F^-	7.88664	0.34693	-0.00792	0.00000	0.41828	0.01770
In^{3+}	40.11965	1.28102	2.74012	0.11753	4.73902	0.16480
Ga^{3+}	18.35158	0.37024	0.51672	0.01283	0.82085	0.01769
Y^{3+}	42.38996	3.09720	6.26569	0.61250	7.07830	0.55576
Sc^{3+}	26.56965	1.42588	1.96019	0.13306	3.14335	0.17373

All values are in atomic units.

A hybrid pseudopotential scheme was developed to improve the convergence. In this method, the ion-size parameters are calculated for the deep core orbitals (the summation over λ in equations 2.25 and 2.26 is restricted to deep core shells only), while the outermost shells are treated by interpolation.

2.3.2 Treatment of outer shell electrons (interpolation scheme)

There are three kinds of terms for the outermost shell (os) electrons of ions:

$\langle\phi_i|\chi_{\gamma,\lambda}\rangle$, $\langle\phi_i|V_{sc,\gamma}|\phi_j\rangle$, and $\langle\phi_i|V_{ex,\gamma}|\phi_j\rangle$,

they are overlap integral, screened Coulomb and exchange potentials, respectively. The interpolation is carried out in the following way:

1. Calculate the values of these terms exactly for a range of α's and R's, α is the Gaussian basis of the defect electron, and R is the distance between the defect electron and an ion.

2. Fit these values into suitable interpolation formulae.

Previously only s and p shells needed to be included in the outer shells. In this work $4d$ shell is the highest occupied energy level (with the most diffuse wavefunction) for Cd^{2+} and In^{3+}, and $3d$ for Ga^{3+} (see Table 2.5). We need to calculate the three terms of the d shell exactly for Cd^{2+}, In^{3+} and Ga^{3+}.

The screened Coulomb potential

The exact expression of the screened Coulomb term is

$$\langle\phi_i|V_{sc,\gamma}|\phi_j\rangle = -(Z_\gamma - \tilde{Z}_\gamma)\langle\phi_i(\vec{r})|\frac{1}{|\vec{r}-\vec{R}_\gamma|}|\phi_j(\vec{r})\rangle$$

$$+ \quad 2\sum_{\lambda}^{os}\langle\phi_i(\vec{r})|\frac{|\chi_{\gamma,\lambda}(\vec{r}_1)|^2}{|\vec{r}-\vec{r}_1|}|\phi_j(\vec{r})\rangle \ , \tag{2.27}$$

and this was fitted to an interpolation formula

$$\langle\phi_i|V_{sc,\gamma}|\phi_j\rangle = \int \phi_i^*(\vec{r})\frac{A_{sc,\gamma}e^{-\beta_{sc,\gamma}|\vec{r}-\vec{R}_\gamma|^2}}{|\vec{r}-\vec{R}_\gamma|}\phi_j(\vec{r})d\tau \ . \tag{2.28}$$

To determine the interpolation parameters $A_{sc,\gamma}$ and $\beta_{sc,\gamma}$ of an ion, the exact value of the potential needs to be calculated. First, the outermost s, p and d orbitals (in their Slater form as given by the SCF calculation) were fitted to a linear combination of a large number of Gaussians (about 15) respectively, then the exact value of the screened Coulomb interaction was computed using the analytic expressions.

With the Slater orbitals replaced by Gaussians, we have

$$\sum_{s}^{os}|\chi_{\gamma,\lambda}|^2 = \frac{1}{4\pi}\sum_{m,n}C_m^sC_n^se^{-\alpha_m^sr_m^2}e^{-\alpha_n^sr_n^2} \ ,$$

$$\sum_{p}^{os}|\chi_{\gamma,\lambda}|^2 = \frac{3}{4\pi}\sum_{m,n}C_m^pC_n^pe^{-\alpha_m^pr_m^2}e^{-\alpha_n^pr_n^2}(x_mx_n+y_my_n+z_mz_n) \ ,$$

$$\begin{aligned}\sum_{d}^{os}|\chi_{\gamma,\lambda}|^2 = {} & \frac{5}{4\pi}\sum_{m,n}C_m^dC_n^de^{-\alpha_m^dr_m^2}e^{-\alpha_n^dr_n^2}[12x_my_mx_ny_n \\ & + 12y_mz_my_nz_n + 12z_mx_mz_nx_n \\ & + 3(x_m^2-y_n^2)(x_n^2-y_n^2) \\ & + (3z_m^2-r_m^2)(3z_n^2-r_n^2)] \ . \end{aligned} \tag{2.29}$$

as in equation 2.17 the sum is over the states with the same spin. x, y and z come from the angular part of the wavefunction, which are

$$x = r\sin\theta\cos\phi, \quad y = r\sin\theta\sin\phi, \quad z = r\cos\theta.$$

Now we need to introduce the notation

$$\langle\alpha_ir_i';\alpha_mr_m\mu\nu\omega|\frac{1}{|\vec{r}-\vec{r'}|}|\alpha_nr_n\xi\eta\zeta;\alpha_jr_j'\rangle$$

$$= \int \frac{e^{-\alpha_i (r_i')^2} x_m^{\mu} y_m^{\nu} z_m^{\omega} e^{-\alpha_m r_m^2} x_n^{\xi} y_n^{\eta} z_n^{\zeta} e^{-\alpha_n r_n^2} e^{-\alpha_j (r_j')^2}}{|\vec{r} - \vec{r}'|} . \tag{2.30}$$

where

$$\begin{gathered} x_m^{\mu} y_m^{\nu} z_m^{\omega} e^{-\alpha_m r_m^2} \equiv G(\alpha_m, r_m, \mu, \nu, \omega) \\ (\vec{r}_m = \vec{r} - \vec{R}_m \ , \quad x_m = x - X_m) \end{gathered}$$

is a generalized Gaussian.

Substituting equation 2.29 into equation 2.27 and using the notation of the generalized Gaussian, we have

$$\begin{aligned}
\langle \phi_i | V_{sc,\gamma} | \phi_j \rangle &= -(Z_\gamma - \tilde{Z}_\gamma) N_i N_j \langle \alpha_i r_i | \frac{1}{|\vec{r} - \vec{R}_\gamma|} | \alpha_j r_j \rangle \\
&+ 2N_i N_j \left[\frac{1}{4\pi} \sum_{m,n} C_m^s C_n^s \langle \alpha_i r_i', \alpha_m^s r_m 000 | \frac{1}{|\vec{r} - \vec{r}'|} | \alpha_n^s r_n 000, \alpha_j r_j' \rangle \right. \\
&+ \frac{3}{4\pi} \sum_{m,n} C_m^p C_n^p \Big(\langle \alpha_i r_i', \alpha_m^p r_m 100 | \frac{1}{|\vec{r} - \vec{r}'|} | \alpha_n^p r_n 100, \alpha_j r_j' \rangle \\
&\quad + \langle \alpha_i r_i', \alpha_m^p r_m 010 | \frac{1}{|\vec{r} - \vec{r}'|} | \alpha_n^p r_n 010, \alpha_j r_j' \rangle \\
&\quad + \langle \alpha_i r_i', \alpha_m^p r_m 001 | \frac{1}{|\vec{r} - \vec{r}'|} | \alpha_n^p r_n 001, \alpha_j r_j' \rangle \Big) \\
&+ \frac{5}{4\pi} \sum_{m,n} C_m^d C_n^d \Big(12 \langle \alpha_i r_i', \alpha_m^d r_m 110 | \frac{1}{|\vec{r} - \vec{r}'|} | \alpha_n^d r_n 110, \alpha_j r_j' \rangle \\
&\quad + 12 \langle \alpha_i r_i', \alpha_m^d r_m 101 | \frac{1}{|\vec{r} - \vec{r}'|} | \alpha_n^d r_n 101, \alpha_j r_j' \rangle \\
&\quad + 12 \langle \alpha_i r_i', \alpha_m^d r_m 011 | \frac{1}{|\vec{r} - \vec{r}'|} | \alpha_n^d r_n 011, \alpha_j r_j' \rangle \\
&\quad + 4 \langle \alpha_i r_i', \alpha_m^d r_m 200 | \frac{1}{|\vec{r} - \vec{r}'|} | \alpha_n^d r_n 200, \alpha_j r_j' \rangle \\
&\quad + 4 \langle \alpha_i r_i', \alpha_m^d r_m 020 | \frac{1}{|\vec{r} - \vec{r}'|} | \alpha_n^d r_n 020, \alpha_j r_j' \rangle
\end{aligned}$$

$$
\begin{aligned}
&+ 4\langle \alpha_i r_i', \alpha_m^d r_m 002 | \frac{1}{|\vec{r}-\vec{r}'|} | \alpha_n^d r_n 002, \alpha_j r_j' \rangle \\
&- 2\langle \alpha_i r_i', \alpha_m^d r_m 200 | \frac{1}{|\vec{r}-\vec{r}'|} | \alpha_n^d r_n 020, \alpha_j r_j' \rangle \\
&- 2\langle \alpha_i r_i', \alpha_m^d r_m 020 | \frac{1}{|\vec{r}-\vec{r}'|} | \alpha_n^d r_n 200, \alpha_j r_j' \rangle \\
&- 2\langle \alpha_i r_i', \alpha_m^d r_m 200 | \frac{1}{|\vec{r}-\vec{r}'|} | \alpha_n^d r_n 002, \alpha_j r_j' \rangle \\
&- 2\langle \alpha_i r_i', \alpha_m^d r_m 002 | \frac{1}{|\vec{r}-\vec{r}'|} | \alpha_n^d r_n 200, \alpha_j r_j' \rangle \\
&- 2\langle \alpha_i r_i', \alpha_m^d r_m 020 | \frac{1}{|\vec{r}-\vec{r}'|} | \alpha_n^d r_n 002, \alpha_j r_j' \rangle \\
&- 2 \left.\left. \langle \alpha_i r_i', \alpha_m^d r_m 002 | \frac{1}{|\vec{r}-\vec{r}'|} | \alpha_n^d r_n 020, \alpha_j r_j' \rangle \right) \right] . \qquad (2.31)
\end{aligned}
$$

The recurrence formula of the generalized Gaussian is

$$
\begin{aligned}
& G(\alpha_m, r_m, \mu+1, \nu, \omega) \\
= & \frac{1}{2\alpha_m}\left[\frac{\partial}{\partial x_m} G(\alpha_m, r_m, \mu, \nu, \omega) + \mu G(\alpha_m, r_m, \mu-1, \nu, \omega)\right] ,
\end{aligned}
$$

and the integral is

$$
\begin{aligned}
& \langle \alpha_i r_i', \alpha_m r_m 000 | \frac{1}{|\vec{r}-\vec{r}'|} | \alpha_n r_n 000, \alpha_j r_j' \rangle \\
= & \; c \; exp\left[-u(\overline{R_i R_j})^2 - v(\overline{R_m R_n})^2\right] F_0\left[w\overline{PQ}^2\right] ,
\end{aligned}
$$

$$c = \frac{2\pi^{\frac{5}{2}}}{(\alpha_i+\alpha_j)(\alpha_m+\alpha_n)\sqrt{\alpha_i+\alpha_j+\alpha_m+\alpha_n}} ,$$

$$u = \frac{\alpha_i \alpha_j}{\alpha_i+\alpha_j} , \quad v = \frac{\alpha_m \alpha_n}{\alpha_m+\alpha_n} ,$$

$$w = \frac{(\alpha_i+\alpha_j)(\alpha_m+\alpha_n)}{\alpha_i+\alpha_j+\alpha_m+\alpha_n} ,$$

$$
\begin{aligned}
\overline{PQ}^2 &= (P_x - Q_x)^2 + (P_y - Q_y)^2 + (P_z - Q_z)^2 , \\
P_x &= \frac{\alpha_i R_{ix} + \alpha_j R_{jx}}{\alpha_i + \alpha_j}, \quad Q_x = \frac{\alpha_m R_{mx} + \alpha_n R_{nx}}{\alpha_m + \alpha_n}, \\
P_y &= \frac{\alpha_i R_{iy} + \alpha_j R_{jy}}{\alpha_i + \alpha_j}, \quad Q_y = \frac{\alpha_m R_{my} + \alpha_n R_{ny}}{\alpha_m + \alpha_n}, \\
P_z &= \frac{\alpha_i R_{iz} + \alpha_j R_{jz}}{\alpha_i + \alpha_j}, \quad Q_z = \frac{\alpha_m R_{mz} + \alpha_n R_{nz}}{\alpha_m + \alpha_n}.
\end{aligned} \tag{2.32}
$$

Applying the recurrence formula and the integral to equation 2.31, an analytical expression was obtained (the calculation for d shell is tedious). To determine the interpolation parameters A_{sc} and β_{sc} of equation 2.28, we simplified the work by setting $\vec{R}_i = \vec{R}_j = \vec{R}$ and $\vec{R}_m = \vec{R}_n = 0$, without loosing the generality. The final analytical expression of the screened Coulomb energy is

$$
\begin{aligned}
\langle \phi_i | V_{sc,\gamma} | \phi_j \rangle &= -(Z_\gamma - \tilde{Z}_\gamma) N_i N_j \frac{2\pi}{\alpha_i + \alpha_j} e^{-\frac{\alpha_i \alpha_j}{\alpha_i + \alpha_j} R^2} F_0 \left[(\alpha_i + \alpha_j) R^2 \right] \\
&+ 2 N_i N_j \sum_{m,n} \left(I^s_{m,n} + I^p_{m,n} + I^d_{m,n} \right) , \\
I^s_{m,n} &= C^s_m C^s_n c^s e^{-\mu R^2} \frac{1}{4\pi} F_0 \left[\omega^s R^2 \right] , \\
I^p_{m,n} &= C^p_m C^p_n c^p e^{-\mu R^2} \frac{3}{4\pi} \cdot \frac{1}{4 \alpha^p_m \alpha^p_n} \left\{ 6\mu F_0 \left[\omega^p R^2 \right] \right. \\
&- \left. \frac{6\mu\omega^p}{\alpha^p_m + \alpha^p_m} F_1 \left[\omega^p R^2 \right] + \frac{4\mu(\omega^p)^2}{\alpha^p_m + \alpha^p_n} R^2 \, F_2 \left[\omega^p R^2 \right] \right\} ,
\end{aligned}
$$

$$\begin{aligned} I^d_{m,n} &= C^d_m C^d_n c^d e^{-\mu R^2} \frac{5}{4\pi} \cdot \frac{1}{64(\alpha^d_m)^2(\alpha^d_n)^2} \\ & \left\{ 240\mu^2 F_0\left[\omega^d R^2\right] - \frac{480\mu^2\omega^d}{\alpha^d_m + \alpha^d_n} F_1\left[\omega^d R^2\right] \right. \\ &+ \left(\frac{240}{\alpha^d_m + \alpha^d_n} + 320R^2 \right) \frac{\mu^2(\omega^d)^2}{\alpha^d_m + \alpha^d_n} F_2\left[\omega^d R^2\right] \\ &- 320 \frac{\mu^2(\omega^d)^3}{(\alpha^d_m + \alpha^d_n)^2} R^2 F_3\left[\omega^d R^2\right] \\ &+ \left. \frac{64\mu^2(\omega^d)^4}{(\alpha^d_m + \alpha^d_n)^2} R^2 F_4\left[\omega^d R^2\right] \right\} . \end{aligned} \qquad (2.33)$$

Here N_i is the normalization factor for α_i; $c(c^s, c^p, c^d)$, u, v and $w(w^s, w^p, w^d)$ are defined as in equation 2.32.

The exact value of the screened Coulomb interaction involved in the outermost s, p and d shells was calculated for a range of the Gaussians' α_i and R_i of ϕ_i, so that the interpolation formula will be applicable to all ions of the same type as ion γ. The least squares method was used for the fitting to determine the constants $A_{sc,\gamma}$ and $\beta_{sc,\gamma}$. The particular matrix elements of $\int \phi_i(Ae^{-\beta r^2}/r)\phi_j d\tau$ chosen for the fit are diagonal elements. Because of the well known fact that the product of two Gaussian functions is a gaussian centered on another site, the fit of diagonal elements in fact covers all off-diagonal elements. This is one example of the usefulness of Gaussians. Quite satisfactory fits were obtained by using this procedure, with RMS deviations better than 10^{-3} in all cases. The values of the fitted parameters A_{sc} and β_{sc} are listed in Table 2.8.

Table 2.7: Values of the Screened Coulomb Energy

R	$\alpha = 0.02$	$\alpha = 0.04$	$\alpha = 0.06$	$\alpha = 0.08$	$\alpha = 0.10$
0	-0.5239E-01 -0.5212E-01	-0.1428E+00 -0.1421E+00	-0.2532E+00 -0.2521E+00	-0.3771E+00 -0.3755E+00	-0.5107E+00 -0.5085E+00
3	-0.3689E-01 -0.3709E-01	-0.7197E-01 -0.7235E-01	-0.9271E-01 -0.9319E-01	-0.1016E+00 -0.1021E+00	-0.1025E+00 -0.1030E+00
6	-0.1288E-01 -0.1292E-01	-0.9258E-01 -0.9274E-01	-0.4641E-02 -0.4644E-02	-0.2104E-02 -0.2104E-02	-0.9419E-03 -0.9421E-03
9	-0.2233E-02 -0.2252E-02	-0.3075E-03 -0.3100E-03	-0.3301E-04 -0.3431E-04	-0.2967E-05 -0.4258E-05	0.6085E-06 -0.6996E-06

These values are contributed by the $4d$ shell of Cd^{2+}. α is the Gaussian exponent of the pseudo-wavefunction, and R is the distance between a Cd^{2+} ion and the site of the pseudo-wavefunction, both α and R are in atomic units. The first and second lines are the values obtained with analytical and numerical method, respectively.

The contribution of os orbitals to the screened Coulomb energy was also evaluated numerically by using Gauss-Laguerre, Gauss-Legendre quadratures and Hartree-Fock wavefunctions given by Clementi and Roetti [30]. In both analytical and numerical cases the pseudowavefunction is in a Gaussian basis, the results of both methods are in good agreement. Table 2.7 gives a comparison of values of the screened Coulomb energy calculated with these two methods.

The exchange potential

The exchange interaction was interpolated in much the same way. The exact form of the exchange energy is

$$\langle \phi_i | V_{ex,\gamma} | \phi_j \rangle = \sum_{\lambda}^{os} \int \frac{\phi_i(r_2) | \chi_{\gamma,\lambda}(r_1) \chi_{\gamma,\lambda}(r_2) | \phi_j(r_1)}{|\vec{r}_1 - \vec{r}_2|} d\tau_1 d\tau_2 \ , \tag{2.34}$$

and it is fitted to the form

$$\langle \phi_i | V_{ex,\gamma} | \phi_j \rangle = \int \phi_i^* A_{ex,\gamma} e^{-\beta_{ex,\gamma} |\vec{r} - \vec{R}_\gamma|^2} d\tau \ . \tag{2.35}$$

The analytical expression of the exchange energy of the outermost d shell is very complicated. The exchange energy of the outermost s and p shells were calculated analytically from Gaussian representation, while that of the outermost d shell was calculated with the Slater approximation

$$E_{ex} = 3 \left(\frac{3}{8\pi} \right)^{\frac{1}{3}} [\rho(\vec{r})]^{\frac{1}{3}} \ , \quad (in\ Hartree) \tag{2.36}$$

Where $\rho(\vec{r})$ is the charge density which was determined from the wavefunctions given by Clementi and Roetti [30].

We compared the values of the exchange potential of os s and p calculated with the Slater approximation with the exact one calculated analytically. It was found that for small distance ($R \leq 6a.u.$) and not very compact Gaussian damping ($\alpha < 0.10a.u.$), they are in good agreement. As R gets larger the values of exact calculation decreases much faster than that of Slater approximation. In our work the floating Gaussian bases were put at or very close to the impurities, so that the range of small R is important. The distance between the floating Gaussian bases

Table 2.8: Short Range Potential Interpolation Parameters (a.u.)

Ion	β_{sc}	A_{sc}	β_{ex}	A_{ex}
Cd^{2+}	1.27120	-11.21865	0.27200	-1.49370
F^-	0.66400	-3.37977	0.37120	-2.04467
In^{3+}	1.54320	-11.79197	0.36160	-1.83031
Ga^{3+}	2.33520	-9.06605	0.42080	-1.58782
Y^{3+}	1.00000	-5.94245	0.34400	-1.91351
Sc^{3+}	1.44240	-5.56568	0.53760	-2.54686

All values are in atomic units. The values of Cd^{2+} and F^- are for fluorite structure.

and the first Cd^{2+} shell is about 6 *a.u*, at the distance of the second Cd^{2+} shell the exchange potential has become very small.

The RMS deviation in all cases was better than 10^{-2}. The values of fitted parameters A_{ex} and β_{ex} are listed in Table 2.8.

The overlap integrals

The overlap integrals are terms of the form:

$$\begin{aligned} ss\sigma &= \int \phi_i^*(\vec{r})\chi_s(\vec{r})d\tau \ , \\ sp\sigma &= \int \phi_i^*(\vec{r})\chi_p(\vec{r})d\tau \ , \\ sd\sigma &= \int \phi_i^*(\vec{r})\chi_d(\vec{r})d\tau \ . \end{aligned} \tag{2.37}$$

The fits of the overlap integrals of a single Gaussian and the outer *s*, *p* and *d* orbitals were made separately. The *s*, *p* and *d* functions are plotted in Fig. 2.5. Only the *spσ* and *sdσ* integrals need to be calculated. The *spπ*, *sdπ* and *sdδ* integrals are 0 by symmetry. σ, π and δ refer to $m_l = 0$, $m_l = \pm 1$ and $m_l = \pm 2$, relative to the

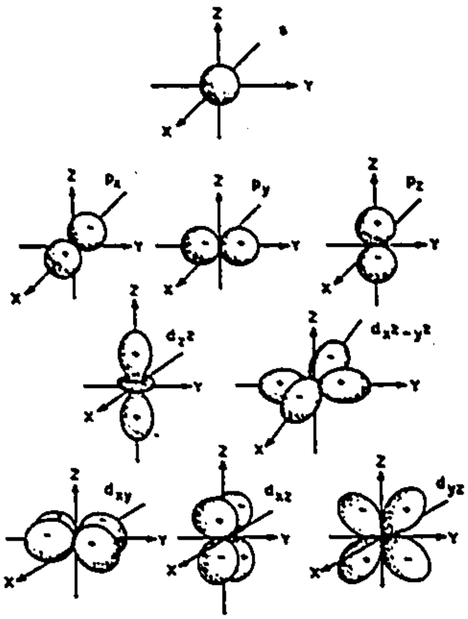

Figure 2.5: The Atomic Orbitals ($l = 0, 1, 2$)

axis joining the two orbitals.

The geometrical results of the overlap integrals have been worked out by Slater and Koster [32]. To introduce their work we set the coordinates for two-center integrals as in Fig. 2.6. We put the defect electron in the crystal as the origin O of a spherical coordinate system and consider the vector $\vec{r}$ determined by any ion in the crystal located at the point P (Fig). The direction cosines l, m and n of r with respect to the rectangular coordinates are given by

$$l = x/r = \sin\theta\cos\phi, \quad m = y/r = \sin\theta\sin\phi, \quad n = z/r = \cos\theta.$$

We then set up a second coordinate system OX'Y'Z' with the same origin as OXYZ and with the OZ' axis lying along OP. The transformation matrix will be designated by

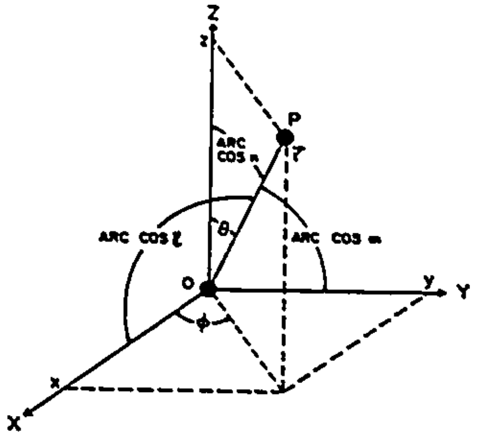

Figure 2.6: Coordinates Used for Two-Center Integrals

$$\begin{Bmatrix} OX' \\ OY' \\ OZ' \end{Bmatrix} = \begin{bmatrix} a_{11} & a_{12} & a_{13} \\ a_{21} & a_{22} & a_{23} \\ a_{31} & a_{32} & a_{33} \end{bmatrix} \begin{Bmatrix} OX \\ OY \\ OZ \end{Bmatrix}$$

so that

$$a_{13} = l, \quad a_{23} = m, \quad a_{33} = n. \tag{2.38}$$

Now let us look at an example of the two-center overlap integral:

$$(s, x'y') \equiv \langle \phi_i | d_{x'y'} \rangle . \tag{2.39}$$

With the transform functions we take equations

$$\begin{aligned} x' &= a_{11}x + a_{12}y + a_{13}z \ , \\ y' &= a_{21}x + a_{22}y + a_{23}z \ , \end{aligned}$$

and rewrite them as

$$\begin{aligned} x' &= \frac{1}{2}[(a_{11}+ia_{12})(x-iy)] + \frac{1}{2}[(a_{11}-ia_{12})(x+iy)] + a_{13}z\ , && (2.40)\\ y' &= \frac{1}{2}[(a_{21}+ia_{22})(x-iy)] + \frac{1}{2}[(a_{21}-ia_{22})(x+iy)] + a_{23}z\ , && (2.41)\end{aligned}$$

we then have

$$\begin{aligned} x'y' &= \frac{1}{2}[(a_{11}a_{21}+a_{12}a_{22})(x^2+y^2)] + a_{13}a_{23}z^2 \\ &+ \frac{1}{2}[(a_{11}+ia_{12})(x-iy)a_{23}z] + \frac{1}{2}[(a_{11}-ia_{12})(x+iy)a_{23}z] \\ &+ \frac{1}{2}[(a_{21}+ia_{22})(x-iy)a_{13}z] + \frac{1}{2}[(a_{21}-ia_{22})(x+iy)a_{13}z]\ . && (2.42)\end{aligned}$$

The first two terms of 2.42 can be combined to give

$$\begin{aligned} -(lm/2)(x^2+y^2) + lmz^2 &= lm[z^2 - \frac{1}{2}(x^2+y^2)] \\ &= (lm/2)[3z^2 - r^2]\ , && (2.43)\end{aligned}$$

since

$$a_{11}a_{21} + a_{12}a_{22} + a_{13}a_{23} = 0\ ,$$
$$x^2 + y^2 + z^2 = r^2\ .$$

The rest terms of 2.42 will become zero after integration, since

$$\begin{aligned} x &+ iy \propto sin\theta e^{i\phi}\ , \\ x &- iy \propto sin\theta e^{-i\phi}\ ,\end{aligned}$$

and

$$\int_0^{2\pi} exp(im_l\phi)d\phi = 0\ , \qquad (2.44)$$

Table 2.9: Two-Center Integrals in Terms of Atomic Orbital Integrals

(s,s)	$(ss\sigma)$
(s,x)	$l(sp\sigma)$
(s,y)	$m(sp\sigma)$
(s,z)	$n(sp\sigma)$
(s,xy)	$\sqrt{3}lm(sd\sigma)$
(s,yz)	$\sqrt{3}mn(sd\sigma)$
(s,zx)	$\sqrt{3}nl(sd\sigma)$
(s,x^2-y^2)	$\frac{\sqrt{3}}{2}(l^2-m^2)(sd\sigma)$
$(s,3z^2-r^2)$	$\left[n^2-\frac{1}{2}(l^2+m^2)\right](sd\sigma)$

when $m_l = \pm 1, \pm 2, \cdots$. The integral 2.39 is then

$$\begin{aligned} \langle \phi_i | d_{x'y'} \rangle &= \sqrt{\frac{15}{4\pi}} \langle \phi_i | x'y' \rangle \\ &= \sqrt{\frac{15}{4\pi}} \cdot \frac{lm}{2} \langle \phi_i | (3z^2 - r^2) \rangle \\ &= \sqrt{3} lm \langle \phi_i | d_{3z^2-r^2} \rangle \\ &= \sqrt{3} lm (sd\sigma) \ . \end{aligned} \tag{2.45}$$

Any general *sp* overlap may be decomposed into it's σ and π components, and any general *sd* overlap into it's σ, π and δ components, but only the σ component will be non-zero. Table 2.9 lists the two-center overlap integrals of the defect electron and the outer s, p and d shells of the ions, noted as (s,s), (s,p) and (s,d) as in the Slater and Koster's paper [32].

Finally, equations 2.37 becomes

$$\begin{aligned}
ss\sigma &= \left(\frac{2\beta}{\pi}\right)^{\frac{3}{4}} \sum_m C^s_m \left(\frac{\pi}{\alpha^s_m + \beta}\right)^{\frac{3}{2}} exp\left(-\frac{\alpha^s_m \beta}{\alpha^s_m + \beta} R^2\right) \sqrt{\frac{1}{4\pi}} , \\
sp\sigma &= \left(\frac{2\beta}{\pi}\right)^{\frac{3}{4}} \sum_m C^p_m \left(\frac{\pi}{\alpha^p_m + \beta}\right)^{\frac{3}{2}} exp\left(-\frac{\alpha^p_m \beta}{\alpha^p_m + \beta} R^2\right) \sqrt{\frac{3}{4\pi}} \frac{\beta R}{\alpha^p_m + \beta} , \\
sd\sigma &= \left(\frac{2\beta}{\pi}\right)^{\frac{3}{4}} \sum_m C^d_m \left(\frac{\pi}{\alpha^d_m + \beta}\right)^{\frac{3}{2}} exp\left(-\frac{\alpha^d_m p\beta}{\alpha^d_m + \beta} R^2\right) \sqrt{\frac{5}{4\pi}} \left(\frac{\beta R}{\alpha^d_m + \beta}\right)^2 .
\end{aligned} \tag{2.46}$$

It was found [25] that an interpolation formula using one Gaussian to represent the core states was inadequate compared to the accuracy of the screened Coulomb and exchange terms. However, two Gaussians with their exponents related by a simple ratio gave fits of sufficient accuracy. Therefore we used the form of equation (2.47) to represent the overlap with the outer s core states

$$ss\sigma \Rightarrow \langle\phi_i|\chi_s\rangle = N^s \int \phi_i^* \left(N_1^s e^{-\beta_{soul} r^2} + A_{soul} N_2^s e^{-\beta_{soul} r^2/\kappa_s}\right) d\tau . \tag{2.47}$$

Here κ_s is the ratio of the exponents of the two fitted Gaussians, which is determined together with A_{soul} and β_{soul} by the least squares fitting procedure. N_1^s, N_2^s and N^s are normalization factors determined by the other parameters of the equation.

Similarly, the overlaps with the outer p and d shells are fitted to functions of the form

$$\begin{aligned}
sp\sigma \;\Rightarrow\; \langle\phi_i|\chi_{pz}\rangle = N^p \int \phi_i^* \Big(& N_1^p e^{-\beta_{poul} r^2} \\
& + A_{poul} N_2^p e^{-\beta_{poul} r^2/\kappa_p} \Big) z d\tau ,
\end{aligned} \tag{2.48}$$

$$\begin{aligned}
sd\sigma \;\Rightarrow\; \langle\phi_i|\chi_{d(3z^2-r^2)}\rangle = N^d \int \phi_i^* \Big(& N_1^d e^{-\beta_{doul} r^2} \\
& + A_{doul} N_2^d e^{-\beta_{doul} r^2/\kappa_d}\Big) \left(3z^2 - r^2\right) d\tau .
\end{aligned} \tag{2.49}$$

Table 2.10: Overlap Interpolation Parameters

	Cd^{2+}	F^-	In^{3+}	Ga^{3+}	Y^{3+}	Sc^{3+}
β_{sovl}	1.35000	1.00000	1.30000	1.90000	1.35000	0.85000
A_{sovl}	0.20393	0.51244	0.11649	0.08680	0.93945	0.15647
κ_s	4.00000	4.00000	4.00000	4.00000	5.00000	4.00000
E_s(eV)	-5.10563	-1.06393	-6.01794	-7.60028	-3.10847	-3.71349
β_{povl}	2.40000	1.00000	1.40000	2.05000	0.65000	0.80000
A_{povl}	0.68044	0.34179	0.15522	0.02728	0.21845	0.04770
κ_p	4.00000	8.00000	3.00000	8.00000	3.00000	6.00000
E_p(eV)	-3.71585	-0.17059	-4.55699	-5.69828	-2.22808	-2.70383
β_{dovl}	0.80000		1.05000	1.75000		
A_{dovl}	0.07244		0.08879	0.07919		
κ_d	5.00000		5.00000	6.00000		
E_d(eV)	-1.42277		-2.10770	-2.40890		

All parameters are in atomic units. E_s, E_p and E_d are the energies of the outer *s*, *p* and *d* shells, respectively. F^-, Y^{3+} and Sc^{3+} have no outer *d* shells.

Here all the parameters are determined in the same way as for the *s* shell overlap. The RMS deviation in all cases are better than 10^{-3}. The values of the fitted overlap parameters are given in Table 2.10.

In order to test the quality of the present extended-ion approximation (the parameters obtained) we have evaluated the energies of the three lowest excited states: $(n+1)s$, $(n+1)p$ and $(n+2)s$ (n is the principal quantum number of the last closed shell) for Cd^{2+}, In^{3+} and Ga^{3+}; and nd, $(n+1)s$ and $(n+1)p$ for Y^{3+} and Sc^{3+}. We have used about 8 FGO bases. The p state is calculated using pairs of 1s Gaussian-type orbital GTO located on an axis, and the d state using four sets of 1s GTO located on two axes. The results are presented in Table 2.11. The experimental data are

Table 2.11: Free Ion Energies

		5*s*	5*p*	6*s*
$Cd^{2+}[Kr]4d^{10}$		-16.46	-11.21	-6.20
	(exp)	-16.90	-11.12	-6.61
		5*s*	5*p*	6*s*
$In^{3+}[Kr]4d^{10}$		-28.06	-20.25	-11.69
	(exp)	-28.03	-20.40	-12.30
		4*s*	4*p*	5*s*
$Ga^{3+}[Ar]3d^{10}$		-30.91	-22.74	-12.52
	(exp)	-30.70	-22.41	-13.25
		$4d^*$	5*s*	5*p*
$Y^{3+}[Kr]4p^6$		-20.2	-19.53	-14.92
	(exp)	-20.5	-19.57	-15.17
		$3d^*$	4*s*	4*p*
$Sc^{3+}[Ar]3p^6$		-17.20	-21.20	-16.57
	(exp)	-24.75	-21.58	-16.99

First three excited state energies of Cd^{2+} and the trivalent impurities. Energies are measured from the ionization limit, and in eV's. Experimental data (exp) are from Moore [33]. *Very compact bases to be needed to simulate 4*d*(Y) and 3*d*(Sc) levels.

from Moore [33]. The results show good agreement with the experimental data, except for $3d$(Sc). We have found that very compact bases are needed for $4d$(Y) and $3d$(Sc) calculations, which are beyond the range of the Gaussian exponent of the pseudo-wavefunction in the fitting of the various terms of the outer shells.

2.4 Polarization Energy

The impurity ion has a net charge of $+e$, so that lattice polarization effect is quite strong. There are two approaches of treating the polarization energy, the quasi-adiabatic approximation and the Hartree-Fock procedure [34].

The quasi-adiabatic approximation is: when an additional, weakly bound electron is introduced into a polar crystal, the tightly bound, rapidly revolving core electrons follow its slow motion in detail. The additional electron, however, cannot follow the detailed motion of the core electrons but is affected only by the average of their motions. It is often suggested that the justification of this approximation is analogous to that of the well-known Born-Oppenheimer adiabatic approximation.

The point of view adopted in the Hartree-Fock method is almost diametrically opposed to that represented by the quasi-adiabatic approximation. The Hartree-Fock procedure implies that, except for the correlation imposed by the exclusion principle, every electron moves in an averaged field of all the other electrons. This assumption is certainly reasonable for the trapped electrons, but it is somewhat questionable for the case of a core electron, since the core electron is presumably capable of following the detailed motion of the slow trapped electron.

It seems that the quasi-adiabatic approximation is more accurate, since the induced dipoles of the core electrons pointing towards instantaneous position of the defect electron, as shown in Fig. 2.7. This requires the computation of an effective

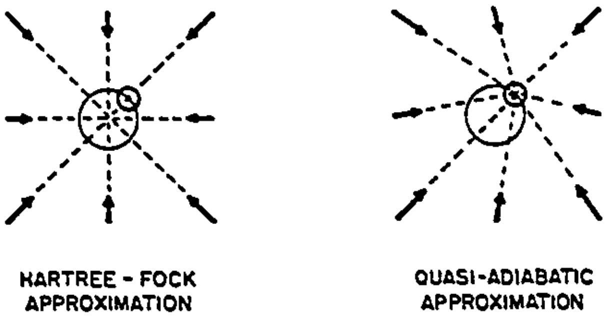

Figure 2.7: Approximations of Polarization Calculation

field in which the trapped electron moves, and the computation of this effective field at the point $\vec{r}$ requires the determination of the field of the polarized core electrons when the trapped electron is at the field point $\vec{r}$. The calculation is very difficult since it has to be done at every point in space. On the other hand, the Hartree-Fock procedure does not require the computation of the polarization at every point in space.

We have used the Hartree-Fock approximation in the calculation of the defect electron energy. There is an aspect in the electron energy calculation that makes the Hartree-Fock approximation superior to the quasi-adiabatic method. The repulsive force between the trapped electron and the core electrons are taken into account in the Hartree-Fock procedure in the exchange term. However, exchange has been omitted in the formulation of the quasi-adiabatic approximation, so it cannot be used for the calculation of the lattice distortion in the vicinity of the center.

We adopted the Hartree-Fock procedure [34] to calculate the polarization energy. We assume that the ions behave as point dipoles with polarisability equal to the free atomic polarisability. This is valid when the overlap between neighbouring atoms is small. Unfortunately, in the shallow state, ions of the first shell surrounding the impurity get about 15% closer than they were in the perfect lattice sites. Since there is no simple way of estimating the effect of this situation on the polarization energy, it is left unchanged. Also we assume that all dipole vectors and electric field vectors are constrained to be radial. It is reasonable because the electron charge cloud and the atomic displacements are of radial symmetry.

The polarization energy is expressed in terms of the Hartree-Fock picture:

$$\begin{aligned} E_{pol} &= -\sum_{\gamma} \vec{\mu}(\vec{R}_{\gamma}) \cdot \vec{E}(\vec{R}_{\gamma}) \,, & (2.50) \\ \vec{E}(\vec{R}_{\gamma}) &= \vec{E}_1(\vec{R}_{\gamma}) + \vec{E}_{dip}(\vec{R}_{\gamma}) \,, & (2.51) \\ \vec{\mu}(\vec{R}_{\gamma}) &= \alpha_{\gamma} \vec{E}(\vec{R}_{\gamma}) \,. & (2.52) \end{aligned}$$

Where $\vec{E}(\vec{R}_{\gamma})$ is the local electric field which consists of two parts: $\vec{E}_1(\vec{R}_{\gamma})$, produced by the defect electron and the lattice distortions; $\vec{E}_{dip}(\vec{R}_{\gamma})$, produced by the induced dipoles. $\vec{\mu}(\vec{R}_{\gamma})$ is the dipole moment induced on the ion at $\vec{R}_{\gamma}$. They are determined self-consistently by iteration. α_{γ} is the free atomic polarisability of ion γ.

The following are the details concerning the three contributions of local electric field:

(1) The electric field due to lattice distortions: Consider the electric field at a lattice site in a perfect lattice, with neither distortion nor defect. In this case there would be no electric field at the sampling point since the field produced by any one ion in the lattice is exactly canceled by other ions in the lattice (at least in a cubic crystal). Now if an ion of charge q is displaced from it's perfect lattice site, the sampling ion will "see" the real charge q at it's new position, as well as an image charge $-q$ at the original position due to the surrounding lattice. Both of

these "charges" will contribute to the local electric field at the sampling point. This method is suitable for the sampling point being the perfect lattice site, for example, to calculate the electric field at ions outside of the small cluster of nearest-neighbour ions that have been allowed to relax.

When ions are allowed to move, the sampling point is away from a perfect lattice site. At these points the simple method described above does not apply because of the lower symmetry of the new sampling position. In this case first we determine the lattice potential V generated by the lattice distortion, then we calculate the gradient of the potential numerically in the immediate neighbourhood of the ion in question,

$$\vec{E}_{LD} = - \nabla V \; . \tag{2.53}$$

The method of calculating V is the same as described in section II.1. In this work the ions which have been explicitly relaxed are about 50.

(2) The electric field created by the defect electron: We use the electron wavefunction obtained from the electron energy calculation. The charge density is

$$\begin{aligned} \rho(\vec{r}) &= |\psi(\vec{r})|^2 \\ &= \left| \sum_i c_i e^{-\alpha_i |\vec{r}-\vec{R}_i|^2} \right|^2 \\ &= \sum_k d_k e^{-\alpha_k |\vec{r}-\vec{R}_k|^2}, \end{aligned} \tag{2.54}$$

the last step is by the Gaussian product rule.

In this part of calculation, we neglect the core orthogonalization of the wavefunction, as this would make it too complicated, so electron wavefunction is renormalized. The charge enclosed in a sphere of radius $|\vec{r} - \vec{R}_k|$ due to the Gaussian k is

$$Q_k(\vec{R}_\gamma) = \int^{\vec{R}_\gamma} e^{-\alpha_k |\vec{r}' - \vec{R}_k|^2} d\tau' , \tag{2.55}$$

and the field is given by the Gauss Law

$$\vec{E}_{DF}(\vec{R}_\gamma) = -\sum_k d_k \frac{Q_k(\vec{R}_\gamma)}{|\vec{R}_\gamma - \vec{R}_k|^3}(\vec{R}_\gamma - \vec{R}_k). \tag{2.56}$$

The field produced by the defect electron is added to the field produced by the lattice distortion to give the $\vec{E}_1(\vec{R}_\gamma)$.

(3) The electric field due to the induced dipoles: The field produced at site $\vec{R}_\gamma$ by the induced dipole moments is

$$\vec{E}_{dip}(\vec{R}_\gamma) = \sum_{k \neq \gamma} \left\{ \frac{3(\vec{\mu}(\vec{R}_k) \cdot \vec{R}_{\gamma k})\vec{R}_{\gamma k}}{|\vec{R}_{\gamma k}|^5} - \frac{\vec{\mu}(\vec{R}_k)}{|\vec{R}_{\gamma k}|^3} \right\}, \tag{2.57}$$

where $\vec{R}_{\gamma k} = \vec{R}_\gamma - \vec{R}_k$.

$\vec{E}_{dip}(\vec{R}_\gamma)$ and $\vec{\mu}(\vec{R}_\gamma)$ are determined simultaneously, the iterative method is very simple. The initial value of $\vec{\mu}(\vec{R}_\gamma)$ is estimated from the field produced by the lattice distortion and the defect electron, that means setting $\vec{E}_{dip} = 0$ in equation (2.51):

$$\vec{\mu}(\vec{R}_\gamma) = \alpha_\gamma \vec{E}_1(\vec{R}_\gamma). \tag{2.58}$$

Inserting this set of $\vec{\mu}(\vec{R}_\gamma)$ into equation (2.57), new $\vec{E}_{dip}(\vec{R}_\gamma)$'s are determined, and then new $\vec{\mu}(\vec{R}_\gamma)$'s are obtained by equation (2.51). Convergence of at least four figures was usually obtained within 3 or 4 iterations.

It is well known that all the dielectric materials exhibit different types of polarizations which can be classified in three categories, (i) electronic, (ii) ionic or atomic, (iii) dipolar orientational [35]. Whether one or two or all three types of polarization mechanisms operate in a dielectric material depends on various factors including the structure of material and the frequency of applied electric field [36]. The electronic polarization is found to be present even at high frequencies in every dielectric material. Ionic crystals form an important class of dielectric materials which show two

Table 2.12: Free Atomic Polarisabilities

	[b]Cd^{2+}	[a]F^-	[a]In^{3+}	[a]Ga^{3+}	[a]Y^{3+}	[a]Sc^{3+}
(atomic units)	12.160	7.028	4.932	1.350	3.712	1.930

[a] Pauling [38]. [b] Tessman and Kahn [37].

types of polarizations, electronic and ionic. The third type of polarization, orientational, is absent in the present system because there are no permanent dipoles. The electronic polarization of ions arises from the deformation of electronic charge with respect to their own nuclei, while the ionic polarization results from the lattice distortion. In the present work the ionic polarization concerns about 50 ions, which are allowed to relax from their perfect lattice sites during the minimization of the energy. On the other hand the electronic polarization involves a much larger cluster of ions. Because the wavefunction of the defect electron is very diffuse in the shallow state, we have chosen a cluster of about 500 ions surrounding the impurity to calculate polarization energy. It was found to be large enough by testing a larger cluster. The neglect of the outer ions is justified because the defect system is electrically neutral.

The free atomic polarisabilities that we used in this work are given in Table 2.12. They are taken from references [37] and [38].

2.5 Minimization Method

So far we have described the method of calculating various energy terms. There remains the problem of finding the minimum energy configuration of the system.

The lattice configuration should be determined with respect to the minimization of the total energy:

$$E_{total} = E_{coul} + E_{rep} + E_{elec} + E_{pol} \; . \tag{2.59}$$

Where the various constituent energies have been described in the previous four sections.

Most discussions of the electron-phonon interaction use the Hellmann-Feynman [39] theorem, which relates the expectation value of a derivative of the Hamiltonian to the derivative of an expectation value

$$\langle \psi(\lambda) | \partial \mathcal{H} / \partial \lambda | \psi(\lambda) \rangle = \frac{\partial}{\partial \lambda} \langle \psi(\lambda) | \mathcal{H} | \psi(\lambda) \rangle \; , \tag{2.60}$$

where $\langle \psi(\lambda) | \psi(\lambda) \rangle = 1$, λ is one of the atomic coordinates. Usually it is more convenient to compute the expectation value of a derivative of the Hamiltonian, according to which the force balance method is used in obtaining the equilibrium. However, in the present work, we found it simpler to evaluate the energy gradient directly in determining the adiabatic potential energy.

In terms of the point symmetry of the system, ions around the impurity are allowed to move in shells in a radial direction. The first shell ions around the impurity are F^-'s, the second Cd^{2+}'s, the third F^-'s, and so on. To investigate the possibility of bistable potential energy of CdF_2:M^{3+}, it is necessary to define a suitable configuration coordinate (c.c.). Sometimes the choice of a c.c. is arbitrary to some degree. In the present system, we have chosen M^{3+}-F^- distance as the c.c. and varied its range from about -0.30Å (toward the impurity) to about 0.30Å (away from the impurity). For each fixed position of the first shell, the second and third shells are allowed to relax to give the minimum energy configuration of the system. The fourth shell was also allowed to relax, but the distortion was found very small.

It is good enough that the surrounding shells are relaxed up to the third (about 50 ions).

We used two diffuse and one compact Gaussian bases centered on the impurity to represent the defect electron. The optimized Gaussian damping factors ($\alpha = 0.005$ for the shallow and $\alpha = 0.08$ for the deep levels) are chosen such that the lowest energies are obtained in either the shallow (delocalized) or deep (localized) state.

2.6 The CPU Times

We used the mainframe IBM(CMS) to calculate the adiabatic potential energy surface (APES) of the bistable system. The CPU time needed mainly depends on the number of the gaussian bases and the number of ions which are allowed to relax. In the case of 3 gaussian bases and 45 relaxing ions (the number of ions for calculating the lattice Coulomb energy and the electron energy is 1800, and the number of ions for calculating the polarization energy is 500), about 1.5 hours of the CPU time are needed to obtain one point of the APES. In the case of 5 gaussian bases and the same number of relaxing ions, about 2.5 hours of the CPU time are needed to obtain one point of the APES. The APES is plotted with about 20 points.

The CPU time needed to calculate the interionic potential with the Gordon-Kim method (also IBM(CMS)) depends on the number of the bases of the wavefunctions and the orders of the Gauss-Laguerre and Gauss-Legendre quadratures. For the interionic potential of In^{3+}-F^{-}, with the order of 80 for the Gauss-Laguerre quadrature and the order of 48 for the Gauss-Legendre quadrature, 7.5 seconds of CPU time is needed to get a point.

Chapter 3. Results and Discussion

In this work we have studied the structure of the impurity states in CdF_2:M^{3+} (where M = In, Ga, Y and Sc). The results have been published [40, 41]. The total energy of the impurity system was calculated as a function of the nearest M^{3+}-F^- distance. We have found a bistable defect system for In and Ga and a single shallow level system for Sc and Y in agreement with experimental observations. The calculated adiabatic potential energy is obtained for the four impurities, with the nearest M^{3+}-F^- distance as the configuration coordinate (c.c.). We will discuss in the following the characteristic aspects of both the deep and shallow levels, and analyze the mechanism which leads to either the bistable or the single level system.

3.1 Shallow Levels

When doped with many trivalent metals (In, Ga, Y, Sc and many rare earth atoms), CdF_2 reveals semiconducting properties. These impurities produce stable effective-mass shallow donor states. In all four M^{3+} studies, a shallow level with a very diffuse wavefunction, which is *s*-like, appears. We used two diffuse and one compact Gaussian bases (α=0.005, 0.02 and 0.08) sitting on the impurity to represent the defect electron. In the shallow level, the Gaussian damping factor α=0.005 (in a.u.) of $exp(-\alpha r^2)$ has the largest weight. Table 3.1 gives the characteristic data of the shallow state of the four impurities.

With the shallow state, a large number of atoms which surround the trivalent impurity are subject to partly screened Coulomb field. This has been treated, as

Table 3.1: Characteristic Data of the Shallow States

Impurity		Energy Terms (eV)					Eigenvector $\{c_i\}$ of: $\sum c_i \left(\frac{2\alpha_i}{\pi}\right)^{\frac{3}{4}} e^{-\alpha_i r^2}$ $\alpha_1 = 0.005$ $\alpha_2 = 0.02$ $\alpha_3 = 0.08$		
M	Δ^a(Å)	E_{coul}	E_{rep}	E_{elec}	E_{pol}	E_{tot}	c_1	c_2	c_3
In	-0.15	-24.11	1.40	-2.72	-1.08	-26.52	1.35	-0.09	0.31
Y	-0.11	-23.48	0.94	-2.48	-1.84	-26.86	1.37	0.11	-0.23
Ga	-0.26	-25.32	1.48	-2.72	-1.41	-27.97	1.37	-0.07	0.23
Sc	-0.20	-24.54	0.51	-2.57	-1.51	-28.21	1.29	0.23	-0.25

[a] Δ is the distortion of the first shell around the impurity with regard to the perfect lattice. Negative value means that ions move toward the impurity.

described in Chapter 2, by including a large number of atoms in the cluster. The polarization energy of all four cases in the shallow state are expected to be large, from Table 3.1, we see that it ranges from -1.1 eV (In) to -1.8 eV (Y). The first shell ions surrounding the impurity displace from the perfect lattice sites toward the impurity due to the Coulomb attraction, it is about 0.15Å for In and Y, and 0.24Å for Ga and Sc, respectively. The lattice "collapses" toward the impurity. The displacements of the second and the third shell ions are small.

The lattice distortion and "collapsing" mentioned above are relative to the perfect lattice. It is more conventional to associate a large relaxation with the deep localized state. For this reason the bottom of the ionization state is chosen as the reference, e.g. in c.c. diagram. With respect to this reference, there is no lattice relaxation for the shallow level. Actually when $M^{3+}+e^-$ shallow donor is ionized, one does not expect appreciable difference in displacements of the lattice atoms between the shallow and the ionized state. Experimentally, the ionization of the shallow state of In donor is accompanied by only a very small Stokes shift [16]. Within the extended-ion approach, it is not straightforward to define the ionized state. As an estimate of the equilibrium configuration of ionized states, we kicked out the electron from the impurity system, and then calculate the adiabatic potential energy as a function of the displacement of the lattice atoms. Displacements at minima of ionization states and shallow states for all the four impurities are shown in Table 3.2. One can see that in all the four cases the displacement at the minima of both the shallow level and the ionization state are either exactly the same or very close. So that as commonly used in the c.c. diagram, we have taken the equilibrium lattice configuration of the shallow state as the reference. The strong defect-lattice coupling of the localized deep state will be described relative to this reference. Also from Table 3.2 one may notice that the equilibrium configuration of the ionization states are the same for In and Y, and so it is for Ga and Sc. This mainly results from the pair potential of M^{3+}-F^-. As described in Chapter 2, In^{3+}-F^- and Y^{3+}-F^- have almost the same pair potential, and so do Ga^{3+}-F^- and Sc^{3+}-F^-.

Ordinarily, such a diffuse shallow level is a proper subject of the effective mass approximation (EMA). It is assumed in the EMA that the amount of localized charge of the impurity electron remaining in the region of the short-range potential is so small that the conditions imposed by the character of the solution of the Schrödinger equation in that region are irrelevant, then the problem is reduced to that of a hydrogen atom. In the limit of a very large electronic orbit (the effective Bohr radius of about 20Å), the impurity electron is bound by the attractive force of the long range (Coulomb) part of the potential V which behaves as $\sim (\varepsilon r)^{-1}$, where V is some effective impurity potential which is usually centered at the site of the defect, ε

Table 3.2: Lattice Displacements of Ionization States and Shallow States

Impurity	The First 3 Shells' Distortion (Å) (Ionization)			The first 3 Shells' Distortion (Å) (Shallow Level)		
M	1st	2nd	3rd	1st	2nd	3rd
In	-0.11	0.05	-0.01	-0.15	0.03	-0.03
Y	-0.11	0.05	-0.01	-0.11	0.05	-0.01
Ga	-0.20	-0.01	-0.05	-0.26	-0.05	-0.06
Sc	-0.20	-0.01	-0.05	-0.20	-0.01	-0.04

Negative value of distortions means that ions move toward the impurity.

is the static dielectric constant of the host crystal which is typically of the order of 10 in semiconductors. Substantial spatial delocalization implies extreme localization in the wave vector space. Consequently, the wavefunctions can be thought of in terms of a product of a slowly varying envelop function $F(r)$ and a periodic function derived from the nearest band minimum. Near the band edge, the crystal Hamiltonian can be approximated by the effective mass parameter (m^*) familiar from the nearly-free-electron model. The ground state energy is $Z^2m^*/\varepsilon^2(Ry)$, and the effective radius of the wavefunction is $\varepsilon/(Zm^*)$ times the Bohr radius of hydrogen. The hydrogenic model has been very successful in providing a good overall picture of the effects associated with the so-called shallow donors and acceptors, where the potential V is dominated by its long range (Coulomb) term. The fundamental properties of the electronic states described by the hydrogenic model are insensitive to the atomic and chemical signatures of the defect. The effect of the surrounding lattice upon these states can be accounted for in terms of a small number of macroscopic parameters

(m^* and ε) peculiar to the host crystal in question. When the short range potential is considered, the ground state energy of the shallow states are corrected for polaron and central cell effects. The variation of the ground state energy reflects the chemical nature of different impurities.

The localized deep states are not amenable to treatment within the EMA. The extented character of the hydrogenic wavefunction is a manifestation of the long range character of the screened Coulomb potential which is the main source of binding. The contraction of the impurity wavefunction and, consequently, an increasing importance of the short range interactions breaks the hydrogenic model down. The deep level problem can only be solved if there are suitable means of solving the Schrödinger equation with a strong, short range term in the potential V. As we intended to compare the two levels, which are produced by the same defect center, with details of the structure, we had to study it within the same extended-ion method.

We noted some difference from the picture given by the conventional EMA. For example, we do not notice a simple chemical shift among the four impurities. However, electron energies in all four cases are close, they range from -2.48 (Y) to -2.72 (In, Ga) (see Table 3.1). And there is some affinity between In and Y, and also between Ga and Sc, for In and Y (Ga and Sc) are in the same row in the Periodic table. One can see from Fig. 3.1 and 3.2 that In and Y donors create similar adiabatic potential energy surfaces (APES) of the shallow state, and from Table 3.1 that at the shallow level, the total energies as well as lattice distortions (relative to the perfect lattice) for both cases are very close. From Fig. 3.1 and Fig. 3.2 and Table 3.1 the same situation can be found for Ga and Sc donors. There are factors which go beyond the conventional EMA in the present study. First, there is the pair

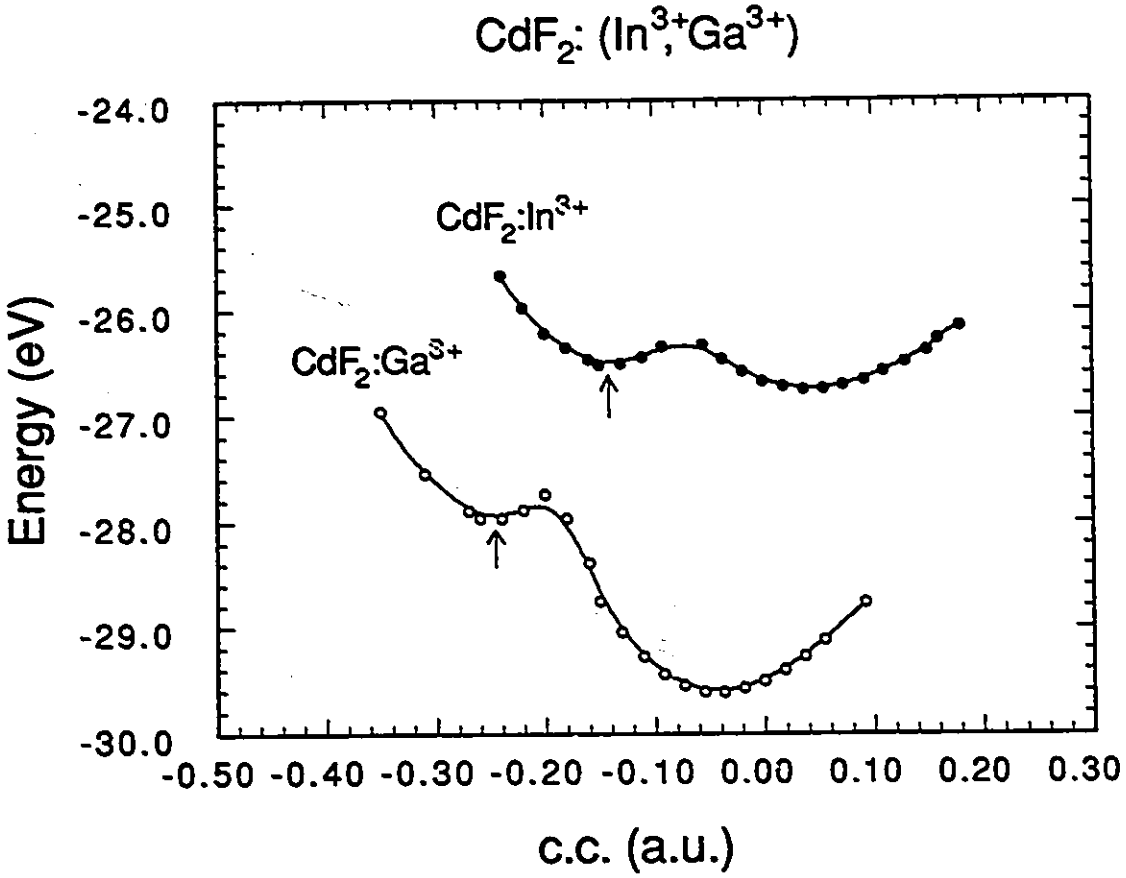

Figure 3.1: The APES of CdF$_2$:(In^{3+}, Ga^{3+})

Potential energy curve for CdF$_2$:(In^{3+}, Ga^{3+}). Total energy of the system as a function of the nearest M^{3+}-F$^-$ distance (c.c.). The arrows indicate the ionization limit. By measuring the distortion from this point, it can be seen that a large relaxation is associated with the deep level.

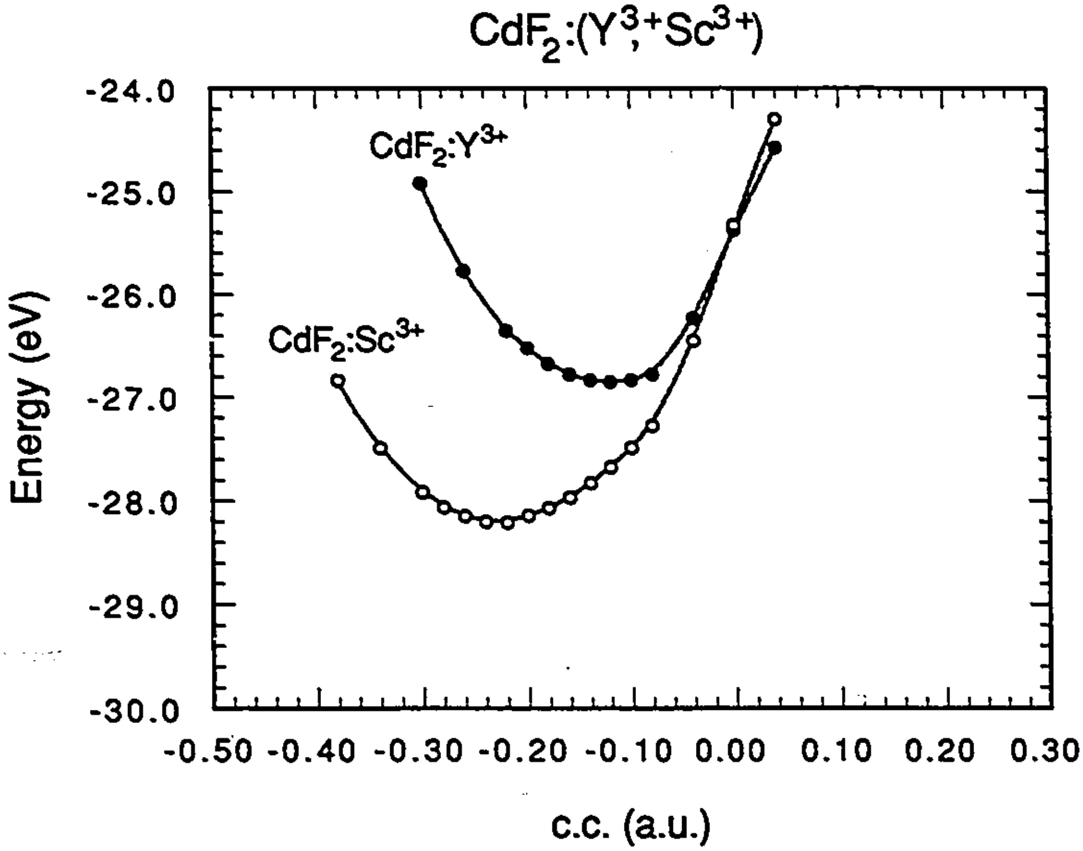

Figure 3.2: The APES of $CdF_2:(Y^{3+}, Sc^{3+})$

Potential energy curve for $CdF_2:(Y^{3+}, Sc^{3+})$. Total energy of the system as a function of the nearest M^{3+}-F^- distance (c.c.).

potential for M^{3+}-F^- which we determined separately for each of the four dopant atoms with the Gordon-Kim approach. The short range extended-ion parameters, which is represented by the central cell correction in EMA, and the electronic polarization are also different. Although the shallow level wavefunctions are diffuse in all cases, they differ in detail when the eigenvectors are examined.

3.2 Deep Levels

All defect states in semiconductors can be fairly safely divided into two groups. The first is formed by effective mass states as described above, while the second by the so-called deep states. The most significant difference between them is the electron wavefunction localization. The Bohr radius of the first group is of the order of simple hydrogenic estimations, $a \approx 20$Å. For the second group of states, good knowledge of the wavefunction is scarce, but there is quite substantial experimental evidence that the deep states are localized. For example, in the absorption spectrum of CdF_2:In^{3+} (Fig. 1.2) the VIS band (corresponding to deep states) is much broader than that of IR band (corresponding to shallow states). This reveals the localized feature of the deep state. Generally, a localized state has strong coupling to the atomic vibration of the surrounding atoms and leads to broad optical absorption or luminescence bands. In a semiconductor the Bohr radius of deep states is of the order of the interatomic distance [42].

With In and Ga replacing a host Cd atom, we obtained beside the shallow level one deep level with a compact wavefunction (also s-like). The Gaussian damping factor α=0.08 (in a.u.) of $exp(-\alpha r^2)$ has the largest weight. Corresponding to the deep level, the displacement of lattice atoms is almost negligible. The lattice responds as if to a In^{2+} (or Ga^{2+}) ion. The electronic polarization is also quite small,

$\approx$ -0.1 eV. We have mentioned that the deep level wavefunction is also s-like, since the ground state configuration of In^{2+} and Ga^{2+} are $[Kr]4d^{10}5s^1$ and $[Ar]3d^{10}4s^1$, respectively. In the calculation of the adiabatic potential energy as a function of the lattice configuration, the Gaussian bases were set to form s-like wavefunctions for both the shallow and the deep states.

The deep state is the consequence of strong lattice-defect vibronic coupling. The delocalized states couple predominantly to the optical modes, while the localized states, to large k-vector (predominantly acoustic) modes. A dramatic increase of the strength of the electron-phonon coupling for localized defects may lead to quite unusual phenomena known as the Large-Lattice-Relaxation (LLR). From the different lattice configurations of the shallow and deep states one can see that an electron transfer from the localized state to the delocalized shallow state produces a large symmetrical lattice collapse around the impurity, it is the so-called LLR. From the experimental data, U. Piekara and J.M. Langer [5] estimated that the lattice relaxation, $Q_d - Q_s$, between the deep and the shallow state is about 10% of the lattice parameter. Where Q_d is the nearest M^{3+}-F^- distance of the deep level, and Q_s is the one of the shallow level. Our calculation gives the relaxation $(Q_d - Q_s)$ of about 7.9% of the lattice parameter for In, and 9.5% for Ga, respectively, both are close to the estimate. It is also in agreement with experiments that the lattice relaxation is larger for Ga. The experiment shows that UV-VIS absorption band of Ga is almost 1 eV higher than that of In, and the ground state of Ga is thermally 0.1 eV deeper than that of In. Ga has therefore even larger Stokes shift.

The electronic energy of the s-like electron is about -8 eV which is to be compared with the -28 eV in the free atomic state. This rise in energy is principally due to the lattice Madelung energy (which is $\approx$ 20 eV at the cation site). Table 3.3 shows some

Table 3.3: Characteristic Data of The Adiabatic Potential Energy of the Bistable System CdF_2:M^{3+} (M=In, Ga)

			Energy Terms (eV)					Eigenvector $\{c_i\}$ of: $\sum c_i N_i e^{-\alpha_i r^2}$ $\alpha_1 = 0.005$ $\alpha_2 = 0.02$ $\alpha_3 = 0.08$		
M		Δ^a(Å)	E_{coul}	E_{rep}	E_{elec}	E_{pol}	E_{tot}	c_1	c_2	c_3
In	S	-0.15	-24.11	1.40	-2.72	-1.08	-26.52	1.35	-0.09	0.31
	D	0.04	-19.12	0.17	-7.72	-0.09	-26.76	-0.26	0.18	-1.63
Ga	S	-0.26	-25.32	1.48	-2.72	-1.41	-27.97	1.37	-0.07	0.23
	D	0.04	-20.36	0.01	-9.07	-0.19	-29.61	0.38	0.77	-1.98

S for shallow and D for deep.

[a] Δ is the distortion of the first shell around the impurity with regard to the perfect lattice. Negative value means that ions move toward the impurity.

characteristic data, such as the spatial extension of the electron wavefunction (α of $e^{-\alpha r^2}$ with the largest weight), the relaxation of the M^{3+}-F^- separation, electronic polarization energy and the total energy of the system, corresponding to the shallow and deep levels in CdF_2:In^{3+}, Ga^{3+}.

A potential barrier between the shallow and deep levels is seen in both CdF_2:In^{3+} and CdF_2:Ga^{3+}. It seems rather low, although it is not possible to attach with great confidence to the value obtained ($\approx$ 0.1 eV). On the other hand, the energy difference between the shallow and deep levels is found to be about 0.2 eV in CdF_2:In^{3+} from Table 3.3. This value is in qualitative agreement with the one reported in Ref [10]: 0.11 eV. In the case of CdF_2:Ga^{3+}, there is no reported experimental value available. However, the energy difference obtained Table 3.3 seems too large. Although we were successful in reproducing the observed trend in the four trivalent impurities regarding the presence of deep levels, our predicted energy difference between the shallow and deep levels is not in quantitative agreement with the experimental data. This may be attributable at least in part to the difficulty of studying a shallow center with atomistic discrete defect approach.

3.3 Mechanism of Existence of Deep Levels

First we analyze the variation of energy terms, and then discuss the mechanism of the existence of deep levels. Table 3.4 gives details of energy terms (Coulomb, repulsion, electron, polarization and total energy) and defect electron wavefunction varying with the lattice configuration for CdF_2:In^{3+}. In the table the lattice configuration is represented by the distortion of the first shell surrounding the impurity. The first shell's distortion ranges from $\approx$0.24Å toward the impurity (noted as -0.24Å) to $\approx$0.18Å away from the impurity (noted as 0.18Å). For a fixed first shell's position, the second and third shell positions are those minimized to give the lowest total energy. As the first shell's configuration changes from -0.24Å to -0.11Å (the position of shallow level), the Coulomb energy increases, while the repulsive energy decreases with less distortions. The electron energy remains almost the same as the wavefunction remains very diffuse. Considering the effective-mass large-radius character of the shallow level and its weak coupling to the lattice, the change of the lattice configuration is not supposed to much affect the electron energy. The polarization energy also decreases but slower compared to the change of the Coulomb and repulsive energies, which is mainly because of the change of the lattice configuration.

As the first shell's position reaches the area of the potential barrier (from -0.091Å to -0.055Å), the displacement of the second and third shells suddenly changes the direction, which causes a precipitous increase and decrease of the Coulomb and repulsive energies, respectively. At this point the defect electron starts to be localized on the impurity. This is reflected in the electron energy, it gets much deeper; the polarization energy, its value becomes very small; and the wavefunction, the Gaussian damping factor which has the largest weight jumps abruptly from α=0.005 to α=0.08.

After the area of the potential barrier, (the first shell's position from -0.037Å to 0.18Å) the electron wavefunction remains compact, which indicates a localized state. The value of the repulsive energy and the polarization energy first gets smaller and then gets larger, the minimum of the value is at about the bottom of the deep state because of the smallest lattice distortion.

Table 3.4: The APES of CdF_2:In^{3+} (1)

The First 3 Shells' Distortions (Å)			Energy Terms (eV)					Eigenvector $\{c_i\}$ of: $\sum c_i N_i e^{-\alpha_i r^2}$ $\alpha_1 = 0.005$ $\alpha_2 = 0.02$ $\alpha_3 = 0.08$		
1st	2nd	3rd	E_{coul}	E_{rep}	E_{elec}	E_{pol}	E_{tot}	c_1	c_2	c_3
-0.24	-0.05	-0.06	-25.02	3.60	-2.77	-1.48	-25.67	1.23	0.21	0.02
-0.22	-0.03	-0.05	-24.78	2.89	-2.78	-1.31	-25.98	1.24	0.18	0.06
-0.20	-0.01	-0.05	-24.69	2.42	-2.72	-1.23	-26.22	1.30	0.07	0.12
-0.18	0.00	-0.05	-24.45	1.96	-2.74	-1.14	-26.36	1.30	0.04	0.18
-0.16	0.01	-0.03	-24.23	1.60	-2.76	-1.08	-26.47	1.31	0.01	0.23
-0.15	**0.03**	**-0.03**	**-24.11**	**1.40**	**-2.72**	**-1.08**	**-26.52**	**1.35**	**-0.09**	**0.31**
-0.13	-0.06	-0.01	-24.02	1.48	-2.71	-1.26	-26.51	1.37	-0.15	0.35
-0.11	0.09	0.00	-24.03	1.87	-2.64	-1.64	-26.45	1.43	-0.26	0.40
-0.09	**0.13**	**0.02**	**-24.21**	**3.13**	**-2.54**	**-2.72**	**-26.35**	**1.51**	**-0.38**	**0.42**
-0.06	**-0.05**	**-0.02**	**-20.76**	**0.26**	**-5.55**	**-0.28**	**-26.33**	**-0.43**	**-0.09**	**-1.39**
-0.04	-0.05	-0.02	-20.36	0.24	-6.09	-0.26	-26.47	-0.38	-0.01	-1.50
-0.02	-0.05	-0.02	-19.96	0.26	-6.64	-0.26	-26.59	-0.33	0.06	-1.57
0.00	-0.03	-0.01	-19.74	0.13	-6.93	-0.14	-26.68	-0.31	0.11	-1.60
0.02	-0.01	0.00	-19.53	0.08	-7.21	-0.08	-26.73	-0.29	0.15	-1.62
0.04	**-0.01**	**0.00**	**-19.12**	**0.17**	**-7.72**	**-0.09**	**-26.76**	**-0.26**	**0.18**	**-1.63**
0.06	0.00	0.00	-18.93	0.22	-7.96	-0.09	-26.75	-0.26	0.22	-1.64
0.07	0.01	0.01	-18.92	0.32	-8.02	-0.11	-26.72	-0.25	0.24	-1.64
0.09	0.03	0.02	-18.75	0.52	-8.24	-0.20	-26.67	-0.24	0.25	-1.63
0.11	0.05	0.03	-18.61	0.81	-8.44	-0.35	-26.59	-0.23	0.27	-1.63
0.13	0.05	0.03	-18.21	0.95	-8.86	-0.38	-26.50	-0.21	0.27	-1.62
0.15	0.06	0.04	-18.09	1.33	-9.04	-0.60	-26.39	-0.21	0.28	-1.61
0.16	0.07	0.05	-17.98	1.79	-9.21	-0.88	-26.28	-0.20	0.29	-1.60
0.18	0.11	0.06	-18.31	2.62	-8.98	-1.49	-26.16	-0.21	0.31	-1.59

Negative value in distortions means that ions move toward the impurity.

Table 3.5: the APES of CdF_2:In^{3+} (2)

(a) Diffuse bases only $\alpha = 0.005, 0.02$

The First 3 Shells' Distortions (Å)			Energy Terms (eV)				
1st	2nd	3rd	E_{coul}	E_{rep}	E_{elec}	E_{pol}	E_{tot}
-0.18	0.00	-0.04	-24.45	1.96	-2.71	-1.25	-26.45
-0.16	0.00	-0.04	-24.14	1.56	-2.75	-1.27	-26.60
-0.15	0.01	-0.03	-23.90	1.24	-2.76	-1.27	-26.70
-0.13	**0.03**	**-0.02**	**-23.69**	**1.04**	**-2.77**	**-1.33**	**-26.74**
-0.11	**0.04**	**-0.02**	**-23.57**	**0.96**	**-2.70**	**-1.44**	**-26.75**
-0.09	0.06	-0.01	-23.37	0.96	-2.70	-1.60	-26.71
-0.06	0.12	0.02	-23.40	2.18	-2.56	-2.77	-26.55

(b) Compact bases only $\alpha = 0.02, 0.08$

The First 3 Shells' Distortions (Å)			Energy Terms (eV)				
1st	2nd	3rd	E_{coul}	E_{rep}	E_{elec}	E_{pol}	E_{tot}
-0.11	-0.10	-0.05	-21.13	1.63	-4.10	-1.01	-24.60
-0.07	-0.07	-0.04	-20.85	0.84	-4.97	-0.55	-25.54
-0.04	-0.06	-0.03	-20.20	0.50	-6.16	-0.35	-26.21
0.00	-0.03	-0.01	-19.74	0.13	-6.90	-0.09	-26.60
0.02	-0.03	-0.01	-19.33	0.20	-7.48	-0.10	-26.71
0.04	-0.01	0.00	-19.12	0.17	-7.77	-0.05	-26.79
0.05	**0.00**	**0.01**	**-18.93**	**0.22**	**-8.03**	**-0.05**	**-26.79**
0.07	0.01	0.01	-18.92	0.32	-8.11	-0.08	-26.78
0.11	0.04	0.03	-18.61	0.81	-8.55	-0.33	-26.67
0.15	0.06	0.04	-18.09	1.33	-9.15	-0.58	-26.49
0.18	0.10	0.06	-18.31	2.62	-9.10	-1.48	-26.27

Negative value in distortions means that ions move toward the impurity.

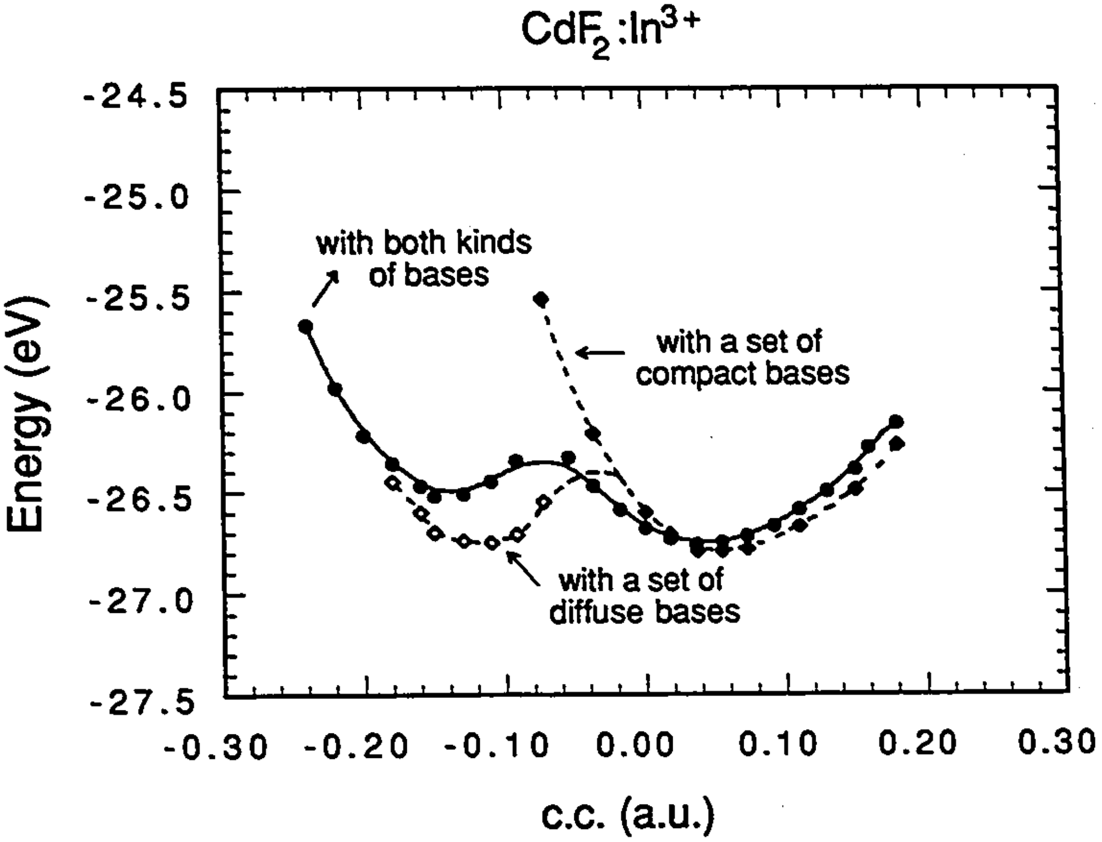

Figure 3.3: The APES of CdF$_2$:In^{3+}

Potential energy surfaces of CdF$_2$:In^{3+} with either a set of diffuse floating Gaussian bases or a set of compact ones, respectively, as well as that with two types of bases. The presence of both types of bases lowers the barrier.

Table 3.6: The APES of CdF_2:Y^{3+}

The First 3 Shells' Distortions (Å)			Energy Terms (eV)					Eigenvector $\{c_i\}$ of: $\sum c_i N_i e^{-\alpha_i r^2}$ $\alpha_1 = 0.005$ $\alpha_2 = 0.02$ $\alpha_3 = 0.08$		
1st	2nd	3rd	E_{coul}	E_{rep}	E_{elec}	E_{pol}	E_{tot}	c_1	c_2	c_3
-0.24	-0.04	-0.06	-25.02	3.54	-2.56	-1.73	-25.78	1.29	0.23	-0.27
-0.20	-0.03	-0.05	-24.47	2.33	-2.56	-1.66	-26.36	1.28	0.24	-0.28
-0.18	-0.01	-0.04	-24.23	1.84	-2.56	-1.59	-26.53	1.29	0.23	-0.27
-0.16	0.00	-0.03	-24.00	1.45	-2.55	-1.58	-26.68	1.30	0.22	-0.27
-0.15	0.01	-0.02	-23.78	1.17	-2.54	-1.63	-26.78	1.30	0.21	-0.27
-0.13	0.03	-0.02	-23.69	1.02	-2.48	-1.70	-26.84	1.36	0.12	-0.24
-0.11	**0.04**	**-0.01**	**-23.48**	**0.94**	**-2.48**	**-1.84**	**-26.86**	**1.37**	**0.11**	**-0.23**
-0.09	0.06	0.00	-23.29	0.97	-2.47	-2.05	-26.84	1.37	0.10	-0.23
-0.07	0.07	0.01	-23.11	1.11	-2.46	-2.32	-26.78	1.39	0.08	-0.22
-0.06	0.10	0.03	-23.13	1.86	-2.44	-2.99	-26.70	1.42	0.02	-0.19
-0.04	0.12	0.06	-23.06	2.22	-2.42	-3.37	-26.64	1.45	-0.03	-0.17
0.00	0.13	0.08	-22.62	2.68	-2.43	-3.98	-26.35	1.44	-0.03	-0.16
0.04	0.13	0.08	-21.93	2.57	-2.45	-4.08	-25.89	1.42	-0.01	-0.15
0.07	0.15	0.10	-21.50	3.31	-2.47	-4.74	-25.40	1.41	-0.01	-0.14

Negative value in distortions means that ions move toward the impurity.

Near the deep level, the repulsive and polarization energies vary slowly, the main contribution of the change of total energy is from the electron energy, which is getting lower, and the Coulomb energy, which is getting higher. One can clearly see a competition between these two energy terms, which determines the bottom of the deep state. The situation in CdF_2:Ga^{3+} is quite similar. There exists a strong electron-lattice coupling: the bound electron induces LLR (relative to the ionized limit) around itself, which in turn helps to bind the electron. This is similar to the self-trapping in a perfect lattice.

We also calculated the adiabatic energy using only diffuse bases (α=0.005 and α=0.02) for the delocalized shallow state or compact bases (α=0.05 and α=0.08) for the localized deep state. The results are listed in Table 3.5. With only diffuse bases the energy curve was calculated up to the first shell's distortion at -0.06Å (Table 3.5a). As the first shell's relaxation gets larger (in the direction of the deep state), the total energy can not be minimized. The polarization energy starts to blow. Since a delocalized shallow state is not supposed to be accompanied with large lattice relaxation. From Table 3.4, one can see that -0.06Å is just the position of the barrier where the electron starts to sit on the impurity. The shallow level obtained with only diffuse bases: -26.75 eV is deeper than that obtained with both types of bases: -26.52 eV (Table 3.4), mainly because of the larger polarization. The deep level obtained with only compact bases: -26.79 eV (Table 3.5b) is almost the same as that obtained with both diffuse and compact bases: -26.76 eV (Table 3.4), with almost the same lattice configuration.

The adiabatic potential energy surfaces obtained either with diffuse bases only or with compact bases only, as well as that with two types of bases are plotted in Fig. 3.3. The presence of both types of bases lowers the barrier as shown in Fig. 3.3.

We now examine the cases of Y and Sc in CdF_2, where the defect electron can never sit on the impurity to give a deep state. The electron energy remains almost constant and the wavefunction is always diffuse as the lattice configuration changes (the first shell's distortion from about -0.24Å to 0.07Å). Table 3.6 gives details of energy terms and defect electron wavefunction varying with the lattice configuration for CdF_2:Y^{3+}.

We now discuss the factors which contribute to the appearance of the deep level, such as in In and Ga, but not in Sc and Y. It seems reasonable to associate the deep level with the highest *s*-like level of the free M^{2+} ion. From Table 2.11 (Free Ion Energies), these are $[Kr]4d^{10}5s^1$(In^{2+}, Y^{2+}) and $[Ar]3d^{10}4s^1$(Ga^{2+}, Sc^{2+}) levels. For In and Ga, the binding energy is 28.0 eV and 30.7 eV, respectively [33]. In the ionic lattice, an electron at a cation site is sitting on a barrier of the repulsive Madelung potential, which is

$$E_M = -\frac{\alpha_M}{R_{nn}} = 20.3eV \ , \tag{3.1}$$

where α_M is Madelung constant at a cation site of fluorite structure,

$$\alpha_M = -3.27611 \ ; \tag{3.2}$$

and R_{nn} is the distance between the cation and its nearest neighbour F^-,

$$R = 4.391a.u. \ . \tag{3.3}$$

As a rough estimate, the above binding energy can be reduced by 20.3 eV, which becomes 7.7 eV for In and 10.4 eV for Ga. The resulting energy can be compared to the purely electronic energy of the deep level which is (-)7.7 eV and (-)9.1 eV, respectively. Applying the same argument to the case of Sc and Y, one finds from Table 2.11 that the electron energy in the lattice would be about zero. It seems reasonable therefore to argue that the deep level does not show up in the case of Sc and Y due to this internal difference of the two groups of trivalent atoms. In experiments the deep level in the case of Ga is deeper than that in In. This would also be explained according to the internal difference, the binding energy for Ga is larger than that for In. Based on the argument just shown, we predict that Tl^{3+} would show a deep level beside the shallow donor level. Indeed, the binding energy of the 6*s* electron in free Tl^{2+} is about 29.8 eV, close to those in In and Ga. After correcting for the Madelung potential, there would result a deep level comparable to that observed in In and Ga. As we will discuss below, this can be interpreted as the effect of short range potential produced by the impurity atom in the context of the extrinsic self-trapping, proposed by Shinozuka and Toyozawa [14].

According to the fundamental studies of Shinozuka and Toyozawa [14], the self-trapping of carriers in a deformable medium of 3-*d* is characterized by the existence of both free(F) and self-trapped(S) states which are separated by a potential barrier. In the present system involving an impurity center, the F and S states refer to diffuse (EMA) and very compact states, respectively. Toyozawa named such cases as the "extrinsic self-trapping" (impurity assisted self-trapping) to distinguish it from self-trapping in a pure crystal. The basic idea is that a constructive addition of both the short range impurity potential and the electron-phonon interaction leads to the realization of a deep state in a system where such a deep state would not occur with only one element present. The present system is an example of the extrinsic self-trapping.

Using the effective mass approximation, combined with the Fröhlich hamiltonian to represent the electron-phonon coupling, Bednarek and Adamowski have studied the In and Y centers in CdF_2 [43, 44]. They fitted certain parameters, such as the central cell correction and the non-parabolicity of the band, to experimental data of donor ionization energy. They plotted the energy of the system as a function of the decay constant of the exponential wavefunction of the donor state. They obtained two minima for In and only one for Y. Although there are some similar aspects between this work and the present work, it is not clear in the continuum work which factor determines the bistable behaviour and therefore a direct comparison is not straightforward.

3.4 A Candidate Medium for Optical Storage of Information

First we introduce briefly other well-known bistable defect systems. The DX centers [45] observed with various donors in III-IV semiconductors (e.s. AlGaAs or GaAs under pressure) and the E2L centers [46] in GaAs are such examples. It is believed that most donors in III-IV compounds exhibit the usual shallow donor level and also a deeper level, separated by a small potential barrier. Recent first principle's calculations on Si in GaAs, based on the super-cell (or large unit cell) method [47], show that in the charged state (D^-), the deeper level is associated with a large lattice distortion of lowered symmetry. When the highly covalent system is compared with the present system of trivalent impurity centers in CdF_2, some difference appears. In the present work, we noted that both the shallow and deep levels occupy the same symmetry. There is no pseudo Jahn-Teller effect involved with the deeper level, as in the case with the DX center.

The search for novel efficient photorefractive and photochromic media continues for more than two decades because of their potential high storage density [48]. CdF_2

crystals doped with indium may be an efficient medium for optical storage of information in static and dynamic regimes. As we have discussed above the remarkable change in the electron localization at the In impurity during phototransformation leads to a change in the local polarizability. This character will cause a change of the refractive index of the host crystal . Although the impurity phototransformation process proceeds via the conduction band (photoionization of the localized state is followed by a subsequent recapture of electrons by In^{3+} into the delocalized hydrogenic state), the change of the refractive index may be very localized due to a very low mobility of electrons in CdF_2. Therefore a spatial resolution of writing may be in a nanometer range and be limited only by statistical fluctuations in the Indium distribution. The efficient writing of a dispersive grating in CdF_2:In^{3+} has been reported [49]. A similar effect based on defect metastability in AlGaAs epitaxial layers was also reported [50]. There, the change of the refractive index was caused by photoionization of DX centers and metastable photogeneration of free carriers. In the case of CdF_2 the effect is caused by a phototransformation of the impurity itself. In contrast to AlGaAs layers, bulk CdF_2 crystal can easily be grown, therefore it is more suitable for writing thick and multiple holograms. Moreover, CdF_2 offers also a much broader spectral range of scanning the hologram, as compared with AlGaAs.

Part II

Athermal Halogen Atom Desorption

Chapter 4. Introduction

The phenomena of desorption of atoms and molecular species induced by electronic transitions (either by photon or electron stimulation) are studied in a wide range of insulating materials including the ionic halides. The ejecta can be both neutral and ionized species in the ground and excited state. There are possible applications involved, but the fundamental aspects are also important. In this work, we are interested in the energetic desorption of neutral ground state halogen atoms observed in alkali halides KBr and NaBr. Following a recent report, we also investigate the role of indium impurity in KBr in the nonthermal Br^0 desorption. We will also present preliminary works dealing with the desorption of fluorine atoms in CaF_2.

Our work shows that the desorption of halogen atoms is induced by decay of excitons (either Frenkel-type free exciton or the self-trapped exciton) on and near the surface. Since the recent works revealing that the self-trapped exciton (STE, hereafter) in ionic halides is basically a primitive F-H pair and that the substantial relaxation energy associated with the off-center relaxation can be converted to propel the V_k center away from the excited electron which is being localized as an F center, the energetic halogen atom ejection was interpreted as being the consequence of the same relaxation taking place near the surface [51, 52]. Earlier association of the phenomena to the excitonic mechanism originated from the observation made by Townsend and collaborators [53] that the ejected atoms were dominantly along the <110> direction, which is the direction of the halogen ion row in the NaCl lattice. It is in this direction the V_k center is propelled away in the bulk. More recently, however, time-of-flight spectroscopy measurements made by Szymonski *et al.* showed that the ejected halogen atoms from a (100) surface were preferentially along a direction perpendicular to the surface plane. They suggested that this may indicate that the STE mechanism is not involved and a hole localization on the surface might be responsible for the observed direction.

In this section, We will first introduce briefly the study of electron and photon induced desorption, and then introduce the experimental results. At last we will review briefly the instability of STE in the bulk of alkali halides, in which the related concepts such as on-center and off-center STE as well as Robin-Klick parameters will be described.

4.1 Electron and Photon Induced Desorption

There are many kinds of desorption processes. Desorption can be induced by electron beams or ion beams with energy from several keV to MeV. Fast particles cause lots of damage, displace many atoms or ions and stimulate electrons in ion cores into excited states. So desorption induced by fast ions is a complicated process including sputtering as well as different electronic interactions responsible for the composition and final charge state of the emitted particles. Usually inert ions, Ar^+ for example, are used to avoid chemical interactions in the process.

Desorption can also be induced by low energy electrons or photons with energy from 10 eV to keV, commonly called EID, ESD and PSD (electron induced desorption, electron stimulated desorption, and photon stimulated desorption).

When a charged particle slows down in an ionic insulator, in addition to displacing atoms from their lattice positions, it creates electronically excited states (excitons and electron-hole pairs). These initially delocalized excitations can interact with a lattice to form localized excited states, e.g. so-called self-trapped holes and self-trapped excitons. Such localized excitations can subsequently decay nonradiatively leading to defect production in the bulk of the crystal and/or particle emission from the surface. In the particular case of an impinging low-energy electron, according to Franck-Condon principle, the elastic part of the interaction can be neglected, because the projectile's mass is much smaller than that of the target atoms. Similar electronic desorption phenomena have been observed for ultraviolet or X-ray photon irradiation. Such processes provide a unique opportunity to study the electronic transitions responsible for transfer of the excitation energy into the energy of atomic motion leading to surface sputtering.

Generally, electronic desorption processes are of fundamental importance. Alkali halides can be used as model systems for studying these electronic interactions, since they have simple and well-known crystallographic and electronic structures, and the electronic desorption in these materials is very efficient.

Interaction of charged particles and photons with alkali halides have been studied for several decades. We would like to mention the Menzel-Gomer-Redhead (MGR) model introduced in 1964 by Menzel and Gomer [54], and independently by Redhead [55], which was proposed to explain why electronic desorption cross sections are generally much smaller than the analogous dissociation cross sections for gas phase molecules. The model begins with a valence electron excitation. An electron, presumably from a bonding orbital between the desorbate species and the rest of the system is suddenly excited into a non- or an anti-bonding state. As a result of this Franck-Condon excitation, the desorbate species finds itself on a repulsive potential curve and begins to move away from the surface. The main predictions of this MGR picture are that:

1. desorption thresholds should be in the range of energies of bonding-antibonding transitions, a few to say, 20 eV;
2. there should be an isotope effect in desorption, since faster particles which have the same surface chemistry have a better chance of escaping before tunneling or Auger processes vitiate the effects of the initial excitation;
3. the reason that desorption cross sections are low relative to those for apparently analogous gas-phase dissociation processes is that surfaces have available a large supply of electrons for reneutralization of the initially created hole.

However, this model does not offer specific understanding on the ground and excited states potential surfaces. It is hard to confirm if this mechanism is at work in any given case.

In 1983 Townsend [56] concluded that electronic desorption of alkali halides could be adequately understood in terms of what he called the Pooley-Hersh model, which is primarily used for explanation of Frenkel-pair formation in the bulk of alkali halides (Pooley, 1966 [57]; Hersh, 1966 [58]). But it has appeared that neither the primary defect structure and evolution in the bulk, nor the surface emission phenomena were sufficiently known. In the last decade, considerable theoretical development of self-trapped excitons and related defect formation in the bulk has been made, for example, Song's off-center STE model [59]. And now, much more sophisticated experiments performed recently, have provided new insight into the basic mechanisms involved in the electronic desorption of alkali halides. It is the purpose of the present work to understand the mechanism of energetic halogen atom desorption from the point of view of excitonic instability.

4.2 Experimental Results of Alkali Halides Desorption

4.2.1 Desorption from alkali halides of NaCl lattice

Since the early work of Townsend and Kelly (1968) [60], and Palmberg and Rhodin [61], it is known that electron irradiation of alkali-halide surfaces results in the efficient desorption of halogen and alkali atoms.

Halogen atoms desorption from pure alkali-halide crystals

Townsend *et al.* [53] observed that halogen atoms were ejected dominantly along <110> axes at the surface of an alkali halide subjected to electron beam excitation. Attempts to measure angular dependence of emitted species were made. Early techniques [53, 56, 62] could not provide any information about either mass or charge of the different desorbing species that arrived at the collected deposit and stick with various probabilities. In addition, the results were likely influenced by reflected primary electrons. The time-of-flight (TOF) measurements have been performed since 1978 [63, 64, 65, 66, 67]. In 1991, Szymonski *et al.* [67] obtained angle-resolved energy distributions of bromine atoms. The following are main results of TOF measurements.

(1) The neutral halogen atom spectra [63, 68, 65, 67] consist of both a broad peak that has a temperature-dependent maximum and a narrow, higher velocity peak whose energy (at peak maximum) is temperature-independent. The broad peak can be fitted by a Maxwellian energy distribution that is representative of the specimen temperature and is due to thermally emitted particles. The narrow peak is due to the ejection of hyperthermal halogen atoms at ground state, which is only observed in type III alkali halides (e.g. KBr and RbBr, see Fig. 4.2. The maximum of the narrow peak may give the kinetic energy of hyperthermal halogen atoms, which

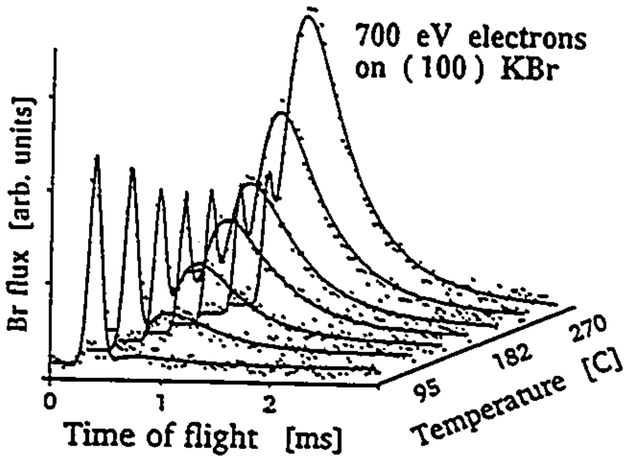

Figure 4.1: Temperatures-Dependent TOF Spectra

Time-of-flight spectra of bromine atoms desorbed from the (100) surface of KBr under 700 eV electron excitation, as a function of temperature. [67]

is 0.25eV in KBr. Fig. 4.1 shows the TOF distributions of Br atoms emitted along the normal to the (100) surface of KBr at several temperatures. The hyperthermal component gives way completely to thermal halogen emission at 350°C. The TOF spectra of halogen atom desorption in 9 alkali halides are presented in Fig. 4.2.

(2) Angular-dependent measurements [67] show that the nonthermal bromine atoms have a strikingly more peaked angular dependence than the thermal ones. As shown in Fig. 4.3, the athermal emission is strongly along the direction normal to the (100) surface.

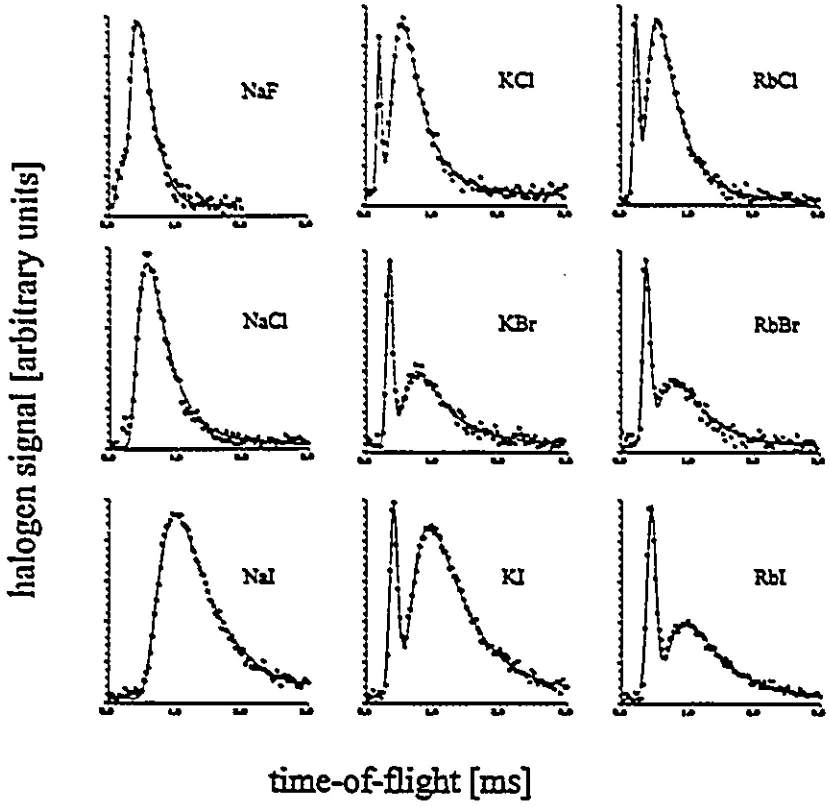

Figure 4.2: TOF Spectra of Desorbing Halogen Atom in 9 Alkali Halides

Time-of-flight spectra of halogen atom desorption in 9 alkali halides from (100) surface [69].

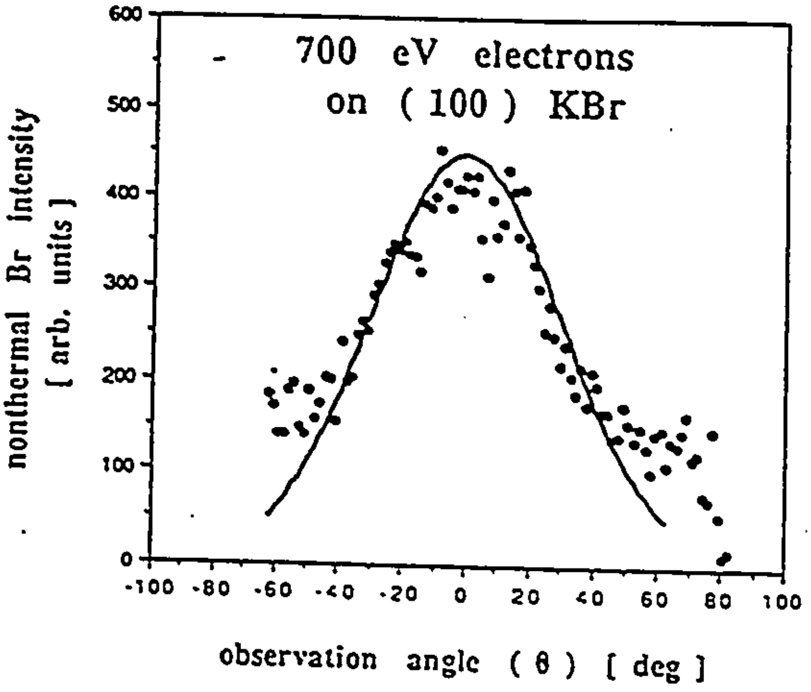

Figure 4.3: Angular Distributions of the Athermal Br Atoms

Angular distributions of nonthermal Br atoms sputtered from a KBr crystal at 140°C. [67], measured in a (010) plane of the (100) KBr crystal.

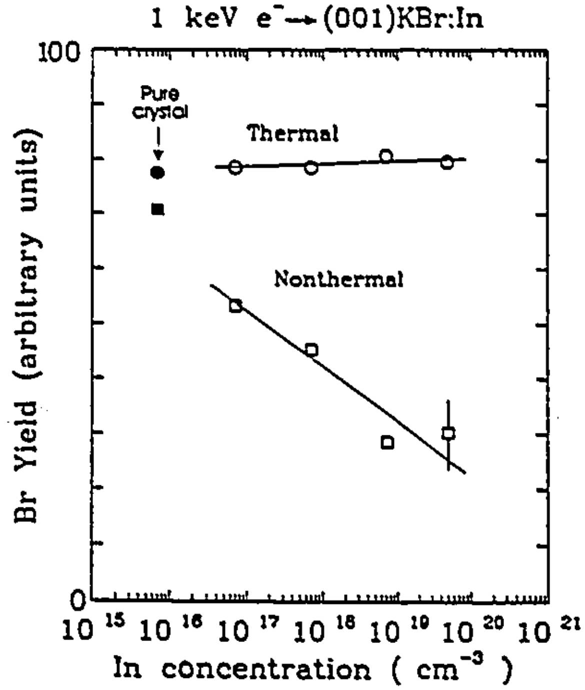

Figure 4.4: Br^0 Yield vs In^+ Concentration

Dependence of the thermal and nonthermal Br^0 yield on concentration in 1 keV electron-irradiated (001) $KBr:In^+$ single crystals. Black markers indicate results for pure sample. The measurements were done at 150^0C. [70]

Halogen atoms desorption from In-doped KBr

To determine the role of hole diffusion in the desorption of nonthermal halogen atoms, Postawa *et al.* [70] measured the kinetic energy distributions of neutral halogen atoms emitted due to ESD from In-doped (001) KBr single crystals. The energy spectra consist of two peaks, the broad one and the narrow one, similar to the case of pure KBr. The distribution of low-energy particles can be described by the thermal (Maxwellian) energy spectrum. Particles contributing to the second peak have nonthermal kinetic energies. Their experiment shows that the emission of halogen atoms having nonthermal energies decreases with an increase in the concentration of In impurities, as shown in Fig. 4.4. At the same time, the emission of thermal particles does not seem to be sensitive to variation of In^+ concentration. At the temperature of the experiment (150°C), In^+ impurities are known to be very efficient traps for migrating holes but not to influence the migration of H-centers. According to their arguments, the obtained results support the model of nonthermal halogen desorption which requires a long range diffusion of holes from the bulk to the surface as a necessary step of the process.

Alkali atom desorption

Most studies of ESD and PSD investigate ground state species, like halogen atom desorption introduced above. Since Tolk *et al.* [71, 72] have first found ESD and PSD of excited-state alkali atoms from alkali halides and proposed an important role of the electronic state in the surface layer, several groups have followed them to confirm the desorption of excited-state alkali atoms under electron bombardment [73, 74]. An interesting result has been reported recently by Hirose and Kamada [75, 76]. They observed that the atomic emission (Na D-line) from the excited desorbed alkali atom is the strongest in the type III materials, such as KBr, and has not been detected from NaBr for example. The atomic emission (Na D-line) due to the transition from desorbed excited state sodium atoms is stronger in NaF than in NaCl, and is too weak to be observed in NaBr and NaI, while the intensity of the atomic emission line from excited state potassium atoms is larger in the order of KI, KBr and KCl (see Fig. 4.5). These results may be interpreted in terms of the lattice instability due to the electronic excitation on and near the surface.

Our brief study of the excited alkali atom desorption preceded by that of a

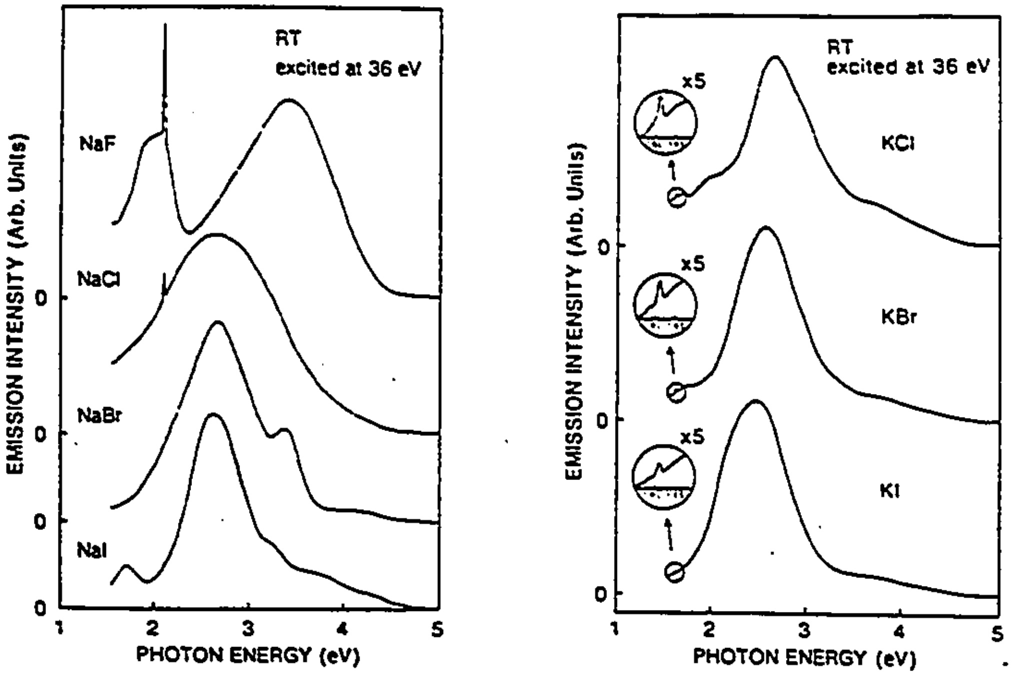

Figure 4.5: Na D-line Emission from Desorbed Excited State Alkali Atoms

A set of emission spectra from sodium halides irradiated with undulator radiation of 36 eV at room temperature. [76]

halogen atom indicated that it is energetically possible if the F center is in an excited state. More details are in Ref. [77].

4.2.2 Desorption from CaF_2 crystals

In CaF_2, desorption of neutral Ca and F, as well as of F^+, is reported [78]. However, no energetic F emission seems to have been established [78, 79].

4.3 The Instability of STE in the Bulk of Ionic Halides

Our study shows that the instability of the STE on or near the surface plays an important role for the athermal halogen atom desorption from KBr, RbBr and CaF_2.

4.3.1 On-center and off-center models of the STE

Reflectance and absorption spectra often show structure at photon energies just below the energy gap. This structure is caused by the absorption of a photon with the creation of a bound electron-hole pair. An electron and a hole may be bound together by their attractive Coulomb interaction just as an electron is bound to a proton to form a neutral hydrogen atom. The bound electron-hole pair is called an exciton, which can move through the crystal and transport energy.

Excitons can be found in every insulating crystal. Removal of an electron from the valence band to the nearby conduction band upsets the stability of the lattice. In alkali halides, the hole can be localized to one halide ion. The particular halide on which the hole is localized will no longer be a "hard sphere" with respect to repulsion equilibrium with its neighbors. The most outer shell of a negative halogen ion is a complete p shell. After an electron is removed from the valence band, the incomplete p shell of the halogen atom can form a covalent bond with one of the halide neighbors, forming a dimer X_2^- molecule ion in the crystal. It is the so called V_k center. Then a STE results when the excited electron becomes bound to the site of the V_k center in a relatively loose orbital. This is the first model of the STE as proposed originally by Kabler [80], after he demonstrated that the recombination of an excited electron with the V_k center results in the same emission band as the intrinsic luminescence. This on-center (V_k+e) STE model has further been reinforced by optically detected ESR studies which showed in many alkali halides that the hyperfine structure was very similar to that of the V_k center itself, with the spin Hamiltonian parameters clearly correlated. Subsequent analyses of exciton spectroscopy (luminescence, transient absorption and magnetic resonance etc···) have all been conducted on the assumption that the STE in alkali halides has the same structure as that of the V_k, except possibly in some details. Earlier theoretical calculations [81, 82, 83] were based on this on-center model.

The excited electron and the hole would normally have opposite spins and the STE would be a spin singlet state. But the spin of the excited electron may flip because of the spin-orbit coupling or the interaction with nuclei. Because of this, an STE may be either singlet or triplet and the triplet state is generally lower in energy. The intrinsic recombination luminescence of the STE is either σ-polarized or π-polarized (the polarization is parallel or perpendicular to the axis of the V_k center, respectively). The σ luminescence bands have lifetimes in the range of nanoseconds, and the π luminescence bands have lifetimes ranging from 90 ns in NaI up to 5 ms in KCl [59]. The σ-bands originate from the radiative decay of singlet state of the STE, and the π-bands arise from the triplet state [84]. Because of the spin selection

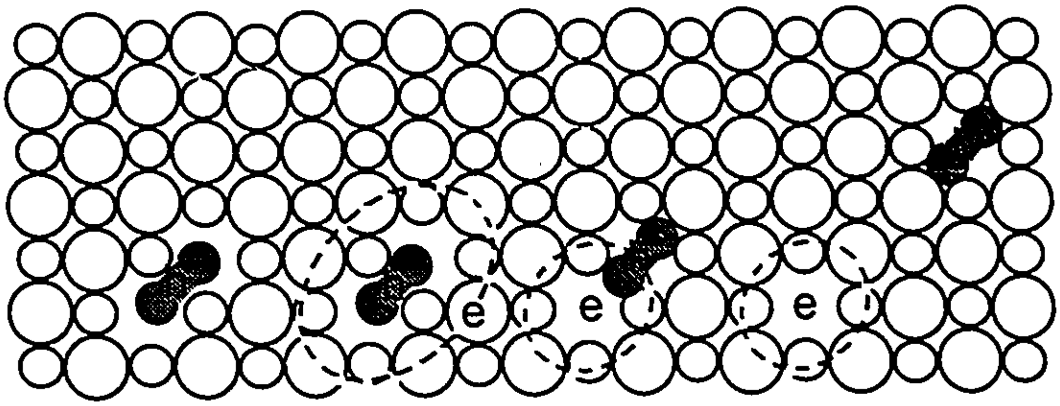

(a) V_k CENTRE (b) $V_k + e$ (c) STE (d) F-H PAIR

Figure 4.6: Schematic Illustrations of STE in Alkali Halides

rule, the triplet lifetime is much longer. Electronic processes are mainly associated with the long-lived triplet state STE.

In 1984, in a series of work [85, 86, 24] Song and collaborators studied the instability of STE using a combined method based on the extended-ion approach and the CNDO (Complete Neglect Differential Overlap) code. Their study showed that the STE is strongly unstable in the configuration of the on-center (V_k+e, D_{2h} symmetry) geometry. The V_k core suffers an axial translation along the <110> axis. At the same time the surrounding ions undergo relaxation of the same symmetry, i.e. C_{2v}. The excited electron charge density is concentrated on the nascent anion vacancy after the V_k core slips to one side. The electron and hole charge density of the STE therefore split in space and the resulting structure of the STE is more like a primitive F-H pair. The charge distribution on X_2^- becomes polarized, such that the hole and electron attract each other. Fig. 4.6 illustrates the variation of the geometries from a V_k center to a F-H pair.

Recently, *ab initio* Hartree-Fock methods have become available to handle defect systems like the STE in alkali halides. This method is still in the trial stage for such complex defect as STE. Some preliminary results have been obtained with two independent codes, ICECAP (Ionic Crystal with Electronic Cluster: Automatic Program) and CADPAC (Cambridge Analytic Derivatives Package) [87, 88, 89, 90], both support the off-center model. The adiabatic potential energy surface (APES) of the triplet STE as a function of the axial shift ΔQ_2 along the <110> axis are shown for some typical materials obtained using the extended-ion approach [91], in Fig 4.7, and using *ab initio* Hartree-Fock method [88], in Fig. 4.8.

The basics of this lowered symmetry of the off-center STE relative to that of the V_k center has been described in recent literatures [51, 59, 92]. In short, the driving force of this large photo-chemical reaction is in the excited electron. The excited electron which is in a diffuse orbital around the self-trapped hole when in the highly excited state becomes localized on the nascent anion vacancy as it reaches the lowest triplet state. In fact the excited electron is so strongly attracted by the half anion vacancy that it can easily displace the molecule-ion core X_2^- along the <110> row accompanied with appropriate relaxation of other surrounding ions. It was believed that on going from on-center geometry to off-center geometry, the STE, which moves toward a nearest halide neighbour, needs to overcome the nearest neighbour alkali repulsive barrier [83]. However, the excited electron gains more than adequate energy by localizing on an anion vacancy site. Recent calculations based on various method show that the energy gained by this lowered symmetry (as the STE transform from the on-center D_{2h} to off-center C_{2v} symmetry) is about 1

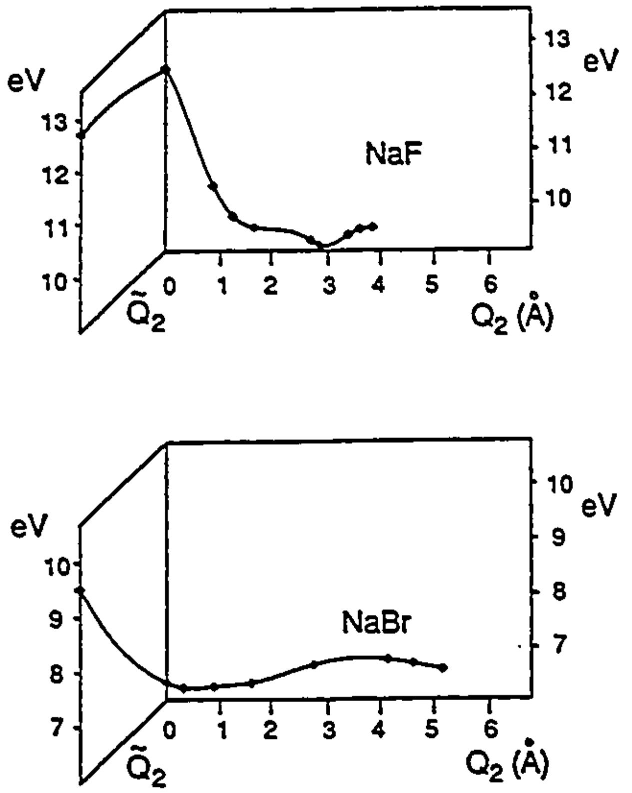

Figure 4.7: The APES of the Triplet STE with the Extended-Ion Method

The adiabatic potential energy surface (APES) of the triplet STE in NaF and NaBr, obtained by the extended-ion method [91]. Q_2 represents the axial translation of the molecule-ion from the original V_k center position.

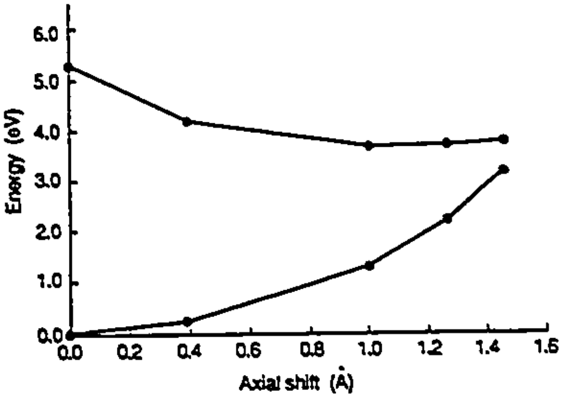

(a) NaF

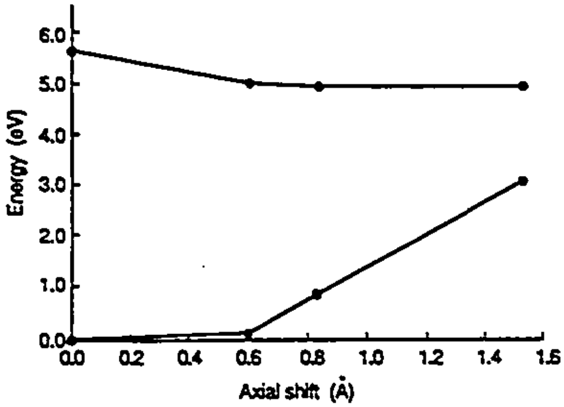

(b) NaBr

Figure 4.8: The APES of the Triplet STE with *ab initio* Method

The APES of the triplet STE in NaF and NaBr, obtained by all-electron Hartree-Fock method (CADPAC code) [88]. (Also the ground state APES is shown).

eV, but depends on the method used [59].

The axial shift and the relaxation energy gain along the <110> axis in NaBr and NaI seem smaller than in NaF and other fluorides, KCl, RbCl, KBr and RbBr. It is found that the degree of the off-center relaxation depends on the host lattice parameter related to the size of X_2^-.

4.3.2 The Rabin-Klick diagram

In order to explain the strong material dependence of low temperature F center yield, Rabin and Klick [93] have introduced a geometrical parameter which is known as the Rabin-Klick parameter S/D. The parameter S, illustrated in Fig. 4.9, is the separation of two adjacent halide ions along a <110> row minus twice the halide ion radius, i.e. the "excess space" measured between hard spheres placed at the ion positions. D is the diameter of the neutral halogen atom. The ratio S/D was originally proposed as a geometric measure of space available for the insertion of an interstitial halogen atom to form an H center, or now in the present context, is the space for the STE to relax off-center. Fig. 4.10 is the plot of the Stokes shift against Rabin-Klick parameter S/D. According to the relative magnitude of the Stokes shift, these alkali halides are divided into three distinct classes by Kan'no *et al.* [94]. NaI, NaBr belong to type I, NaCl and a few others belong to type II, and KBr and others form type III.

Fig. 4.11 shows the original Rabin-Klick diagram of the low temperature F center formation yield, in which the logarithm of energy per F center formed at 4.2 K is plotted versus the Rabin-Klick parameter S/D. The defect (F center) formation efficiency at 4.2 K is large in crystals with S/D exceeding 0.45, since it is easier for the conversion of STEs to separated F-H pairs in these crystals. Also one may

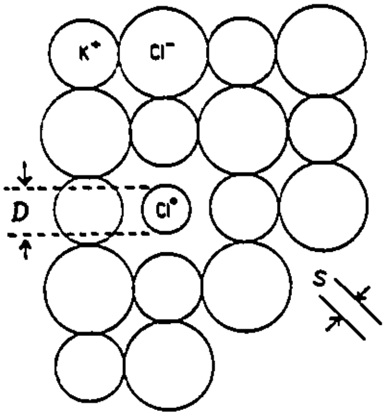

Figure 4.9: Definition of Rabin-Klick parameter S/D

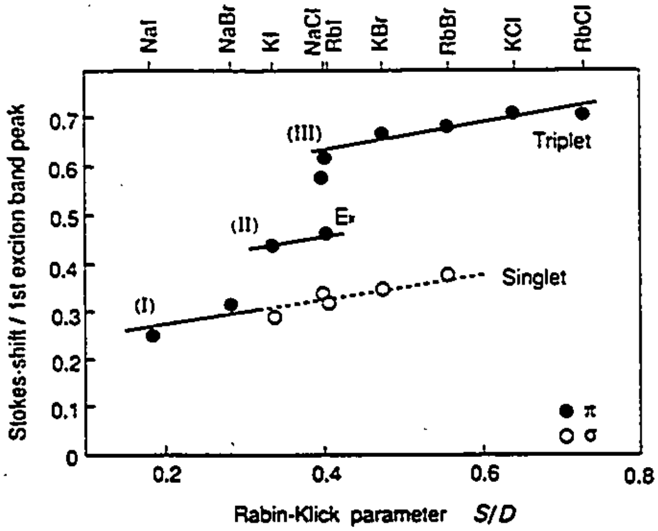

Figure 4.10: Correlation Between π Band Stokes Shift and Rabin-Klick Diagram

Plot of Stokes shift of STE luminescence bands normalized by the energy of the lowest exciton absorption peak vs. the Rabin- Klick parameter S/D defined above. Closed circles denote the π emission and open circles indicate the σ emission. Grouping of the bands as type I, II, and III is indicated [94].

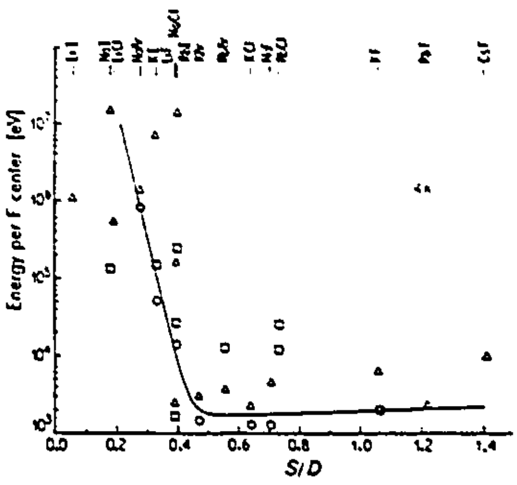

Figure 4.11: Rabin-Klick Diagram of F Center Creation (4K)

Plot of logarithm of the ionizing energy required per stable F center generated at 4K in alkali halides arranged along the horizontal axis according to the value of S/D.

conclude from the trends in this figure that if the lattice is open enough (large S/D) to allow large off-center relaxation of the STE, then any barriers to further separation of the F-H pair are also likely to be small. It is therefore possible that the relaxation of the free exciton or of an excited state of the STE can provide enough directed energy along the separation coordinate to produce stable defects at low temperature.

4.3.3 Understanding of the off-center STE

The various aspects involving the STE are now understood from the point of view of the off-center model.

1. The large variation of the Stokes shift of the π bands (from 76% in NaF to 24% in NaI) is directly correlated to the magnitude of the axial shift. The larger

axial shift leads to a larger Stokes shift. The shift is not directly accessible experimentally, but the calculated shift, called ΔQ_2 as shown in Fig. 4.7 and Fig. 4.8, correlates well with observed Stokes shift [95]. The Stokes shift correlate also with the Rabin-Klick parameter S/D, as Kan'no *et al.* [94] demonstrated. This is not surprising because the magnitude of the axial shift should certainly be a function of the space available in the halogen <110> row for the molecule-ion to move through.

2. Song and Chen found that the triplet lifetime τ can be directly correlated to the axial shift ΔQ_2 in an approximate theoretically derived formula [95]. It is possible to deduce the axial shifts of several STE configurations belonging to the same energy surface, as it has been done in RbI [96] and for NaI under dilatational strain [97].

3. The low temperature F center formation yield which depends strongly on material, as shown in Rabin-Klick diagram [93, 98] can be understood in terms of the available relaxation energy along the reaction coordinate Q_2 which can be converted to kinetic energy of the molecule-ion (the H center). Such mechanism is clearly satisfactory at least qualitatively [91].

4. The thermal channel of F center formation which seems available in all alkali halides with about 100 meV of activation energy is certainly compatible with the calculated APES, both through the extended-ion and the *ab initio* Hartree Fock method. The APES of Fig. 4.7 and Fig. 4.8 suggest no energy barrier of substantial magnitude (of the order of, say 0.2 eV).

At the present time evaluating with great confidence an energy barrier of this magnitude is an extremely difficult task with any calculational method. The extended-ion method we described in Part I has its obvious limitations due to the basic approximations used. It can predict generally correct trends for defects such as the STE. The values of activation energy obtained by such method are qualitative or semi-quantitative at best. However, there is no doubt that well-thought out approximate methods are valuable in exploring complex new defect systems. It is only after such explorations that one can attempt more elaborate calculations, such as the *ab initio* calculations. The *ab initio* approaches have their specific difficulties. The problem of embedding a quantum cluster inside an infinite crystal is a complex one [99]. There are also problems of purely quantum chemical nature which have to be faced in view of the large number of electrons involved in a solid state defect study.

Recent experimental works present direct indications as to the nature and even the detailed environment of the STE. The recently published resonant Raman scattering work [100] shows very clearly that the hole of the STE in NaCl is practically an H center, rather than a V_k center. There is a large difference in the stretching mode frequency of the molecule-ion between the H and V_k centers (366 cm^{-1} vs 243 cm^{-1} respectively). The excited electron of the STE is similar, but with some perturbation, to the F center according to the same work. Similar results are obtained in RbI [100]. Fast spectroscopic studies have shown in RbI [96] that several local minima exist on the triplet STE APES, and there is a transfer of population between them which are observed by time-resolved luminescence studies. Recent femto-second photoconversion studies [101] showed more details on how the excited STE state relaxes to various metastable states before settling to either the π emitting STE state or to F-H pair state. Although some details are not yet clearly understood, such as the possible reorientation of the STE axis during relaxation [102, 103, 104], there is no more any doubt as to the fact that the STE is off-center and practically a primitive F-H pair already and there is no energy barrier of substance between the STE state and other states on the same APES, including well-separated F-H pairs. Recent study of ODESR monitored by magnetic circular dichroism in KBr [105] showed that the correlated Frenkel pairs created at 4K correspond to the 4-th nearest neighbour F-H pairs. By comparing the theory and experiment together in a critical way, one has reached a satisfactory understanding of the STE for the most part [59]. This can be considered as a paradigm of close interplay between experiment and theory.

Chapter 5. Method of Calculation

The method of calculation in this part is basically the same as in Part I. The main difference is that the cluster is made of a number of circular slabs to simulate a surface with possibly an infinite thickness, and the defect consists of a pair of excited electron and hole trapped on a V_k center. The Madelung potential was calculated directly, from the point charges inside the cluster. The short range interaction between ions is treated classically using Born-Mayer type pair potentials. The pair potential constants of alkali halide are well known [106], and are listed in Table 5.1.

The polarization energy in this bulk STE problem is calculated by the Mott-Littleton method of the lowest order as in Ref. [107, 108]. The polarizabilities of Na^+, K^+, Ca^{2+}, Br^- and F^- are listed in Table 5.1.

The electron energy is calculated using the extended ion method (see section 2.3). The deep core ion size parameters, the outer shell short range potential and overlap interpolation parameters for Na^+, K^+, Ca^{2+}, Br^- and F^- [91, 108] are listed in Table 5.1.

In the following, only the elements not covered in Part I will be described.

5.1 Generation of the Surface.

In the present study of desorption, we have used a cluster of ions consisting of ten circular slabs to simulate a semi-infinite surface. This cluster is electrically neutral, the total number of point charges included in it is around 6000. About 500 atoms in the cluster contribute to the electron energy through the short range potential

Table 5.1: Parameters for Na^+, K^+, Ca^{2+}, Br^- and F^-

a: Born-Mayer pair potential coefficients.

	Na^+-Br^-	K^+-Br^-	Br^--Br^-	Ca^{2+}-F^-	F^--F^-
A	50.851	83.265	93.300	70.879	23.856
ρ	0.6198	0.6350	0.5940	0.5290	0.5290

b: Ion size parameters, short range potential and overlap interpolation parameters. Polarisabilities.

	Na^+	K^+	Br^-	Ca^{2+}	F^-
A	6.87800	26.99000	33.91133	26.77859	7.95117
B	0.18600	2.08000	5.01791	1.70488	0.34943
J	-0.00300	2.23000	8.02950	1.93452	-0.00794
K	0.00000	0.23000	1.70585	0.16146	0.00000
J'	0.27800	4.68000	8.75470	3.63728	0.54139
K'	0.00700	0.37000	1.33958	0.23421	0.02252
β_{sc}	1.94900	0.88000	0.30624	1.14560	0.76000
A_{sc}	-4.12410	-5.34450	-4.54650	-5.49402	-3.82315
β_{cx}	1.00960	0.38720	0.19328	0.44400	0.37520
A_{cx}	-4.17637	-2.38390	-2.02488	-2.37786	-2.07188
β_{sovl}	1.25000	0.60000	1.10000	0.65000	0.85000
A_{sovl}	0.15960	0.21148	1.40270	0.12142	0.38138
κ_s	4	4	8	4	4
E_s	-3.07635	-1.96444	-0.67924	-2.82800	-1.06574
β_{povl}	1.25000	1.30000	0.35000	0.65000	1.20000
A_{povl}	0.06681	0.84795	0.44269	0.08017	0.44265
κ_p	6	5	5	4	8
E_p	-1.79715	-1.17109	-0.13320	-1.93000	-0.17442
Polar.	1.95700	8.98000	28.07300	7.42000	4.40000

All parameters are in atomic units. The outer shells for Ions here are only *s* and *p*. E_s and E_p are the energies of the outer *s* and *d* shells, respectively.

energy such as the screened Coulomb and exchange terms. The number of ions explicitly relaxed to minimize the total energy is between two and three dozen, depending on the type of crystal lattice, the surface chosen, and the position where the STE is created initially; the surface, the first, second or third layer. The first layer STE is defined as the one created between the surface and the next plane.

5.2 Parameters of In^+

The parameters of In^+ were obtained in the same way as for In^{3+}. The Born-Mayer pair potential of In^+-Br^- is obtained with Gordon-Kim method [19], (see Sec. 2.2, Append. C). There is no polarisability available for $In^+([Kr]4d^{10}5s^2)$, so we used the one for $Ag^+([Kr]4d^{10})$ instead. Table 5.2 lists the parameters. The deep core ion size parameters, the outer shell short range and overlap interpolation parameters are defined and obtained in the same way as described in Sec. 2.3. The outer shells for In^+ are $5s$ and $4d$.

5.3 Treatment of the V_k Center

The V_k center consists of two anions bound together when a hole is localized. The basic idea of computing the interaction of an excited electron and a V_k center is to keep the treatment of the molecule as close as possible to the treatment of the individual ions to simplify the calculation. In the study of CaF_2, the available F_2^- orbitals from Ref. [109] were used. The fitted parameters previously determined [108] were used here, and are given in Table 5.3 and Table 5.4. For the bromides, we have used the parameters previously used in the study of the bulk STE [91], which are also given in Table 5.3 and Table 5.4. In Ref. [91], Br_2^- was approximated as a pair of Br^0

Table 5.2: Parameters for In$^+$

a: Born-Mayer coefficients and polarisability.

	A	ρ	Polar.
In$^+$-Br$^-$	182.173	0.5977	16.482

b: Ion size parameters.

A	B	J	K	J'	K'
84.08622	17.28261	44.46939	14.76043	39.14369	9.16588

c: Short range potential and overlap interpolation parameters.

	β	A	E(eV)	κ
sc	0.55120	-5.74250		
ex	0.13600	-0.95367		
sovl	0.34800	0.98125	-0.60688	6
dovl	1.10000	0.16348	-1.33167	4

All parameters are in atomic units. The outer shells for In$^+$ are only *s* and *d*. E_s and E_d are the energies of the outer *s* and *d* shells, respectively.

Table 5.3: Short Range Potential Interpolation Parameters for X_2^- (atomic units)

X	β_{sc}	A_{sc}	β_{ex}	A_{ex}
Br	0.43680	-4.76850	0.16928	-1.40554
F	1.10000	-4.13804	0.42667	-2.30630

Table 5.4: Overlap interpolation parameters for X_2^- (atomic units)

X	β_{sovl}	A_{sovl}	κ_s	E_s	β_{povl}	A_{povl}	κ_p	E_p
Br	1.25	1.49650	8	-0.75670	0.25	0.11561	4	-0.20860
F	0.70	0.15134	4	-1.19526	0.70	0.25279	4	-0.30194

E_s, E_p and E_d are the energies of the outer *s* and *p* shells, respectively.

for the calculation of short range terms as the molecular orbitals are not available.

Throughout all of the above discussion, it has been assumed that the V_k center is perfectly symmetrical, *ie.* the hole is shared equally by both ions of the molecule. However, in most cases this is not true as the charge is shifted more to one side than the other, or shared by three ions in a row when the hole jumps from one pair of halide ions to the next pair. One possible way to deal with the hole charge distribution would be to scale all of the parameters in some way from an X^- ion to X^0 (X represents a halogen atom) as the charges shift from one side to the other. We did not attempt it, however.

When the hole diffuses away from the electron (localized on the nascent F center), the Xr_2^- undergoes changes in hole charge distribution and bond length, and sometimes bond-switching. A CNDO (Complete Neglect of Differential Overlap) code was adapted to represent the molecule-ion more precisely, and is interfaced with the extended-ion package in a consistent way. A small number of X^- ions, usually three to five, were treated by the CNDO cluster. The CNDO program determines the change in energy of the molecule bonding which shares the hole and updates the hole charge distribution during the lattice relaxation, which is used in the extended-ion part to calculate the electron wavefunction, the energy and the lattice displacements. It is important to note that the excited electron is directly influenced by the state of the hole described by the CNDO code, especially its charge distribution. At the same time, the excited electron charge density determines the electrostatic potential which acts on the CNDO ions. The entire process was iterated back and forth between the two parts of the program.

The CNDO parameters of Br employed in this work are slightly adjusted from the standard values [110] to fit the observed bond length, vibrational frequency, and the electron affinity of the halogen atom. This last adjustment was made in such a way that the total energies of Br_2^{2-} and Br_2^-, at large internuclear distance, differ by the known value of the electron affinity. The same procedure was used for F_2^-. The CNDO parameters obtained in this way are listed in Table 5.5.

5.4 Minimization Method

In this work, we need to find the minimum energy configuration of the multidimentional space of the crystal. A minimization procedure is developed to solve this problem [86]. We minimize the total energy with respect to individual ion position:

$$E_{tot} = E_{coul} + E_{rep} + E_{elec} + E_{pol} + E_{CNDO} \ ,$$

Table 5.5: CNDO Parameters for X_2^-

X	Orbital exponent (Å^{-1})		electronegativity, $\frac{1}{2}(I+A)$ (eV)		Bonding energy β (eV)
	s	p	s	p	
Br	2.20	2.20	25.20	6.37	-6.90
F	2.11	2.11	37.43	8.66	-11.30

where the various constituent energies have been described in Part I and the previous sections.

We optimize the position of one atom at a time with three degrees of freedom. The same process is carried out in sequence over all ions allowed to move. We then repeat the whole procedure and iterate until the total energy converges within some pre-determined value. Convergence was usually obtained after about 4 interactions, but sometimes it took more iterations to reach convergence.

The V_k center has two ions covalently bonded. In general, the V_k center is displaced by large distances and it usually requires more iterations to reach equilibrium and convergence. Therefore we minimize twice over the CNDO ions before the rest of the lattice is minimized.

To calculate the minimum energy position of the ion, we used the following efficient interpolation scheme, which was developed by Brunet, Leung and Song [86]. First, we interpolate the energy surface to first order of ion displacement:

$$E = a_0 + a_1 x + a_2 y + a_3 z \,. \tag{5.1}$$

This requires the energy to be sampled at four points. In practice we need only calculate the energy at three points since one point can be the energy before the ion is moved, which is obtained from the minimization of the previous cycle. For the other three sampling points we choose three mutually perpendicular directions to avoid problems with linear dependence when we solve the set of 4 simultaneous equations for the coefficients of equation 5.1. We can now calculate the direction and magnitude of the gradient of the energy surface at the point under study.

Then to calculate the minimum energy position of the ion, we interpolate to second order along a line in the direction of $-\nabla E$:

$$E = a + b\delta + c\delta^2 \, , \tag{5.2}$$

where δ is the displacement of the ion in this direction.

Here we need to evaluate the energy at only one more point since we already know a and b (a is the energy at $\delta = 0$ while $b = |\nabla E|$ at $\delta = 0$). Then it is straightforward to determine the position of minimum energy δ_m:

$$\frac{dE}{d\delta} = 0 \ \ at \ \ \delta_m \quad \Longrightarrow \quad \delta_m = -\frac{b}{2c} \, . \tag{5.3}$$

The ion then is moved a distance δ_m in the $-\nabla E$ direction. We reevaluate the energy with the ion at this position and compare it with the other energies that have been calculated in the course of the minimization, and the ion is placed at the position that gives the lowest energy.

In the study of the instability of the STE in the desorption problem, we usually try to find the most likely path for the molecule to move. We first determine the minimum energy direction of the molecule's axis, and then pull the head of the molecule or push the tail of it along the direction (that means some coordinates are restricted to follow a certain path) to calculate the adiabatic potential energy surface. As the molecule moves the V_k center may jump from one pair of CNDO ions to the next.

5.5 The CPU Times

We used the workstation (IBM RS/6000) to calculate the adiabatic potential energy surface (APES) of the desorption. For a typical case, (e.g. 2130 point ions, 420 extended-ions, 26 relaxing ions, 5 CNDO atoms, 2 gaussian bases and 4 iterations) about 1 hour of the CPU time is needed to obtain a point of the APES.

Chapter 6. Results and Discussion

6.1 Br^0 Desorption From (100) Surface of NaBr and KBr

We have selected three bromides as they represent the two distinct classes, as shown in Fig. 4.10. NaBr represents, together with NaI and a few other impurity-associated STE systems, the typical case of *a large molecule in a small cage* (type I according to Kan'no *et al.* [94]). KBr and RbBr belong to the type III and represent the case of *a small molecule in a large cage*. As we described in section 4.3, NaBr on the one hand and KBr and RbBr on the other differ in the magnitude of the off-center shift, off-center relaxation energy, Stokes shift of π band and low temperature F center yield. They are therefore expected to behave differently also in halogen atom desorption. For both bromides, we examined halogen atom desorption in different cases of F and/or H center localizations: free exciton (one-center) on the surface layer, STE (two-center) on the surface layer and the first, second, third layers below the surface. In the following we will report the results obtained for NaBr and KBr, the results for RbBr are almost the same as for KBr [77].

6.1.1 Free exciton and STE decays on the surface

A free Frenkel type exciton is simulated by a Br^0 atom on the (100) surface, with an excited electron bound to it in a perfect lattice. After relaxation, the excited electron localizes on the anion site, thereby becoming an F center. At the same time, the bromine atom on which the hole is localized is ejected normal to the (100)

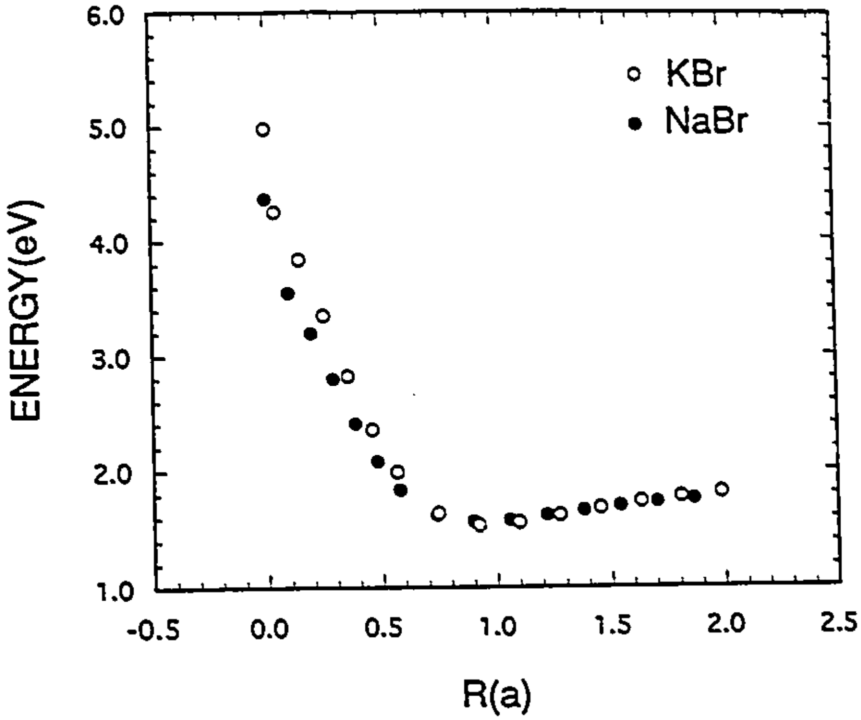

Figure 6.1: The APES of Free Exciton in KBr and NaBr

The adiabatic potential energy surface (APES) of the free exciton decay on the surface in KBr and NaBr. Energy is in eV and the coordinate R (in units of the anion-cation distance) gives the distance between the (100) surface and the bromine atom.

surface with an excess energy of about 2.6 eV in KBr and 3.0 eV in NaBr. The adiabatic potential energy surfaces APES are shown in Fig. 6.1. In both KBr and NaBr, when the bromine is ejected to about one lattice parameter away from the surface, the adiabatic potential energy is at the minimum. As the bromine moves further, the energy rises until the bromine is about two lattice parameters away from the surface, then the APES becomes flat. The energy rising is about 0.25 eV and 0.30 eV for KBr and NaBr, respectively.

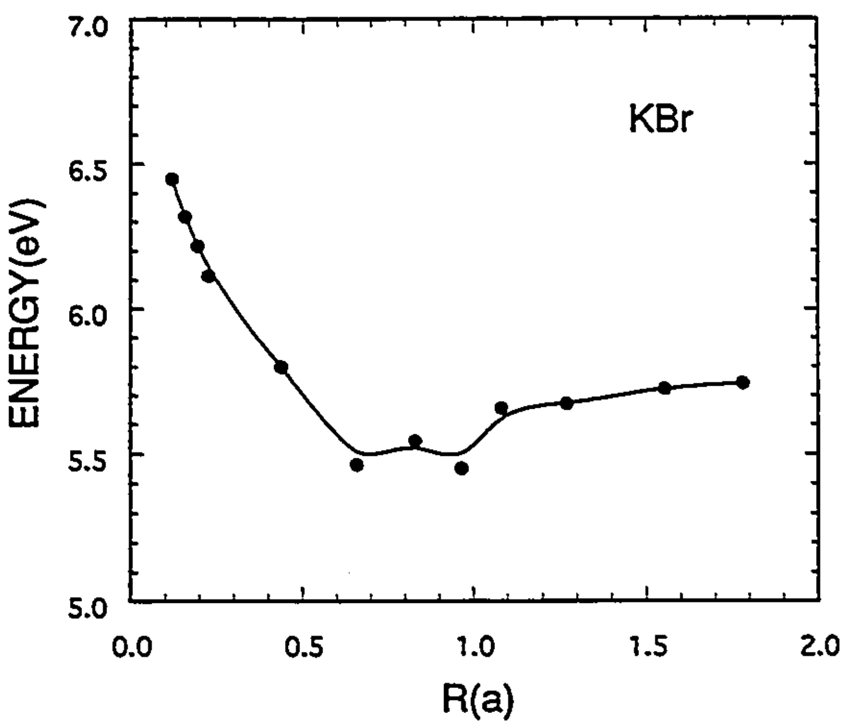

Figure 6.2: The APES of STE on the Surface in KBr

The APES of the STE created on the surface in KBr. Energy is in eV and the coordinate R (in units of the anion-cation distance) gives the distance between the (100) surface and the center of gravity of the hole charge distributed on the bromine atoms.

During the bromine atom's ejection from the surface, the relaxation of the surrounding ions remains small, i.e. less than 5% of the anion-cation distance. As we change the number of ions which are allowed to relax from about one dozen to about two dozen, the relaxation energy remains almost the same within an error of about 0.05 eV. The APES shown in Fig. 6.1 is obtained with two dozen relaxing ions. The floating Gaussian basis (FGO) used in the calculation is $\alpha = 0.04$, for it gives the lowest total energies.

In the absence of the excited electron, the hole localizes initially on one bromine atom, and then very quickly a stable Br_2^- forms on the surface and never leaves the surface. This seems to show that the ejection of the bromine atom from the surface is the direct consequence of the electron localization on the anion vacancy. In bromides, only STE luminescence is observed, therefore, it is uncertain whether free exciton is stable enough on the surface to produce desorption.

STE formed on the (100) surface in KBr and NaBr has also been studied. The two ions chosen to form the molecule are at site (0,1,1) and (0,0,0). In both crystals, during the minimization of the total energy, one of the molecule-ion at (0,1,1) site starts to leave the surface. In NaBr, the hole distribution polarizes slowly, for example, it is 59% and 41% on ion(0,1,1) and ion(0,0,0), respectively, when ion (0,1,1) is 2.33 a.u. away from the surface (the anion-cation distance in NaBr is 5.648 a.u.). It is close to half and half. The bond length of the molecule remains about 5.2 a.u. even when the ion(0,1,1) is 4.73 a.u. away from the surface. In NaBr, the electron and hole do not split as in the bulk. Our study suggests a radiative recombination on the surface. By contrast, in KBr, the hole distribution polarizes very early, it is 72% and 28% on ion(0,1,1) and ion(0,0,0), respectively, when the ion(0,1,1) is 1.8 a.u. away from the surface (the cation-anion distance in KBr is

6.232 a.u.). Also the molecule bond breaks in early stage. Our calculation shows that the STE decays with Br^0 leaving the surface approximately normal to the surface with a kinetic energy estimated to be about 0.4 eV. Fig. 6.2 shows the APES of the STE decay on the surface in KBr.

6.1.2 Near the surface

We have examined the instability of the STE in the first three layers below the surface and calculated APES for these three layers in KBr and NaBr. The configurations of the STE in the three layers are shown in Fig. 6.3. The APESs for KBr and NaBr are shown in Fig 6.4 and Fig 6.5, respectively.

In the bulk, a V_k center in an otherwise perfect crystal is symmetric relative to the mid-point of the molecule-ion. Near a (100) surface we found the symmetry is broken and the hole is attracted toward the surface. According to our work, the excited electron localizes with preference nearer to the surface in the first and second layers below the surface. Further below, the electron is expected to localize either near the surface or away from the surface with equal probability. Fig. 6.3 illustrates the geometry of the STE on the three layers. Only when the off-center relaxation of the STE propels Br_2^- toward the surface can there be a desorption. So that there is no desorption starting from the STE in the first and second layers. This is true in both KBr and NaBr. The STE in the first and second layers relaxes toward the interior and it is expected either to recombine giving off the π band luminescence , or create F-H pair near the surface which may be transient or stable.

Starting from the third layer, the hole on the Br_2^- shows no polarization, and the excited electron could localizes on either anion site. When the excited electron localizes on the deeper site (see Fig. 6.3) in KBr, it leads to desorption with a

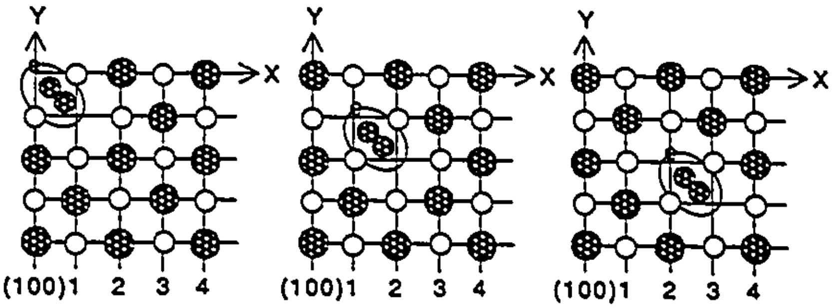

The 1st Layer STE The 2nd Layer STE The 3rd Layer STE

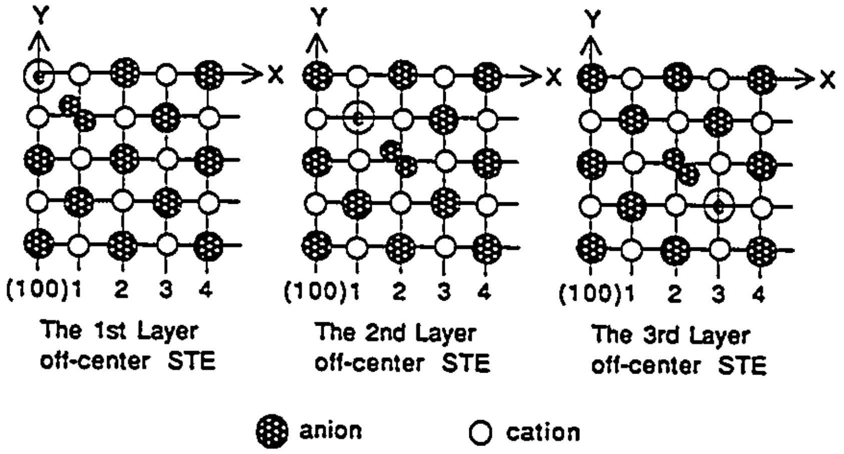

The 1st Layer off-center STE The 2nd Layer off-center STE The 3rd Layer off-center STE

Figure 6.3: Configurations of the STE Near the Surface

The first layer STE is defined as being formed by a pair of Br atoms along the <110> axis, one of which is on the surface and the other on the next plane below it. The subsequent layer STEs are defined in a similar way.

In the first and second layers below the surface, the excited electron tends to localize nearer to the surface. Further below the electron is expected to localize on either site with equal probability. Here we show the electron localizes on the site away from the surface in the third layer STE.

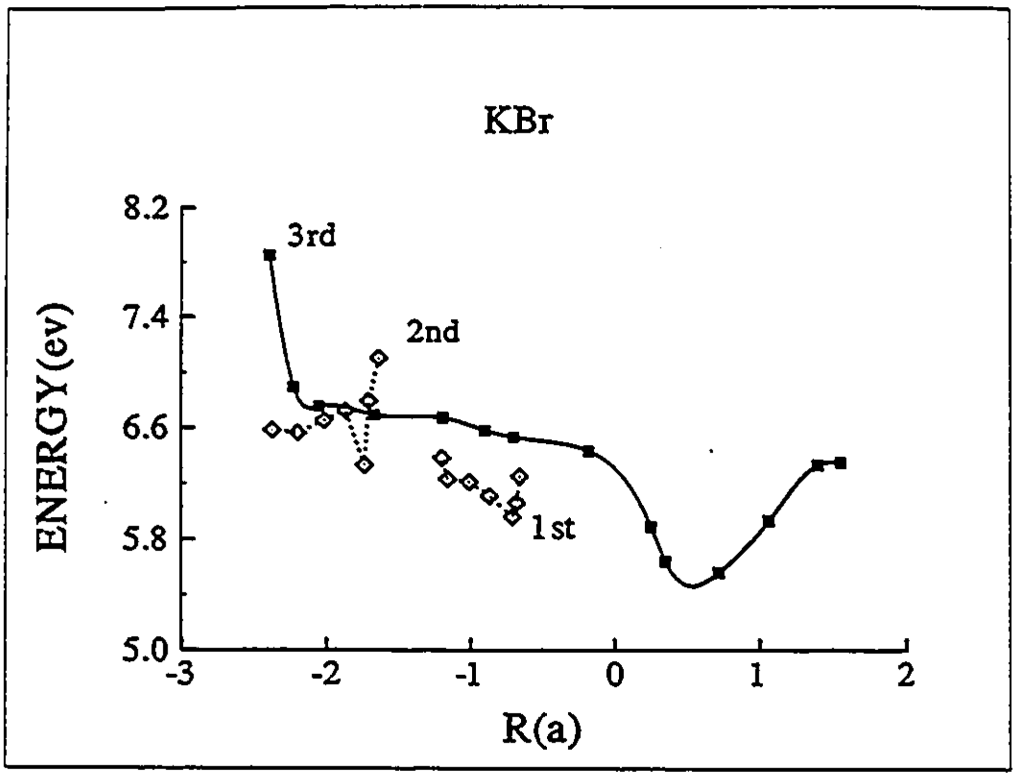

Figure 6.4: The APES of STE Near the Surface in KBr

The APES of the STE created in the first three layers below the (100) surface in KBr. Energy is in eV and the coordinate R (in units of the anion-cation distance) gives the distance between the (100) surface and the center of gravity of the hole charge distributed on the bromine atoms.

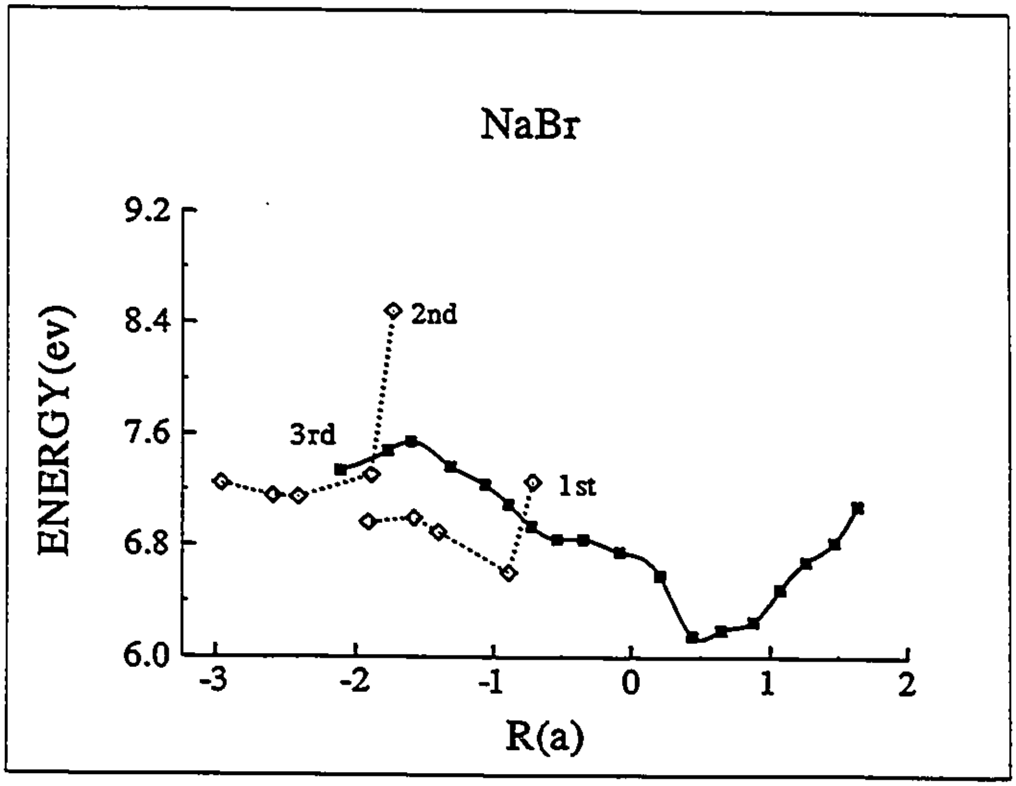

Figure 6.5: The APES of STE Near the Surface in NaBr

The APES of the STE created in the first three layers below the (100) surface in NaBr. Energy is in eV and the coordinate R (in units of the anion-cation distance) gives the distance between the (100) surface and the center of gravity of the hole charge distributed on the bromine atoms.

possible kinetic energy of about 1 eV. In NaBr, although Br_2^- is propelled toward the surface in the third layer, the APES encounters a barrier as in the bulk [24]. No energetic desorption is expected in NaBr therefore. This is in agreement with the experiment [67] according to which there is no energetic emission of Br^0 from NaBr, in contrast to KBr where it is efficient. It has been generally accepted that the energetic desorption of halogen atoms would be observable only in the type III materials, which include KBr. It is interesting to note here that according to a recent ODESR work in KBr monitored via magnetic circular dichroism of the absorption (MCDA) [105], the correlated F-H pairs formed at 4 K correspond to forth nearest neighbours. This seems to indicate that the kinetic energy of the H center propulsion along the <110> direction originating from the relaxation energy on the APES is dissipated when the F-H pairs are about 20 Å apart in KBr lattice. The energetic halogen atom ejection may have to take place from within the first four layers from the surface.

The ejected atom's trajectory is one of our main interest. As described in Chapter 4 (Introduction), Szymonski *et al.* recently performed angle-resolved experiments on electron stimulated bromine atom desorption from KBr, finding that the preferential direction of nonthermal halogen atom ejection is <100>, rather than <110> [112, 67]. As shown in Fig. 4.3, the sharp (non-thermal) peak in the bromine TOF spectrum was found to be preferentially emitted normal to the (100) face of the cleaved KBr crystal and at 45° to the (110) face of a sawed and polished crystal [67]. That is, hyperthermal bromine emission was found to occur in the direction normal to the surface, independent of the cut of the crystal face. The <100> emission direction appears to be in direct contradiction to the findings of Townsend *et al.* [53] and Schmid *et al.* [62] as well as to widely-held expectations based on models for

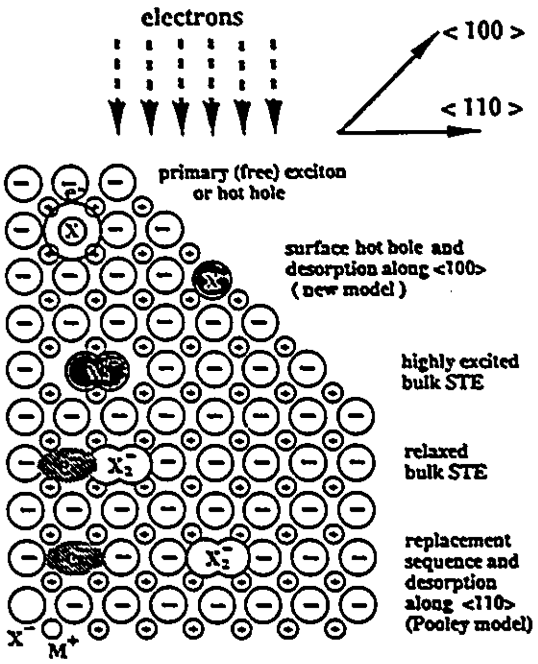

Figure 6.6: Schematic Illustrations of Halogen Atoms Desorption

Schematic illustrations of crystal excitations in alkali halides leading to desorption via the focused replacement sequence along <110> and leading to <100> desorption via outward relaxation of a surface halogen atom having localized a hole according to the model of Szymonski et al. [67].

halogen ejection along the STE molecular bond axis.

The mechanism proposed by Szymonski *et al.* to account for <100> halogen emission is illustrated in Fig. 6.6. They suggested that if a hole is suddenly introduced on a surface halogen ion, the resulting neutral atom will relax away from the alkali neighbours to which it had been electrostatically bonded. The symmetry of the perfect (100) surface dictates that the net direction of such relaxation will be normal to the surface. Our study of the desorption on the third layer below the

(100) surface in KBr shows that, initially, the momentum is given to the molecule-ion Br_2^- in the <110> direction. However, as the atom to be ejected approaches the (100) surface, the axis of the molecule-ion starts a deviation to approach the normal to the surface. After the ejecta has cleared the surface the bromine atom becomes gradually neutral and the trajectory makes an angle of about 10° from the normal to the (100) surface at a distance of about 0.6a (a is the anion-cation distance). Table 6.1 shows the angles between the trajectory and the normal to the (100) surface changing with R (R is the distance between the (100) surface and the desorbing bromine atom). When the distance between the desorbing Br and the surface was larger than 0.6a, the energy surface became fairly soft. It would be meaningless to calculate the direction of the desorbing atom. Although we have not pursued our calculations of the direction beyond that distance, according to the tendency already shown, we expect that the trajectory will eventually become normal to the crystal surface at a macroscopic distance.

The reason for this rotation of the trajectory is to be found in the overall symmetry of the system at this point. Neglecting the perturbation of the F center which is left in the crystal, the ejected atom is seeing an approximately perfect semi-infinite crystal. The ejected bromine atom becomes neutral only at some distance from the surface, about 1.7a. While it leaves the surface, the bromine atom is submitted to both the long range electrostatic as well as the short range fields. It is as a result of these fields that the direction deviates from the [110] axis. Therefore, the model proposed by Szymonski *et al.* [67] according to which the short range repulsion determines the ejection can be integrated with the STE instability model which is needed to initiate the process. The reason that the desorption direction is found to be 45° to the (110) surface may be somewhat different. The (100) face is the only

Table 6.1: Data of Trajectory of Br^0 Desorption in KBr

E_{tot}(eV)	Bond Length (a.u.)	R(a)	Angle(°)
6.60	5.00	0.074	42.7
6.58	5.02	0.136	45.7
6.62	5.01	0.182	45.6
6.53	5.09	0.303	50.6
6.54	5.31	0.397	52.1
6.43	5.62	0.431	37.1
6.26	5.50	0.523	28.9
5.89	5.19	0.569	17.3
5.89	5.15	0.639	9.8
5.64	5.04	0.638	*
5.49	5.19	0.674	
5.74	5.30	1.155	
6.10	5.39	1.476	
6.33	5.61	1.637	
6.35	8.27	1.736	
6.34	9.38	1.877	

The angle is between the trajectory and the normal of the (100) surface. R (in units of the anion-cation distance) represents the distance between the desorbing Br atom and the (100) surface. The table also lists the corresponding total energies of the system and the bond lengths.

*For R being larger than 0.6a, it is meaningless to calculate the angle.

The last two sets of data shows that at the distance of about 1.7a, the bond is broken. After that the total energy remains almost the same (the APES becomes flat).

stable surface plane of a rocksalt alkali halide, so the (110) cut may be a stepwise series of (100) faces at 45° to the normal.

The present work seems to settle the question regarding whether or not the instability of the STE is the driving force of the halogen atom desorption. We have shown that in the absence of the excited electron, the localized hole merely relaxes into the V_k center configuration on the surface and no desorption of bromine takes place (see Section 6.1.1). The instability of the STE in the third layer below the surface gives rise to the bromine atom desorption in KBr, but not in NaBr, because it belongs to a different type of materials (type III and I, respectively) and differ in the magnitude of the off-center shift and off-center relaxation energy of the STE. And also the result that the trajectory undergoes a rotation toward the normal of the (100) surface and then at a macroscopic distance the bromine atom is ejected perpendicularly has clarified some doubt.

In a recent work on defects and the STE near the surface in NaCl, Puchin *et al.* [102] have found results which are quite similar to the ones described in Section 6.1.1. They used a simplified version of the ICECAP (Ionic Crystal with Electronic Cluster: Automatic Program) code, with the norm-conserving pseudopotentials for Na^+ and Cl^{7+}. The one substantial difference is the presence of a barrier of about 0.5 eV for the STE in the third layer and below. At this depth, the STE is quite similar to that in the bulk, and the origin of the barrier should be the same as in their earlier works using the same method [89]. Based on Song and Baetzold's earlier studies [87, 88] using both ICECAP code (with and without the pseudopotentials) and CADPAC (Cambridge Analytic Derivatives Package) code , it is believed that this barrier found may be due to the use of the pseudopotentials as well as the choice of the floating Gaussian orbitals used. Indeed, with the use of the pseudopotentials the core polarization of some of the alkali ions are not adequately provided. As the ions can not relax much in the bulk, the core polarization becomes more crucial for the relaxation of the system. By contrast, an alkali ion at the surface can freely relax into the vacuum without raising the energy, as can be seen in Ref [102].

6.2 Influence of In^+ Doping in KBr

The yield of the halogen atom desorption decreases in KBr when doped with In^+. We studied the influence of In^+ doping in KBr in two cases, the free exciton on the (100) surface, and the STE in the third layer below the surface.

6.2.1 The free exciton on the surface

In the experiment, the concentration of In^+ in investigated samples varied between 10^{17} and 10^{20} particles/cm^3. It is reasonable to have only one In^+ in the cluster. There are 5 nearest cations for an anion site on (100) surface as shown in Fig. 6.7(a). The positions of the four cations on the surface are equivalent, so we calculated the APES for an In^+ replacing one of the four potassiums on the surface (Fig. 6.7(b)) or replacing the one below the surface (Fig. 6.7(c)). As in pure KBr, the excited electron localizes on the anion site thereby becoming an F center, at the same time, the bromine atom on which the hole is localized is ejected. The relaxation energy in both cases are about 3.0 eV, 0.4 eV larger than in pure KBr. It is found that an In^+ on the surface near Br^0 has a significant effect on the trajectory. The excited electron is attracted by both the anion site and In^+ and as a result the trajectory of the desorbing Br^0 deviates markedly. The APESs are shown in Fig. 6.8.

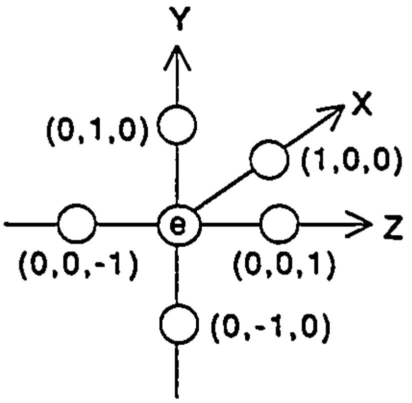

Figure 6.7: Configurations of an In$^+$ Neighbour for a Free Exciton on the Surface

6.2.2 The STE in the third layer

For the STE in the third layer, an In$^+$ replacing one of the 10 nearest potassiums should give the most influence. The STE and the 10 nearest cation sites are illustrated in Fig. 6.9 in which the 10 sites are numbered. We investigated the influence of the In$^+$ impurity in different nearest cation sites. We put the floating Gaussian bases on sites (2,-2,0) and (3,-3,0), the two Br$^-$ ions on which form the molecule, as well as the 10 nearest cation sites, one of which was replaced by an In$^+$, the number of ions which are allowed to move is about 40. The results are given in Table 6.2. It would be noticed that the hole distributions are almost the same for an In$^+$ to be in site 1 or in site 2, these 2 positions are equivalent. Other pairs like sites 3 and 4, 5 and 6, and so on, should also be equal, so we calculated only one position for a pair.

It is found that the In$^+$ attracts the hole, makes the excited electron tend to localize nearer to the In$^+$. From Table 6.2, we can see that when an In$^+$ is in site 1 or site 2, there are more hole on ion (2,-2,0) which is closer to the surface, and

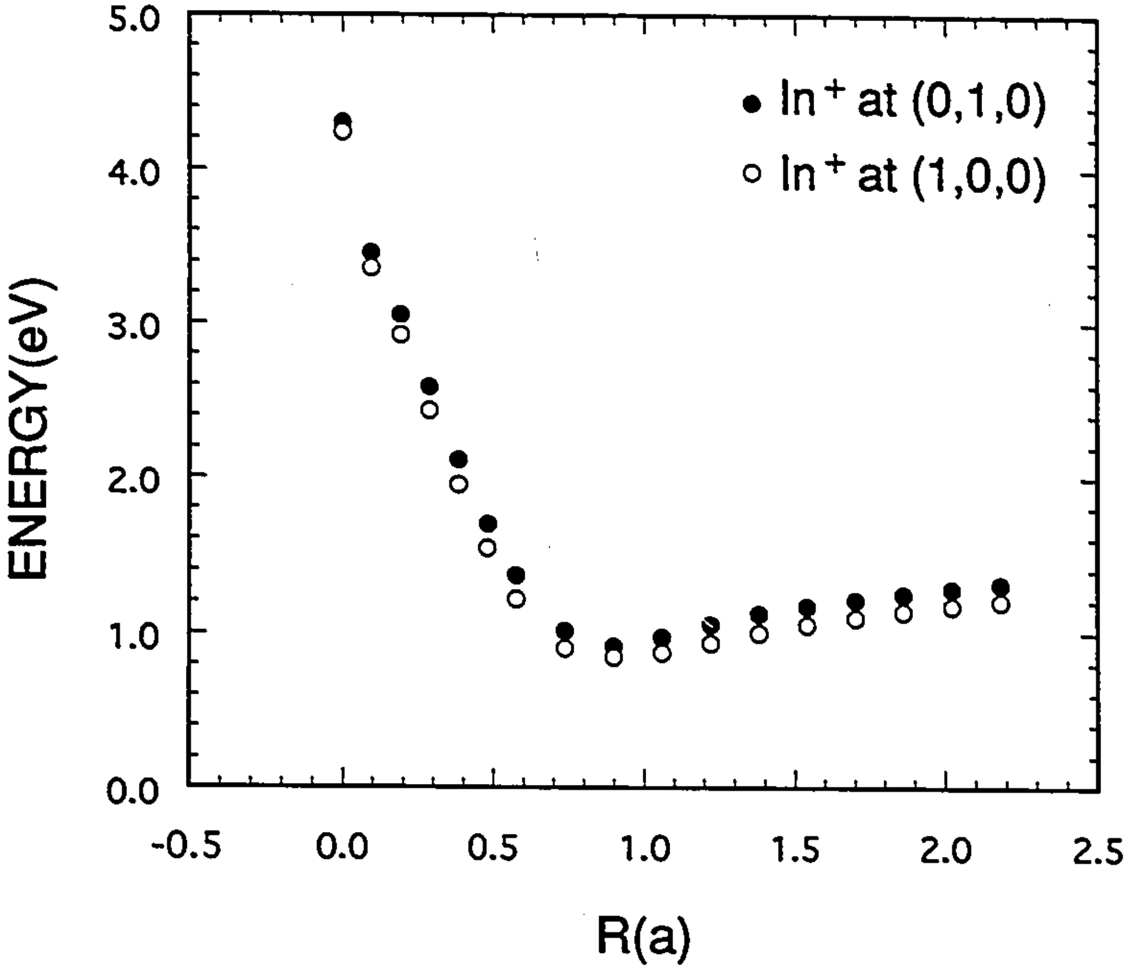

Figure 6.8: The APES of Free Exciton in KBr:In

The APES of the free exciton decay on the surface in KBr:In. Energy is in eV and the coordinate R (in units of the anion-cation distance) gives the distance between the (100) surface and the bromine atom.

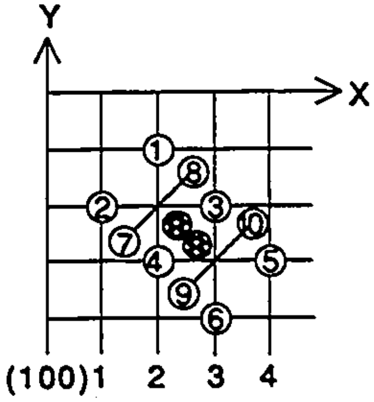

The sites of molecule-ion:
(2,-2,0) & (3,-3,0)

Possible positions of the In^+
adjacent to the third layer's STE:

1 (2,-1,0) ; 2 (1,-2,0) ;
3 (3,-2.0) ; 4 (2,-3,0) ;
5 (4,-3,0) ; 6 (3,-4,0) ;
7 (2,-2,1) ; 8 (2,-2,-1) ;
9 (3,-3,1) ; 10 (3,-3,-1)

Figure 6.9: The Illustration of the Possible Positions of the In^+ Adjacent to the Third Layer's STE

Table 6.2: Polarization of V_k Center Influenced by In^+ Impurity

In^+ Position	Hole Distribution (3,-3,0)	(2,-2,0)	Excite Electron Localizes on
1 (2,-1,0)	0.29	0.71	(2,-2,0)
2 (1,-2,0)	0.28	0.72	(2,-2,0)
3 (3,-2,0)	0.49	0.51	(1,-2,0)
5 (4,-3,0)	0.72	0.28	(3,-3,0)
7 (2,-2,1)	0.24	0.76	(2,-2,0)
9 (3,-3,1)	0.75	0.25	(3,-3,0)

The In^+ positions are referred to Fig. 6.9. (2,-2,0) and (3,-3,0) are the sites of ions which form the molecule. (2,-2,0) is closer to the surface. The results for sites 1 and 2 are almost the same, these two positions are equivalent. And so it is for sites 3 and 4, 5 and 6, and so on, one position is calculated for a pair as shown in the table. When an In^+ is in the No.3 (No.4) site, the excited electron localizes on a K^+ site. It makes the hole jump back and forth, and the energy minimization could not reach convergence.

the excited electron localizes on the site of ion (2,-2,0) with an In^+ adjacent to it. In these two cases, the In^+ makes the excited electron localize closer to the surface, then the off-center relaxation of the STE will propel Br_2^- toward the interior. There will be no desorption in these cases. It is expected either to recombine giving off the π band, or create F-H pair like in the cases described above for the first and second layers. The results are almost the same when an In^+ is in site 7 or 8. The APES of the STE in the third layer in KBr with an In^+ adjacent to it at site 1 is shown in Fig.6.10.

When an In^+ adjacent to a third layer STE, on the site (5 and 6, 9 and 10) further to the surface, the excited electron will localize on the Br site deeper in the bulk, the APES in this case is similar to the one in pure KBr. An In^+ in the site 3 or 4 makes excited electron localize on a K^+ site, which causes the hole jumping back and forth. No stable STE structure was obtained in this case. In conclusion, being near the STE, an In^+ impurity tends to inhibit Br^0 desoption by attracting the excited electron and propelling the V_k center away from the surface.

6.3 Desorption from (111) Surface of CaF_2

There is no comparable experimental work on F^0 desorption with hyperthermal emission in CaF_2. However, there are some interesting results obtained from our theoretical calculation [111].

Here we present preliminary works dealing with the desorption of fluorine atom induced by decay of excitons (either Frenkel-type free exciton or the STE) on and below the (111) surface. Several different initial excitations localized on the (111) surface and on the next F^- plane are studied. Our primary interest is still in the instability aspect of the STE near the surface.

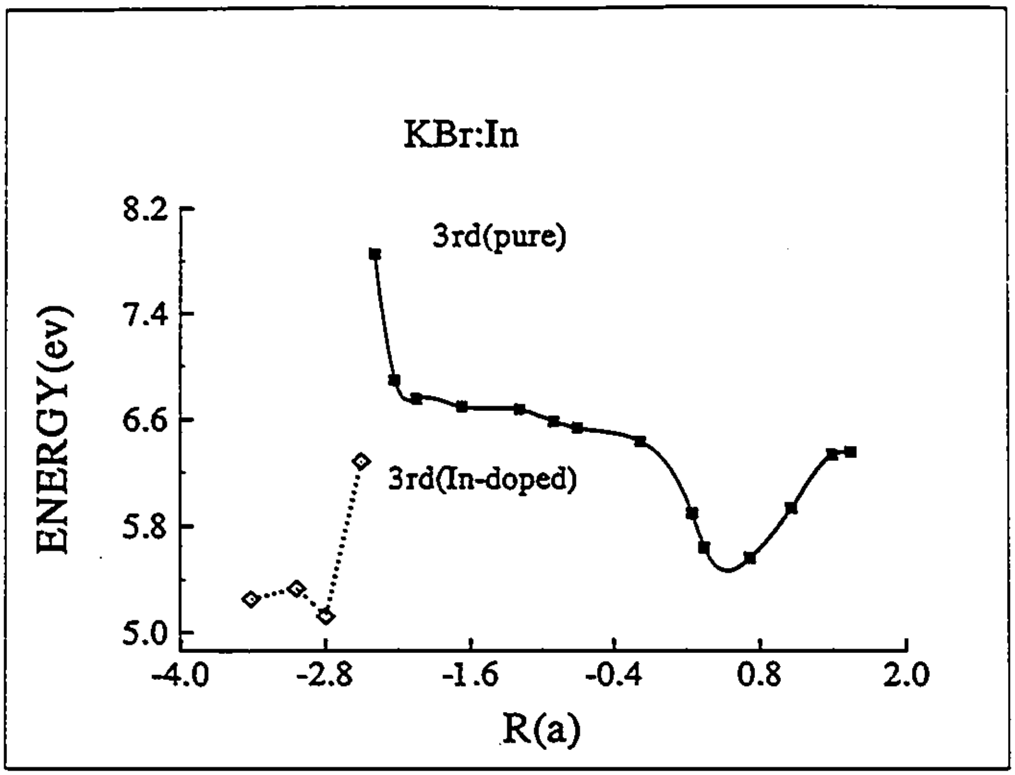

Figure 6.10: The APES of the STE in KBr:In

The APES of the STE created at the third layer below the surface in KBr:In. Energy is in eV and the coordinate R (in units of the anion-cation distance) gives the distance between the (100) surface and the center of gravity of the hole charge distributed on the bromine atoms. The APES of pure KBr is also shown for comparing.

The crystal of CaF_2 with a surface (111) is represented by a semi-spherical cluster of atoms arranged as in the perfect crystal at 0 K. The size of the cluster which is electrically neutral is about 1100-1500. Typically, a pair of floating Gaussian bases (with $\alpha = 0.03$ and 0.06 in atomic units: $\exp(-\alpha r^2)$) is used to represent an excited electron. Because of the lattice structure in the fluorite, the <111> planes contain only one type of ions (see Fig. 6.11), such that starting from the surface the successive planes are $F^-/Ca^{2+}/F^-$/empty/F^-/Ca^{2+}, etc. It is assumed that the samples studied experimentally are cleaved along the plane marked *empty* above.

6.3.1 Decay of free exciton

The free Frenkel-exciton is simulated by an excited electron bound to a fluorine atom F^0 in an otherwise perfect lattice. Such a system on the (111) surface was studied. The system is found to be highly unstable and the fluorine atom desorbs normal to the surface with a portion of the relaxation energy which is estimated to be about 2.0 eV. As the direction of the fluorine emission is perpendicular to the surface throughout the relaxation cycle in the calculation, it seems that a good fraction may be converted to kinetic energy.

6.3.2 Decay of the STE on the (111) surface

In this case the distance between the pair of fluorines is 3.85 Å in the perfect lattice. The excited electron very quickly localizes on one of the anion site in the early stage of lattice relaxation cycle. The fluorine closest to the nascent F center is displaced by a large amount out of the plane while the other F regains the regular anion site. The potential energy shows a total drop of about 3.0 eV, but only a portion of this may be available to impart a kinetic energy along the ejecting direction. Before

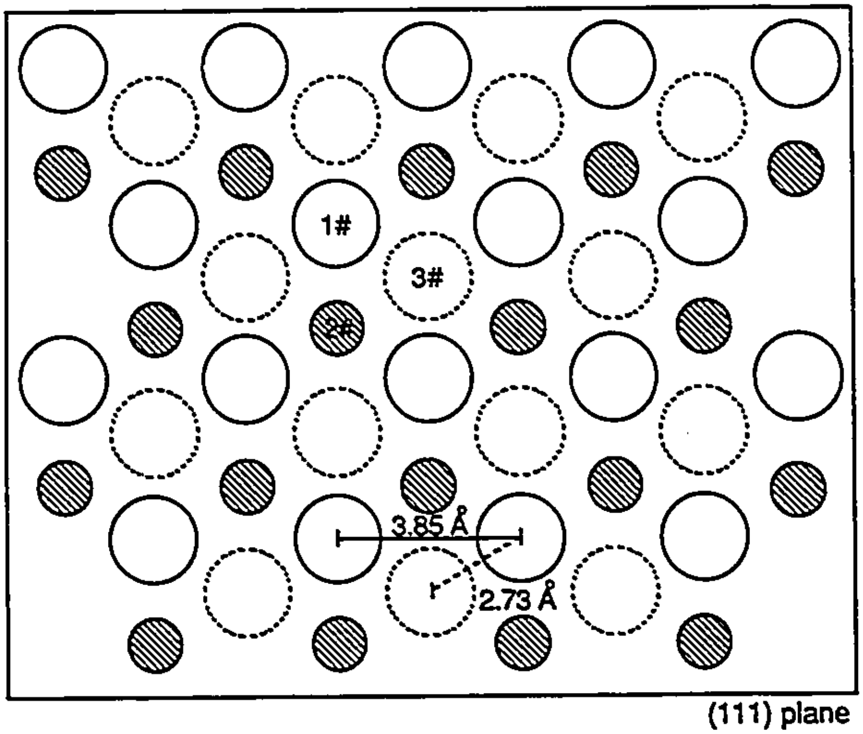

Figure 6.11: The Structure of (111) Surface and Planes Below in CaF_2

The arrangement of atoms are shown viewed vertically from above the (111) surface.
1# F^- layer on the (111) surface,
2# Ca^{2+} layer, the first plane below the surface,
3# F^- layer, the second plane below the surface.
The next plane is an empty plane.
In the perfect lattice, the distance between a pair of fluorines on the surface is 3.85 Å, and the distance between a fluorine on the surface and a fluorine on the first plane is 2.73 Å.

the molecular bond is broken, the energy goes through a barrier of about 1 eV at about 3 Å from the surface. Similar feature was also observed in the studies in NaCl lattice as described above. The barrier is related to the dissociation of the molecule ion, which depends somewhat on the choice of the CNDO parameters. As long as the energy drop is larger than the potential barrier height there could be an energetic fluorine emission. The direction of ejection determined at about 1 Å from the surface is estimated to be around 60° from the vertical to the surface. Energy minimization away from the surface by more than several Å is imprecise, however. As will be discussed below, there is generally a correction of trajectory once the ejected atom has cleared the surface.

6.3.3 Decay of the STE between the surface and the next fluorine plane

The distance between this pair of fluorines in the perfect lattice is shorter (2.73 Å) than in the case above (3.85 Å). It is expected that all else being equal the molecule-ion F_2^- may be formed more easily here. As in the NaCl lattice, we allowed the excited electron to be free to choose the site (on the surface or on the next fluorine plane) to localize by providing floating Gaussian bases on both planes. Invariable, the electron localized on the surface thereby creating an F center on the surface. The surface has the same influence as for the first two layers in KBr. However, the structure of (111) planes in CaF_2 is different from the structure of (100) planes in KBr. The excited electron would not propel the molecule toward the next plane, the Ca^{2+} plane, instead it made the axis of molecule rotate because of the symmetry, (see Fig. 6.12). During the time when the axis of the molecule approached parallel to the normal of the (111) surface, the fluorine displaced by the electron desorbed. This fluorine followed a trajectory which gradually became perpendicular to the surface.

When the total energy was minimized relative to all relaxing atoms, including the desorbing atom, the angle was about 30° from the normal at a distance of about 1 Å from the surface. At this point, the desorbing atom was given an imposed trajectory perpendicular to the surface and the potential energy was obtained by relaxing all other ions (about two dozens). The potential energy plotted relative to the perpendicular distance of the F^0 from the surface is presented in Fig. 6.13. There is an energy barrier of about 0.6 eV on the way to molecule dissociation, similar to the case presented in 2. The relaxation energy available that can be converted to the kinetic energy is larger than the barrier height and therefore an energetic fluorine desorption is possible.

It is quite clear that the exciton, both free and self-trapped, is unstable at or near the surface and as a result fluorine atom can desorb leaving behind an F center on the surface. The parameters which are of interest are the direction of ejection from the surface and the kinetic energy imparted to the emission atom. Except in the case of the free exciton, when the trajectory is normal to the (111) surface from the beginning, the fluorine atom takes a trajectory which undergoes deviation as it leaves the surface to become normal to the (111) surface at large distance. This correction of trajectory seems reasonable when the symmetry of the charges on the surface is considered.

When the exciton decay occurs near the surface, there is adequate relaxation energy which can be converted into ejecting an F atom. The present work shows that this is the case on the surface and the next fluorine plane. It seems unlikely that fluorine atom will desorb from planes deeper than the first two if we refer to the STE relaxation in the bulk.

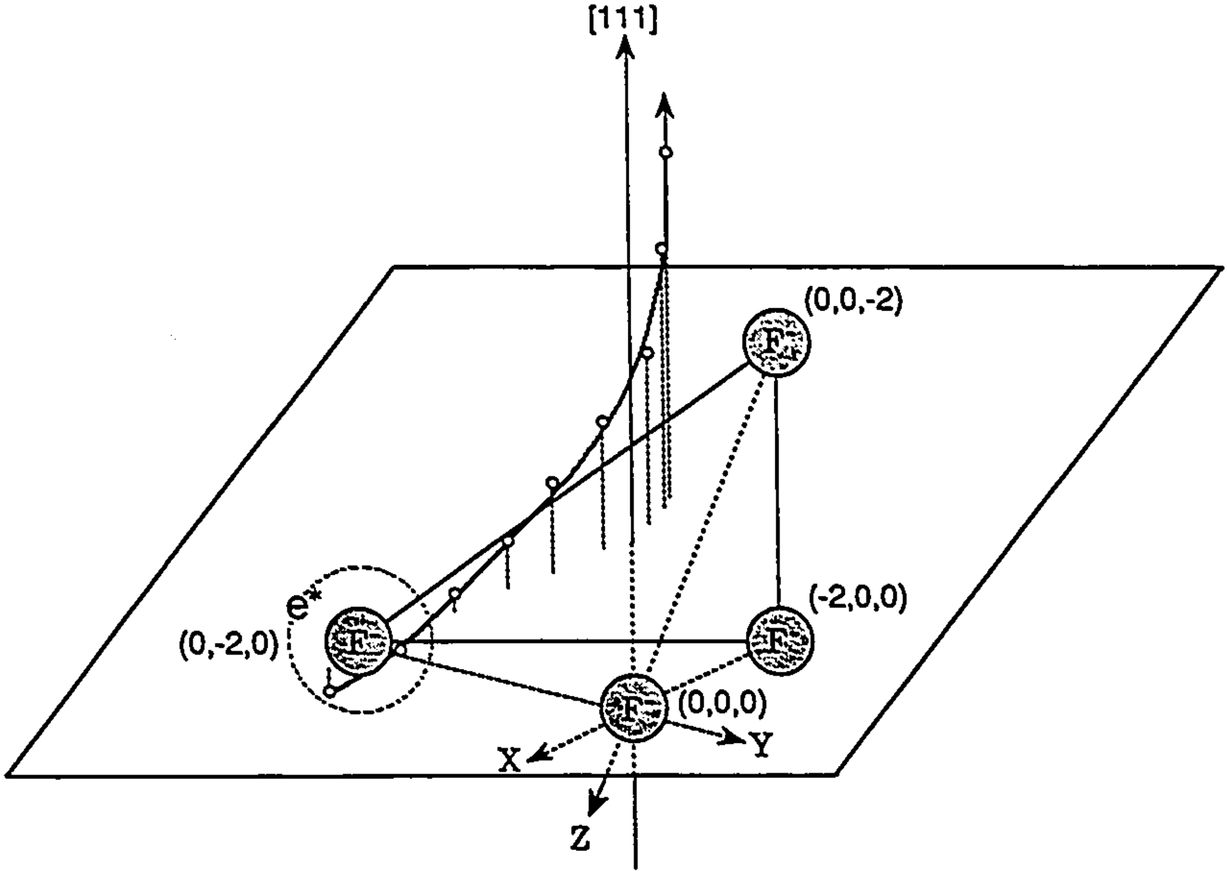

Figure 6.12: The Trajectory of the Desorbing F Atom in CaF_2

Fluorines (0,-2,0), (0,0,-2) and (-2,0,0) are on the (111) surface, fluorine (0,0,0) is on the plane below the surface. (0,-2,0) and (0,0,0) form the molecule. The excited electron localizes on (0,-2,0) and propels the fluorine following the trajectory indicated by the circles. The axis of the molecule approaches parallel to the normal of the surface, and the trajectory of the desorbing F atom becomes perpendicular to the normal gradually.

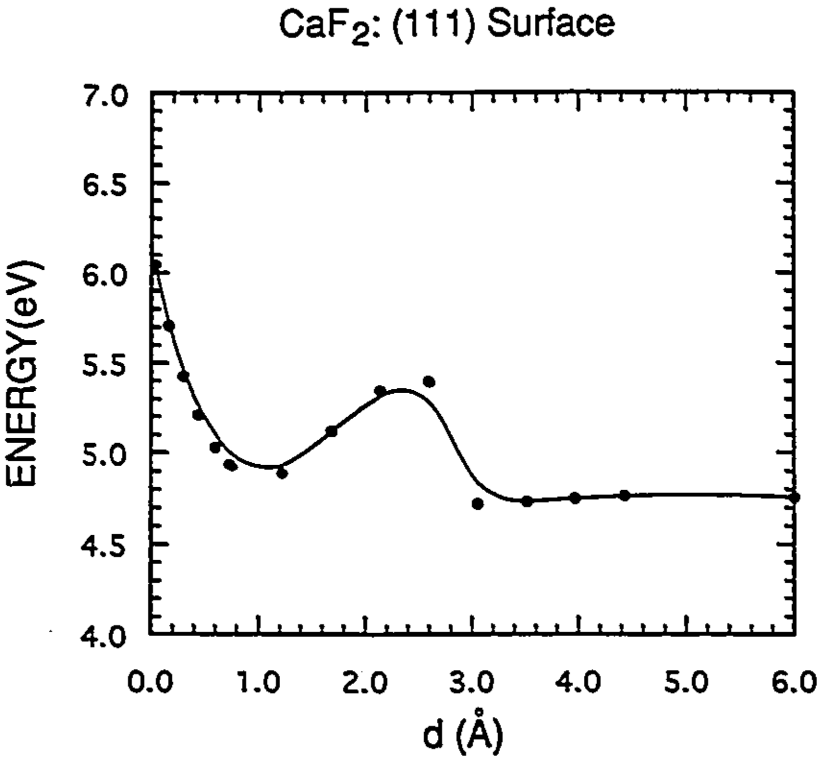

Figure 6.13: The APES of the Desorbing F Atom in CaF_2

The APES of the desorbing F atom as a function of the distance from the (111) surface d in CaF_2 ($d = 0$ indicates the surface). The STE is created between a pair of fluorines on and below the surface. Energy is in eV.

6.3.4 Study of an ideal (111) Ca^{2+} surface

Our preliminary work on an ideal (111) Ca^{2+} surface indicates that there is a large atomic relaxation. Ca^{2+} ions move inward, perpendicular to the surface, by as much as 0.5 Å, with the facing F^- ions moving outward by comparable magnitude. This seems to imply an instability in this surface. On the other hand, as the (111) F^- surface studied above undergoes a gradual depletion of F^0 atoms leading to a formation of F center clusters on the surface, interesting processes could take place, such as the transfer of the excited electrons to Ca^{2+}, transforming it to Ca^+.

Chapter 7. Conclusion

In this chapter we summarize the main points of our desorption work.

(1) The STE shows a general instability on the surface and in the first three layers in both bromides and CaF_2 studied, in the sense that the stable state of the exciton is the one in which the hole and the excited electron become localized away from one another in space.

(2) There are two kinds of decays on the surface, the free exciton (one-center, Frenkel type) and the STE (two-center). According to our calculation, the free exciton decay makes a halogen atom ejected perpendicularly to the surface. But it is uncertain if free exciton has long enough lifetime on the surface. A Br^0 alone without the excited electron, quickly forms a stable Br_2^- on the surface and never leaves the surface. For a STE formed on (100) surface in KBr and NaBr, and on (111) surface in CaF_2, Br/F atom desorbs normal to the (100)/(111) surface in KBr/CaF_2. No such desorption is found in NaBr, because the excited electron and the hole do not split as in the bulk, there would be a radiative recombination on the surface.

(3) When the STE is created near the surface, i.e. between the surface and the first layer below the surface (in KBr, NaBr and CaF_2), and between the first and second layers (in KBr and NaBr), the symmetry of the V_k center about the midpoint of the molecule-ion is broken and the hole is attracted toward the surface. The excited electron prefers to localize nearer to the surface. So that in NaCl lattice, the off-center relaxation of the STE pushes the molecule deeper into the bulk. As a result, there is no desorption, but STE luminescence is expected from the surface. However,

the structure of (111) layers in CaF_2 is different from that of (100) layers in the bromides. In CaF_2, each (111) layer is made of one type of ions. The surface layer and the first layer are made of F^-'s, the next two layers are Ca^{2+} layer and empty, respectively. For the STE created between the surface and the first layer, the excited electron localizing on the surface propels the molecule to change the direction of its axis, since it can not go any deeper. The axis of the molecule gradually approach the normal of the surface which leads to F atoms desorption.

(4) Starting from the third layer, according to our work, the excited electron has equal probability to localize behind the Br_2^- molecule and thus propel it toward the surface. The third layer STE in KBr leads to desorption with a kinetic energy of about 1 eV. In NaBr, there is a barrier for the off-center relaxation of the STE as in the bulk. No energetic emission of Br^0 from NaBr is predicted as a result, which is in agreement with experiment [67].

(5) The presence of a In^+ adjacent to a STE in the third layer, on the side closer to the surface, results in a drastic changes. The excited electron localizes on the Br site nearer to the surface and on In^+, propelling the V_k center deeper into the bulk. So that no halogen atom desorption is expected. This may explain the observed inhibition of Br^0 desorption in In doped KBr [113].

(6) Before the molecular bond is broken, the energy goes through a barrier of about 1 eV near the surface for both Br and F atoms desorption, which is related to the dissociation of the molecule ion. It depends somewhat on the choice of the CNDO parameters. As long as the energy drop is larger than the potential barrier height there could be an energetic emission. How much of the relaxation energy is imparted to the ejecting fluorine atom is more complex. Generally, a few eV of relaxation energy is available when the STE undergoes non-radiative decay. In terms

of a recent work by Meise *et al.* [105], it seems, at least in the case of energetic halogen desorption in NaCl lattice, that up to the fourth layer below the surface contribute to the emission. Halogen atoms from different layers would leave the surface with different velocities on the average. The spread of kinetic energy of emitted halogen atoms in KBr [67, 114] does not seem incompatible with this interpretation.

(7) The perpendicular halogen atom emission from the (100) surface in NaCl is observed by Szymonski *et al.* [67, 114] and confirmed by calculations [115, 77, 102]. This is one of the important findings which any mechanism must be able to explain. As our calculations shows in Chapter 6, in the cases of the free exciton (one-center, Fenkel type) and the STE on the surface, the trajectory of halogen atoms is normal to the surface from the beginning, this is true for all the three crystals with different surfaces ((100) in NaCl lattice, (111) in CaF_2). When the STE is formed below the surface, in NaCl lattice the halogen atom is given an initial momentum along the [110] axis and on approaching the surface undergoes a deviation toward the normal to the (100) plane. In CaF_2 crystal, the fluorine atom's trajectory also undergoes deviation as it leaves the surface to become normal to the (111) surface at large distance. The trajectory correction seems to be determined by the symmetry of the long and short range interactions with the atoms on and below the surface.

(8) In conclusion, we have shown evidence that the STE instability is likely the driving force of the energetic halogen atom desorption from near the surface. Hot hole transport from inside toward the surface, proposed by Szymonski *et al.* [112] may have some indirect influence on the desorption of Br^0. However, we do not think anion atom desorption can be realized without the excited electron localization near the surface.

Appendix A. Properties of Gaussians

We first list some properties of Gaussian basis functions. An excellent description of this subject may be found in reference [116].

In this work, we use exclusively floating Gaussians of spherical symmetry defined as

$$G_i(\vec{r}_i) = e^{-\alpha_i \vec{r}_i^{\,2}} \ , \quad (\alpha > 0) \tag{A.1}$$

where the Gaussian is centered at $\vec{R}_i$ and $\vec{r}_i = \vec{r} - \vec{R}_i$.

The product of two Gaussians centered at any two sites, is itself a Gaussian centered at a third site

$$G_i(\vec{r}_i) G_j(\vec{r}_j) = K G_k(\vec{r}_k) \ , \tag{A.2}$$

where

$$K = e^{-\frac{\alpha_i \alpha_j}{\alpha_i + \alpha_j} |\vec{R}_i - \vec{R}_j|^2} \ , \tag{A.3}$$

$$\alpha_k = \alpha_i + \alpha_j \ , \tag{A.4}$$

$$and \quad \vec{R}_k = \frac{\alpha_i \vec{R}_i + \alpha_j \vec{R}_j}{\alpha_i + \alpha_j} \ . \tag{A.5}$$

In terms of the properties of Gaussians the calculation of the kinetic energy and the point-ion energy is straightforward. The expression of the kinetic energy is

$$\langle \phi_i | T | \phi_j \rangle = \int e^{-\alpha_i \vec{r}_i^{\,2}} \left(-\frac{1}{2} \nabla^2 \right) e^{-\alpha_j \vec{r}_j^{\,2}} d\tau$$

$$= \frac{\alpha_i \alpha_j}{\alpha_i + \alpha_j} \left(3 - 2 \frac{\alpha_i \alpha_j}{\alpha_i + \alpha_j} |\vec{R}_i - \vec{R}_j|^2 \right) \left(\frac{\pi}{\alpha_i + \alpha_j} \right)^{\frac{3}{2}} e^{-\frac{\alpha_i \alpha_j}{\alpha_i + \alpha_j} |\vec{R}_i - \vec{R}_j|^2} \ . \tag{A.6}$$

And the expression of the point-ion energy is

$$\langle\phi_i|\frac{Z_\gamma}{|\vec{r}-\vec{R}_\gamma|}|\phi_j\rangle = \sum_\gamma \int e^{-\alpha_i \vec{r}_i\ ^2} \frac{Z_\gamma}{|\vec{r}-\vec{R}_\gamma|} e^{-\alpha_j \vec{r}_j\ ^2} d\tau$$

$$= \sum_\gamma Z_\gamma \frac{2\pi}{\alpha_i+\alpha_j} F_0\left[(\alpha_i+\alpha_j)|\vec{R}_\kappa-\vec{R}_\gamma|^2\right] e^{-\frac{\alpha_i\alpha_j}{\alpha_i+\alpha_j}|\vec{R}_i-\vec{R}_j|^2}\ , \qquad \text{(A.7)}$$

where Z_γ is the net charge on ion γ, $\vec{R}_k$ is defined as in equation A.5 and

$$F_0(t) = \frac{1}{2}\sqrt{\frac{\pi}{t}}erf(\sqrt{t})\ . \qquad \text{(A.8)}$$

erf is the error function [117] For ions in their perfect lattice positions the sum of equation A.8 is evaluated by the Ewald method [118]. For ions that have been displaced from their perfect lattice positions the point-ion potential is evaluated using equation A.8 (without the sum over γ).

Appendix B. Deep Core Ion Size Parameters

We used Bartram's [28] approach to calculate the contributions from deep core orbitals of the ions in the lattice. Bartram's pseudopotential is based on the assumption that the smooth pseudo-wavefunction varies slowly over the region occupied by an atomic core, which we have imposed on our Gaussian ϕ_i.

Assuming that ϕ_i is slowly varying, we can expand it in a multipolar series

$$\begin{aligned} \phi_i(\vec{r}-\vec{R}_i) &= 2\pi \sum_l \bar{F}_l(\vec{r},\vec{R}_i) P_l(\cos\Omega) \\ &= 2\pi \sum_l \bar{F}_l(\vec{r},\vec{R}_i) \sum_m \frac{4\pi}{2l+1} Y_{lm}(\hat{r}) Y^{*}_{lm}(\hat{R}_i) \ , \end{aligned} \tag{B.1}$$

where $\Omega = \angle(\widehat{\vec{r},\vec{R}_i})$, $\phi_i(\vec{r}-\vec{R}_i) = e^{-\alpha|\vec{r}-\vec{R}_i|^2}$.

Multiply $P_{l'}(\cos\Omega)$ for both sides and integrate:

$$\int_{-1}^{1} P_{l'}(\cos\Omega)\phi_i(\vec{r}-\vec{R}_i)d(\cos\Omega) = 2\pi\sum_l \bar{F}_l(\vec{r},\vec{R}_i)\frac{2}{2l+1}\delta_{ll'} \ , \tag{B.2}$$

we obtain

$$\bar{F}_l(\vec{r},\vec{R}_i) = \frac{2l+1}{4\pi}\int_{-1}^{1}\phi(\vec{r}-\vec{R}_i)P_l(\cos\Omega)d(\cos\Omega) \ . \tag{B.3}$$

Then we rewrite

$$\phi_i(\vec{r}-\vec{R}_i) = 2\pi\sum_l F_l(\vec{r},\vec{R}_i)Y_{lm}(\hat{r})Y^{*}_{lm}(\hat{R}_i) \ , \tag{B.4}$$

$$F_l(\vec{r},\vec{R}_i) = \int_{-1}^{1}\phi(\vec{r}-\vec{R}_i)P_l(\cos\Omega)d(\cos\Omega) \ . \tag{B.5}$$

Further we expand $F_l(\vec{r},\vec{R}_i)$ in a Taylor's series about $\vec{R}_i$

$$\phi_i(\vec{r}-\vec{R}_i) = 2\pi\sum_l \left[\sum_n \frac{1}{n!}F_l^{(n)}(0,\vec{R}_i)r^n\right]\sum_m Y_{lm}(\hat{r})Y^{*}_{lm}(\hat{R}_i) \ , \tag{B.6}$$

$$F_l^{(n)}(0,\vec{R}_i) = \int_{-1}^{1}\left[\frac{\partial^n}{\partial r^n}e^{-\alpha(\vec{r}-\vec{R}_i)^2}\right]_{\vec{r}=0} P_l(\cos\Omega)d(\cos\Omega)\ . \tag{B.7}$$

Up to the order of r^2 we have:

$$\begin{aligned}
F_0^{(0)} &= 2e^{-\alpha R_i^2}\ ,\\
F_0^{(1)} &= 0\ ,\\
F_0^{(2)} &= e^{-\alpha R_i^2}\left(\frac{8}{3}\alpha^2 R_i^2 - 4\alpha\right)\ ,\\
F_1^{(0)} &= 0\ ,\\
F_1^{(1)} &= \frac{4}{3}\alpha R_i e^{-\alpha R_i^2}\ ,\\
F_1^{(2)} &= 0\ .
\end{aligned} \tag{B.8}$$

After the expansion the overlap integral can be expressed in a convenient form

$$\begin{aligned}
\langle\phi_i|\chi_{\gamma,\lambda}\rangle &= 2\pi\int\Big[\Big[F_{0i}^{(0)} + \frac{1}{2}F_{0i}^{(2)}r^2\Big]Y_{00}^*(\hat{r})Y_{00}(\hat{R}_i)\\
&\quad + F_{1i}^{(1)}r\left[Y_{10}^*(\hat{r})Y_{10}(\hat{R}_i) + Y_{11}^*(\hat{r})Y_{11}(\hat{R}_i)\right.\\
&\quad \left. + Y_{1\bar{1}}^*(\hat{r})Y_{1\bar{1}}(\hat{R}_i)\right]\Big]\chi_{\gamma,\lambda}d\tau\\
&= 2\pi\left[F_{0i}^{(0)}\frac{1}{4\pi}\int\chi_{\gamma,\lambda}d\tau + \frac{1}{2}F_{0i}^{(2)}\frac{1}{4\pi}\int r^2\chi_{\gamma,\lambda}d\tau\right.\\
&\quad + F_{1i}^{(1)}\sqrt{\frac{3}{4\pi}}Y_{10}(\hat{R}_i)\int r\cos\theta\chi_{\gamma,\lambda}d\tau
\end{aligned}$$

$$+ F_{1i}^{(1)}\sqrt{\frac{3}{8\pi}}Y_{11}(\hat{R}_i)\int r\sin\theta e^{-i\varphi}\chi_{\gamma,\lambda}d\tau$$

$$+ F_{1i}^{(1)}\sqrt{\frac{3}{8\pi}}Y_{1\bar{1}}(\hat{R}_i)\int r\sin\theta e^{i\varphi}\chi_{\gamma,\lambda}d\tau\Bigg] \ . \qquad \text{(B.9)}$$

Therefore

$$\begin{aligned}
&\sum_{\lambda}\langle\phi_i|\chi_{\gamma,\lambda}\rangle\langle\chi_{\gamma,\lambda}|\phi_j\rangle \\
= &\sum_{\lambda}\Bigg[\frac{1}{4}F_{0i}^{(0)}F_{0j}^{(0)}\left(\int\chi_{\gamma,\lambda}d\tau\right)^2 \\
&+ \frac{1}{8}\left(F_{0i}^{(0)}F_{0j}^{(2)} + F_{0i}^{(2)}F_{0j}^{(0)}\right)\int\chi_{\gamma,\lambda}d\tau\int r^2\chi_{\gamma,\lambda}d\tau \\
&+ 3\pi F_{1i}^{(1)}F_{1j}^{(1)}\Bigg[Y_{10}(\hat{R}_i)Y_{10}^*(\hat{R}_j)\left(\int r\cos\theta\chi_{\gamma,\lambda}d\tau\right)^2 \\
&+\frac{1}{2}Y_{11}(\hat{R}_i)Y_{11}^*(\hat{R}_j)\left(\int r\sin\theta e^{i\varphi}\chi_{\gamma,\lambda}d\tau\right)^2 \\
&+ \frac{1}{2}Y_{1\bar{1}}(\hat{R}_i)Y_{1\bar{1}}^*(\hat{R}_j)\left(\int r\sin\theta e^{-i\varphi}\chi_{\gamma,\lambda}d\tau\right)^2\Bigg]\Bigg] \\
= &\sum_{\lambda}\Bigg[\frac{1}{4}F_{0i}^{(0)}F_{0j}^{(0)}\left(\int\chi_{\gamma,\lambda}d\tau\right)^2 \\
&+ \frac{1}{8}\left(F_{0i}^{(0)}F_{0j}^{(2)} + F_{0i}^{(2)}F_{0j}^{(0)}\right)\int\chi_{\gamma,\lambda}d\tau\int r^2\chi_{\gamma,\lambda}d\tau \\
&+ \frac{9}{4}F_{1i}^{(1)}F_{1j}^{(1)}\Bigg[\cos\theta_i\cos\theta_j\left(\int r\cos\theta\chi_{\gamma,\lambda}d\tau\right)^2
\end{aligned}$$

$$
\begin{aligned}
&+\frac{1}{4}\sin\theta_i\sin\theta_j e^{i(\varphi_i-\varphi_j)}\left(\int r\sin\theta e^{i\varphi}\chi_{\gamma,\lambda}d\tau\right)^2 \\
&+\frac{1}{4}\sin\theta_i\sin\theta_j e^{-i(\varphi_i-\varphi_j)}\left(\int r\sin\theta e^{-i\varphi}\chi_{\gamma,\lambda}d\tau\right)^2\Bigg]\Bigg] \\
= &\sum_\lambda\Bigg[\frac{1}{4}F_{0i}^{(0)}F_{0j}^{(0)}\left(\int\chi_{\gamma,\lambda}d\tau\right)^2 \\
&+\frac{1}{8}\left(F_{0i}^{(0)}F_{0j}^{(2)}+F_{0i}^{(2)}F_{0j}^{(0)}\right)\int\chi_{\gamma,\lambda}d\tau\int r^2\chi_{\gamma,\lambda}d\tau \\
&+\frac{9}{4}F_{1i}^{(1)}F_{1j}^{(1)}\frac{\vec{R}_i\cdot\vec{R}_j}{|\vec{R}_i||\vec{R}_j|}\left(\int r\cos\theta\chi_{\gamma,\lambda}d\tau\right)^2\Bigg]\ , \qquad \text{(B.10)}
\end{aligned}
$$

where the term of $F_{0i}^{(2)}F_{0j}^{(2)}$ is dropped because it becomes a term of order r^4. Also the terms like

$$F_{0i}^{(0)}F_{1j}^{(1)}\frac{1}{4\pi}\sqrt{\frac{3}{4\pi}}Y_{10}(\hat{R}_j)\int\chi_{\gamma,\lambda}d\tau\int r\cos\theta\chi_{\gamma,\lambda}^*d\tau$$

are zero. Since $\chi_{\gamma,\lambda}$ can not be non-zero in both $\int\chi_{\gamma,\lambda}d\tau$ and $\int r\cos\theta\chi_{\gamma,\lambda}^*d\tau$ at the same time, either of the integrals will be zero.

In the last step of equation (B.11) we have used

$$
\begin{aligned}
\sum_\lambda\left(\int r\sin\theta e^{i\varphi}\chi_{\gamma,\lambda}d\tau\right)^2 &= \sum_n\left(\int r\sin\theta e^{i\varphi}\chi_{\gamma,n,11}d\tau\right)^2 \\
&= 2\sum_n\left(\int r\cos\theta\chi_{\gamma,n,10}d\tau\right)^2\ , \qquad \text{(B.11)} \\
\sum_\lambda\left(\int r\sin\theta e^{-i\varphi}\chi_{\gamma,\lambda}d\tau\right)^2 &= \sum_n\left(\int r\sin\theta e^{-i\varphi}\chi_{\gamma,n,1\bar{1}}d\tau\right)^2 \\
&= 2\sum_n(\int r\cos\theta\chi_{\gamma,n,10}d\tau)^2, \qquad \text{(B.12)}
\end{aligned}
$$

here n is the principle quantum number. And

$$\cos\theta_i \cos\theta_j + \sin\theta_i \sin\theta_j \cos(\varphi_i - \varphi_j) = \cos(\widehat{\vec{R}_i, \vec{R}_j}) \ . \tag{B.13}$$

We obtain the ion-size parameters B_γ, K'_γ and K_γ:

$$\sum_\lambda \langle \phi_i | \chi_{\gamma,\lambda} \rangle \langle \chi_{\gamma,\lambda} | \phi_j \rangle = f_1 B_\gamma + f_2 K'_\gamma + f_3 K_\gamma \ , \tag{B.14}$$

where

$$f_1 = \frac{1}{4} F^0_{0i}(0, \vec{R}_i) F^0_{0j}(0, \vec{R}_j) \ , \tag{B.15}$$

$$f_2 = \frac{1}{8} \left(F^0_{0i}(0, \vec{R}_i) F^2_{0j}(0, \vec{R}_j) + F^2_{0i}(0, \vec{R}_i) F^0_{0j}(0, \vec{R}_j) \right) \ , \tag{B.16}$$

$$f_3 = \frac{9}{4} F^1_{1i}(0, \vec{R}_i) F^1_{1j}(0, \vec{R}_j) \frac{\vec{R}_i \cdot \vec{R}_j}{|\vec{R}_i||\vec{R}_j|} \ , \tag{B.17}$$

$$B_\gamma = \sum_\lambda B_{\gamma,\lambda} = \sum_\lambda \left(\int \chi_{\gamma,\lambda} d\tau \right)^2 \ , \tag{B.18}$$

$$K'_\gamma = \sum_\lambda K'_{\gamma,\lambda} = \sum_\lambda (\int \chi_{\gamma,\lambda} d\tau) \left(\int \chi_{\gamma,\lambda} r^2 d\tau \right) \ , \tag{B.19}$$

$$K_\gamma = \sum_\lambda K_{\gamma,\lambda} = \sum_\lambda \left(\int \chi_{\gamma,\lambda} r \cos\theta d\tau \right)^2 \ . \tag{B.20}$$

Similarly, for the screened Coulomb and the exchange terms we have

$$\langle \phi_i | (V_{sc}(\vec{r}) + V_{ex}(\vec{r}))_\gamma | \phi_j \rangle$$

$$
\begin{aligned}
= \; & \frac{1}{4} F_{0i}^{(0)} F_{0j}^{(0)} \int \left(V_{sc}(\vec{r}) + V_{ex}(\vec{r})\right)_\gamma d\tau \\
& + \frac{1}{8} \left(F_{0i}^{(0)} F_{0j}^{(2)} + F_{0i}^{(2)} F_{0j}^{(0)} \right) \int \left(V_{sc}(\vec{r}) + V_{ex}(\vec{r})\right)_\gamma r^2 d\tau \\
& + \frac{9}{4} F_{1i}^{(1)} F_{1j}^{(1)} \Big[\cos\theta_i \cos\theta_j \int r \cos\theta \left(V_{sc}(\vec{r}) + V_{ex}(\vec{r})\right)_\gamma r' \cos\theta' \, d\tau \\
& + \frac{1}{4} \sin\theta_i \sin\theta_j \; e^{i(\varphi_i - \varphi_j)} \int r \sin\theta e^{i\varphi} \left(V_{sc}(\vec{r}) + V_{ex}(\vec{r})\right)_\gamma r' \sin\theta' e^{-i\varphi'} d\tau \\
& + \frac{1}{4} \sin\theta_i \sin\theta_j \; e^{-i(\varphi_i - \varphi_j)} \int r \sin\theta e^{-i\varphi} \left(V_{sc}(\vec{r}) + V_{ex}(\vec{r})\right)_\gamma r' \sin\theta' e^{i\varphi'} d\tau)^2 \Big] \\
= \; & f_1 \int \left(V_{sc}(\vec{r}) + V_{ex}(\vec{r})\right)_\gamma d\tau + f_2 \int \left(V_{sc}(\vec{r}) + V_{ex}(\vec{r})\right)_\gamma r^2 d\tau \\
& + f_3 \int r \cos\theta \left(V_{sc}(\vec{r}) + V_{ex}(\vec{r})\right)_\gamma r' \cos\theta' d\tau \; , \qquad \text{(B.21)}
\end{aligned}
$$

f_1, f_2 and f_3 have been defined before. Ion size parameters A_γ, J'_γ and J_γ are defined as:

$$A_\gamma = \int \left(V_{sc}(\vec{r}) + V_{ex}(\vec{r})\right)_\gamma d\tau - \sum_\lambda E^0_{\gamma,\lambda} B_{\gamma,\lambda} \; , \tag{B.22}$$

$$J'_\gamma = \int \left(V_{sc}(\vec{r}) + V_{ex}(\vec{r})\right)_\gamma r^2 d\tau - \sum_\lambda E^0_{\gamma,\lambda} K'_{\gamma,\lambda} \; , \tag{B.23}$$

$$J_\gamma = \int r \cos\theta \left(V_{sc}(\vec{r}) + V_{ex}(\vec{r})\right)_\gamma r' \cos\theta' d\tau - \sum_\lambda E^0_{\gamma,\lambda} K_{\gamma,\lambda} \; . \tag{B.24}$$

so that

$$\begin{aligned} &\langle \phi_i | V_{sc}(\vec{r}) + V_{ex}(\vec{r}) | \phi_j \rangle - \sum_{\gamma,\lambda} \left(E^0_{\gamma,\lambda} + \Delta E_\gamma \right) \langle \, \phi_i | \chi_{\gamma,\lambda} \rangle \langle \chi_{\gamma,\lambda} | \phi_j \rangle \\ = \;& \sum_\gamma \left(f_1 A_\gamma + f_2 J'_\gamma + f_3 J_\gamma \right) + \sum_\gamma \Delta E_\gamma \left(f_1 B_\gamma + f_2 K'_\gamma + f_3 K_\gamma \right) \; . \end{aligned} \tag{B.25}$$

Appendix C. Calculation of Interatomic Potential

One of the best known methods of generating interatomic potentials is the Electron Gas Model of Gordon and Kim [19]. This model computes the interatomic potentials taking account both of the overlap of the separate atomic densities and of electron correlation. The method is successful for predicting potentials between closed-shell atoms, ions and molecules. The theory is mainly based on three assumptions,

1. *Additive atomic electron densities.* No rearrangement or distortion of the separate atomic densities takes place when the atoms are brought together. The total electron density of two interacting atoms is therefore taken simply as the sum of the two atomic densities. This assumption is reasonable for systems which do not form strong chemical bonds and for distances of separation greater than about half R_m, the equilibrium internuclear separation. This is satisfied in the present work.

2. *Uniform electron gas.* The electron density is treated locally as relatively uniform, which is reasonably accurate in the outer portions of the atoms. Actually, only the outer regions of the atoms, in which the atomic densities overlap, contribute significantly to the interaction.

3. *Hartree-Fock wavefunction.* All it is required from the atomic wavefunction is the electron density, which is a one-electron property. Since Hartree-Fock predictions for one-electron properties are accurate to second-order in electron-electron interactions, they are satisfactory.

With these assumptions, we used Clementi-Roetti's [30] wavefunctions for the calculation of the electron densities. The total density ρ should be a sum of atomic densities ρ_a and ρ_b for the two separated atoms

$$\rho = \rho_a + \rho_b. \tag{C.1}$$

The interaction energy is written in terms of ρ.

The interatomic potential energy has two parts: the Coulomb interaction between all charges (both electrons and nuclei), which is calculated directly; and the interaction including the electronic kinetic energy, electron exchange effects, electron correlation, which is noted as electron gas terms and evaluated using a simple free electron gas model.

The Coulomb potential energy of two ions is

$$\begin{aligned} E_c &= \frac{Z_a Z_b}{R} + \frac{1}{2}\int\int \frac{[\rho_a(\vec{r}_1) + \rho_b(\vec{r}_1)][\rho_a(\vec{r}_2) + \rho_b(\vec{r}_2)]}{r_{12}} d\vec{r}_1 d\vec{r}_2 \\ & -Z_a \int \frac{[\rho_a(\vec{r}_1) + \rho_b(\vec{r}_1)]}{r_{1a}} d\vec{r}_1 - Z_b \int \frac{[\rho_a(\vec{r}_1) + \rho_b(\vec{r}_1)]}{r_{1b}} d\vec{r}_1, \end{aligned} \tag{C.2}$$

where Z_a and Z_b are the nuclear charges of ions A and B, R is the distance between the nuclei, r_{12} is the distance between two electrons, and r_{1a} and r_{2b} are electron-nuclear distances.

To obtain the pair Coulomb interaction, the Coulomb energies of the separated atoms should be subtracted from the total Coulomb energy. The Coulomb energies of the separated atoms are

$$E_c^{(a)} = \frac{1}{2}\int \frac{\rho_a(\vec{r}_1)\rho_a(\vec{r}_2)}{r_{12}} d\vec{r}_1 d\vec{r}_2 - Z_a \int \frac{\rho a(\vec{r}_1)}{r_{1a}} d\vec{r}_1 \ , \tag{C.3}$$

$$E_c^{(b)} = \frac{1}{2}\int \frac{\rho_a(\vec{r}_1)\rho_a(\vec{r}_2)}{r_{12}} d\vec{r}_1 d\vec{r}_2 - Z_b \int \frac{\rho b(\vec{r}_1)}{r_{1b}} d\vec{r}_1 \ . \tag{C.4}$$

After the subtraction, and using the relations

$$\int \rho_a(\vec{r})d\vec{r} = Z_p \ , \tag{C.5}$$

and

$$\int \rho_b(\vec{r})d\vec{r} = Z_n \ , \tag{C.6}$$

where Z_p is the number of electrons of the positive ion, and Z_n is that of the negative ion. The Coulombic interaction is obtained for ion pairs in spherical polar coordinates

$$\begin{aligned} V_c &= \int_0^\infty \rho_a(r_1)r_1^2dr_1 \int_0^\infty \rho_b(r_2)r_2^2dr_2 \int_0^{2\pi} d\phi_1 \int_0^{2\pi} d\phi_2 \\ &\quad \times \int_0^\pi \sin\theta_1 d\theta_1 \int_0^\pi \sin\theta_2 d\theta_2 (\frac{Z_aZ_b}{Z_pZ_n}R_{-1} + r_{12}^{-1} - \frac{Z_b}{Z_n}r_{1b}^{-1} - \frac{Z_a}{Z_p}r_{2a}^{-1}) \\ &= \int_0^\infty 4\pi r_1^2dr_1 \int_0^\infty 4\pi r_2^2dr_2\rho_a(r_1)\rho_b(r_2)I. \end{aligned} \tag{C.7}$$

The following integrals [119] are used for the expression of I in the above equation (C.7):

$$\begin{aligned} \langle R^{-1}\rangle &\equiv \left(\frac{1}{4\pi}\right)^2 \int_0^{2\pi} d\phi_1 \int_0^{2\pi} d\phi_2 \int_0^\pi \sin\theta_1 d\theta_1 \int_0^\pi \sin\theta_2 d\theta_2 R^{-1} \\ &= R^{-1} \ , \end{aligned} \tag{C.8}$$

$$\begin{aligned} \langle r_{1b}^{-1}\rangle &\equiv \left(\frac{1}{4\pi}\right)^2 \int_0^{2\pi} d\phi_1 \int_0^{2\pi} d\phi_2 \int_0^\pi \sin\theta_1 d\theta_1 \int_0^\pi \sin\theta_2 d\theta_2 r_{1b}^{-1} \\ &= \frac{2}{R + r_1 + |R - r_1|} \ , \end{aligned} \tag{C.9}$$

$$\begin{aligned} \langle r_{2a}^{-1} \rangle &\equiv \left(\frac{1}{4\pi}\right)^2 \int_0^{2\pi} d\phi_1 \int_0^{2\pi} d\phi_2 \int_0^{\pi} \sin\theta_1 d\theta_1 \int_0^{\pi} \sin\theta_2 d\theta_2 r_{2a}^{-1} \\ &= \frac{2}{R + r_2 + |R - r_2|} , \end{aligned} \tag{C.10}$$

$$\begin{aligned} \langle r_{12}^{-1} \rangle &\equiv \left(\frac{1}{4\pi}\right)^2 \int_0^{2\pi} d\phi_1 \int_0^{2\pi} d\phi_2 \int_0^{\pi} \sin\theta_1 d\theta_1 \int_0^{\pi} \sin\theta_2 d\theta_2 r_{12}^{-1} \\ &\equiv F(R, r_1, r_2) \\ &= \begin{cases} \frac{2}{R+r_1+|R-r_1|} , & for\ r_2 < |R - r_1| \ ; \\ \frac{1}{2}\left(\frac{1}{r_1} + \frac{1}{r_2}\right) - \frac{R}{4r_1r_2} - \frac{(r_1-r_2)^2}{4Rr_1r_2} , & \\ \qquad for\ |R - r_1| < r_2 < R + r_1 \ ; & \\ r_2^{-1} , & for\ r_2 > R + r_1 \ . \end{cases} \end{aligned} \tag{C.11}$$

The expression of I then is

$$\begin{aligned} I &= \frac{Z_a Z_b}{Z_p Z_n} \cdot \frac{1}{R} + F(R, r_1 r_2) - \frac{Z_b}{Z_n} \cdot \frac{2}{R + r_1 + |R - r_1|} \\ &\quad - \frac{Z_a}{Z_p} \cdot \frac{2}{R + r_2 + |R - r_2|} . \end{aligned} \tag{C.12}$$

The double integral over the electron distances r_1 and r_2 is then carried out numerically using Gauss-Laguerre quadrature

$$\begin{aligned} \int_0^{\infty} G(x) dx &= \sum_{i=1}^{n} w_i e^{x_i} G(x_i) = \sum_{i=1}^{n} w_i' G(x_i) , \\ w_i' &= w_i e^{x_i} . \end{aligned} \tag{C.13}$$

Where $G(x)$ is the integrand, x_i is the zero point of Laguerre polynomials, and w_i is the weight factor. Since the wavefunctions of the cations involved in our work are farely compact, 80 × 80 points were needed to give four-figure accuracy.

The energy density of electron gas is defined as a sum of two parts, the Hartree-Fock portion (noted as E_{HF}) and the electron correlation (noted as E_{corr}).

The Hartree-Fock portion includes the zero-point kinetic energy density and the exchange contribution, (the Coulomb terms was already calculated separately)

$$E_{HF}(\rho) = C_k\rho^{2/3} + C_e\rho^{1/3} , \tag{C.14}$$

where

$$C_k = \frac{3}{10}(3\pi^2)^{2/3} ,$$

and

$$C_e = -\frac{3}{4}(3/\pi)^{1/3} .$$

The correlation energy density is

$$\begin{aligned} E^l_{corr}(r_s) &= -0.438r_s^{-1} + 1.325rs^{-3/2} - 1.47r_s^{-2} - 0.4r_s^{-5/2}, \\ &\quad \mathit{for\ low\ density},\ r_s > 10; \\ E^h_{corr}(r_s) &= 0.0311lnr_s - 0.048 + 0.009r_slnr_s - 0.01r_s, \\ &\quad \mathit{for\ high\ density},\ r_s < 0.7; \\ E^i_{corr}(r_s) &\approx -0.06156 + 0.01898lnr_s, \\ &\quad \mathit{interpolation\ formula},\ \mathit{for}\ 0.7 < r_s < 10, \end{aligned} \tag{C.15}$$

where the radius r_s is related to the electron density ρ by $\rho 4\pi r_s^3/3 = 1$.

Then the total energy density functional for the electron gas is

$$E_G(\rho) = E_{HF}(\rho) + E_{corr}(\rho), \tag{C.16}$$

then the electron-gas contribution to the interatomic interaction is given by

$$\begin{aligned} V_G &= \int d\bar{r}\{[\rho_a(r_a) + \rho_b(r_b)]E_G(\rho_a + \rho_b) \\ &\quad -\rho_a(r_a)E_G(\rho_a) - \rho_b(r_b)E_G(\rho_b)\}. \end{aligned} \tag{C.17}$$

Where r_a and r_b are as shown in Fig. C.1.

The total interatomic potential is the sum of the Coulomb terms V_C (C.7) and the electron gas terms V_G (C.17).

To evaluate the integrals of electron gas terms in equation C.17, it is more convenient to use the prolate spheroidal coordinate system, in which

$$r_a = \frac{R}{2}(\sqrt{1+\lambda^2} + \mu^2),$$

$$r_b = \frac{R}{2}(\sqrt{1+\lambda^2} - \mu^2), \tag{C.18}$$

and

$$d\bar{r} = \frac{R^3}{8}\frac{\lambda}{\sqrt{1+\lambda^2}}(\lambda^2 - \mu^2 - 1)d\phi d\mu d\lambda. \tag{C.19}$$

The angular integration over ϕ is 2π since the electron density is cylindrically symmetric about the axis joining a and b. The λ and μ integrations were carried out using Gauss-Laguerre and Gauss-Legendre numerical quadratures, respectively. 80×80 and 48×48 points were needed for λ and μ, respectively, to make the convergence smoothly and give about three-figure accuracy. The program (Fortran) to calculate the repulsive part of the total interatomic potential is given at the end of this appendix.

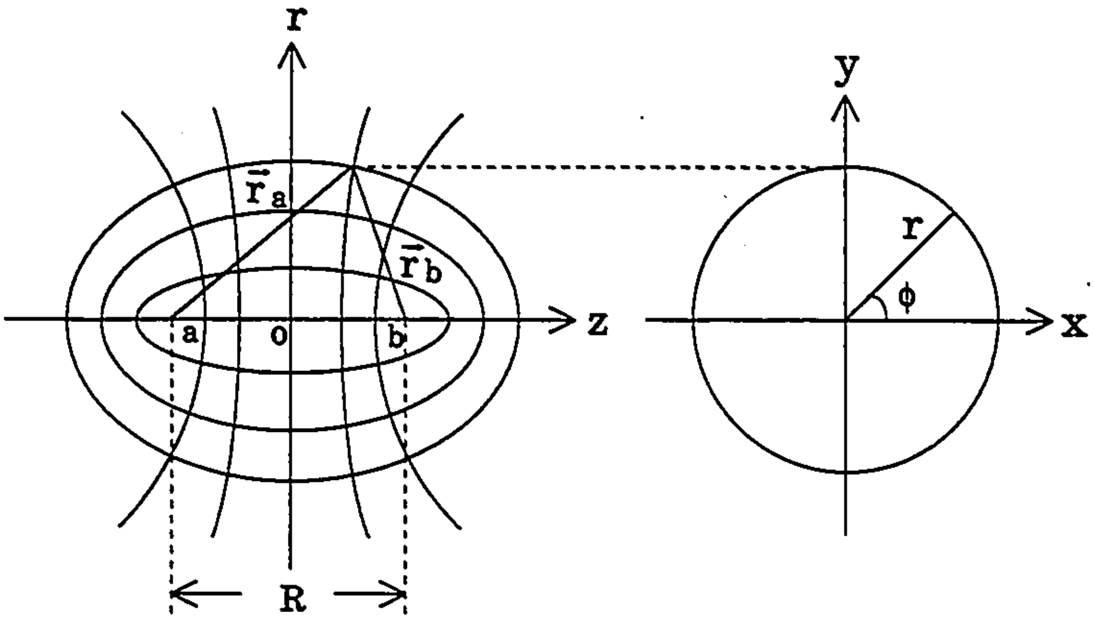

Figure C.1: Prolate Spheroidal Coordinate System

Here is a brief introduction of the prolate spheroidal coordinate system [120].

It is simpler to proceed by considering the equation of an ellipse and a hyperbola

$$\frac{z^2}{a_1^2} + \frac{x^2}{a_1^2(1-e_1^2)} = 1,$$

$$\frac{z^2}{a_2^2} - \frac{x^2}{a_2^2(e_2^2-1)} = 1, \tag{C.20}$$

where a is the semi-major axis and $e_1 < 1$ is the eccentricity of the ellipse, $e_2 > 1$, the eccentricity of the hyperbola. Now substitute $\frac{R}{2}ch(u)$ for a_1 and $sech(u)$ for e_1 in the ellipse, $\frac{R}{2}\cos v$ for a_2 and $\sec v$ for e_2 in the hyperbola and finally $x^2+y^2=r^2$ for x^2, we obtain

$$\frac{z^2}{(\frac{R}{2})^2 ch^2(u)} + \frac{r^2}{(\frac{R}{2})^2 sh^2(u)} = 1,$$

$$\frac{z^2}{(\frac{R}{2})^2 \cos^2 v} - \frac{r^2}{(\frac{R}{2})^2 \sin^2 v} = 1, \tag{C.21}$$

with

$$0 \le u \le \infty \quad 0 \le v \le \pi$$

These equations represent the confocal families of: (1) prolate spheroids ($u = const$) and (2) hyperboloids (of two sheets) of revolution ($v = const$) obtained by rotating the ellipse and hyperbolas around the z-axis. The intersection of these surfaces, as shown in Fig. C.1, will be a circle of radius r; hence if $0 \le \phi \le 2\pi$, the addition of (3), a family of planes through the z-axis ($\phi = const$), to the spheroids and hyperboloids gives us three suitable coordinate surfaces (u, v, ϕ). These three surfaces are orthogonal and all of them have common foci ($c^2 = (\frac{R}{2})^2$).

Solving z and r from equation C.21, then setting $x = r\cos\phi$, $y = r\sin\phi$, we obtain

$$\begin{aligned} x &= \frac{R}{2} sh(u)\sin v\cos\phi, \\ y &= \frac{R}{2} sh(u)\sin v\sin\phi, \\ z &= \frac{R}{2} ch(u)\cos v. \end{aligned}$$

For a two-center problem such as the electron gas terms, it is convenient to introduce the coordinates λ and μ in place of $sh(u)$ and $\cos v$

$$\begin{aligned} 0 &\leq \lambda \leq \infty, \quad using\ Gauss-Laguerre\ quadrature; \\ -1 &\leq \mu \leq 1, \quad using\ Gauss-Legendre\ quadrature. \end{aligned} \tag{C.22}$$

Then

$$\begin{aligned} x &= \frac{R}{2}\lambda\sqrt{1-\mu^2}\cos\phi, \\ y &= \frac{R}{2}\lambda\sqrt{1-\mu^2}\sin\phi, \\ z &= \frac{R}{2}\sqrt{\lambda^2+1}\mu. \end{aligned}$$

and

$$J = \frac{D(x,y,z)}{D(\lambda,\mu,\phi)} = \frac{R^3}{8}\cdot\frac{\lambda}{\sqrt{1+\lambda^2}}(\lambda^2-\mu^2-1) \tag{C.23}$$

According to the properties of the ellipse and hyperbola, we have

$$\begin{aligned} r_a + r_b &= 2a_1 = R\cdot ch(u), \\ r_a - r_b &= 2a_2 = R\cdot\cos v, \end{aligned}$$

it leads to

$$\begin{aligned} r_a &= \frac{R}{2}(\sqrt{1+\lambda^2}+\mu^2), \\ r_b &= \frac{R}{2}(\sqrt{1+\lambda^2}-\mu^2). \end{aligned}$$

FORTRAN PROGRAM

```
C----------------------------------------------------------------C
C THIS PROGRAM IS FOR CALCULATING THE INTERACTION ENERGY          C
C (REPULSIVE PART, WITH GORDON-KIM METHOD) BETWEEN ION            C
C PAIRS OR ATOM PAIRS.                                             C
C  LFION:    THE FLAG TO INDICATE IF IT IS AN ION PAIR OR AN       C
C            ATOM PAIR TO BE CALCULATED.                           C
C            LFION=1: ION PAIRS, 0: ATOM PAIRS.                    C
C  ZP:       NO. OF NUCLEAR CHARGES OF THE POSITIVE ION.           C
C  ZN:       NO. OF NUCLEAR CHARGES OF THE NEGATIVE ION.           C
C  ZEP:      NO. OF ELECTRONS OF THE POSITIVE ION.                 C
C  ZEN:      NO. OF ELECTRONS OF THE NEGATIVE ION.                 C
C  NR:       NO. OF VALUES OF R.                                   C
C  DFAC:     THE PARAMETER TO ADJUST THE SCALE.                    C
C                                                                  C
C  NLAGR:    ORDER OF GAUSS-LAGUERRE NUMERICAL QUADRATURES.        C
C  NLEGD:    ORDER OF GAUSS-LEGENDRE NUMERICAL QUADRATURES;        C
C  XLAGR:    ZERO POINT OF LAGUERRE POLYNOMIALS.                   C
C  XLEGD:    ZERO POINT OF LEGENDRE POLYNOMIALS;                   C
C  XLAGR:    WEIGHT FACTOR OF LAGUERRE NUMERICAL                   C
C            QUADRATURES.                                          C
C  XLEGD:    WEIGHT FACTOR OF LEGENDRE NUMERICAL                   C
C            QUADRATURES.                                          C
C                                                                  C
C  NPK/NNK:  NO. OF ORBITAL TYPES OF A POSITIVE/NEGATIVE ION.      C
C  NORBP/NORBN (1-D ARRAR):                                        C
C            NUMBER OF s (p, d, ...) TYPE OF ORBITALS OF A         C
C            POSITIVE/NEGATIVE ION.                                C
C  NBASP/NBASN (1-D ARRAY):                                        C
C            NUMBER OF BASES FOR s (p, d, ...) TYPE OF ORBITAL     C
C            OF A POSITIVE/NEGATIVE ION.                           C
C  INDP/INDN (2-D ARRAR):                                          C
C            INDEX OF BASES OF A POSITIVE/NEGATIVE ION.            C
C  BASP/BASN (2-D ARRAR):                                          C
C            BASES OF A POSITIVE/NEGATIVE ION,                     C
C  COEP/COEN (3-D ARRAR):                                          C
C            COEFFICIENTS OF DIFFERENT BASES AND DIFFERENT         C
C            s (p, d, ...) ORBITALS.                               C
C----------------------------------------------------------------C
      IMPLICIT REAL*8(A-H,O-Z)
      DIMENSION R0(100),R(100)
      COMMON/C1/ZP,ZN,ZEP,ZEN,LFION
      COMMON/C2/XLAGR(80),WLAGR(80),NLAGR
      COMMON/C3/XLEGD(48),WLEGD(48),NLEGD
      COMMON/C4/ROP(80),RON(80)
      COMMON/C5/DFAC,PI
      COMMON/DAION/NBASP(3),NORBP(3),INDP(10,3),BASP(10,3),
     * COEP(10,5,3),NBASN(3),NORBN(3),INDN(10,3),BASN(10,3),
     * COEN(10,5,3),NPK,NNK
```

```
C
  1 FORMAT(/1X,'*****DATA OF CATION*****')
  2 FORMAT(/1X,'*****DATA OF ANION*****')
  3 FORMAT(/1X,'INDEX',4X,'BASIS',I8,4I10)
 21 FORMAT(4F6.1)
 32 FORMAT(1X,5I4,8X,'LFION,NR,NPK,NNK,NNEIB')
 33 FORMAT(1X,4I4,12X,'NLLAG,NHLAG,NLMEW,NHMEW')
 22 FORMAT(1X,4F6.1,4X,'ZP,ZN,ZEP,ZEN')
 23 FORMAT(8I4)
 34 FORMAT(F12.6,F6.1)
 35 FORMAT(1X,F6.1,10X,'DFAC')
 24 FORMAT(/1X,'NO. OF S ORBITS:',I2,4X,'NO. OF S BASIS:',I2)
 25 FORMAT(/1X,'NO. OF P ORBITS:',I2,4X,'NO. OF P BASIS:',I2)
 26 FORMAT(/1X,'NO. OF D ORBITS:',I2,4X,'NO. OF D BASIS:',I2)
 27 FORMAT(I4,2X,6F10.5)
 28 FORMAT(2D25.15)
 29 FORMAT(8F7.2)
C
    READ  (5,23)LFION,NR,NPK,NNK
    WRITE(6,32)LFION,NR,NPK,NNK
    READ  (5,23)NLAGR,NLEGD
    WRITE(6,33)NLAGR,NLEGD
    READ  (5,21)ZP,ZN,ZEP,ZEN
    WRITE(6,22)ZP,ZN,ZEP,ZEN
    READ  (5,34)DFAC
    WRITE(6,35)DFAC
C-----------------------------------------------------------------C
C  READ POSITIVE ION WAVEFUNCTIONS                                C
C-----------------------------------------------------------------C
    WRITE(6,1)
    DO 10 K=1,NPK
        READ (5,23)NORBP(K),NBASP(K)
        IF(K.EQ.1) WRITE(6,24)NORBP(K),NBASP(K)
        IF(K.EQ.2) WRITE(6,25)NORBP(K),NBASP(K)
        IF(K.EQ.3) WRITE(6,26)NORBP(K),NBASP(K)
        WRITE(6,3) (I,I=1,NORBP(K))
        DO 20 I=1,NBASP(K)
                READ  (5,27)INDP(I,K),BASP(I,K),(COEP(I,J,K),J=1,NORBP(K))
                WRITE(6,27)INDP(I,K),BASP(I,K),(COEP(I,J,K),J=1,NORBP(K))
 20     CONTINUE
 10 CONTINUE
C-----------------------------------------------------------------C
C  READ NEGATIVE ION WAVEFUNCTIONS                                C
C-----------------------------------------------------------------C
    WRITE(6,2)
    DO 30 K=1,NNK
        READ (5,23)NORBN(K),NBASN(K)
        IF(K.EQ.1) WRITE(6,24)NORBN(K),NBASN(K)
        IF(K.EQ.2) WRITE(6,25)NORBN(K),NBASN(K)
```

```
        IF(K.EQ.3) WRITE(6,26)NORBN(K),NBASN(K)
        WRITE(6,3)(I,I=1,NORBN(K))
        DO 40 I=1,NBASN(K)
              READ  (5,27)INDN(I,K),BASN(I,K),(COEN(I,J,K),J=1,NORBN(K))
              WRITE(6,27)INDN(I,K),BASN(I,K),(COEN(I,J,K),J=1,NORBN(K))
 40     CONTINUE
 30  CONTINUE
C
     READ (5,28)(XLAGR(I),WLAGR(I),I=1,NLAGR)
     READ (5,28)(XLEGD(I),WLEGD(I),I=1,NLEGD)
     READ (5,29)(R(I),I=1,NR)
     PI=DACOS(-1.0D0)
C
     DO 50 I=1,NLAGR
        CALL CHADEN( 1,1,XLAGR(I),ROP(I))
        CALL CHADEN(-1,1,XLAGR(I),RON(I))
 50  CONTINUE
 55  FORMAT(1X,2D12.4)
C
     WRITE(6,81)
     DO 80 I=1,NR
        CALL COUL(R(I),VCOUL)
        CALL HUCO(R(I),VK,VE,VC)
        ETOT=VCOUL+VK+VE+VC
        EREP=ETOT+(ZP-ZEP)/R(I)
        EREP=ETOT*27.2116D0
        WRITE(6,82)R(I),EREP
 80  CONTINUE
 81  FORMAT(/1X,'R(A.U.)',5X,'EREP(eV)')
 82  FORMAT(2X,F5.2,3X,D12.5)
      STOP
      END
C-----------------------------------------------------------------------C
C S/R  CALCULATE COULOMBIC INTERACTIONS.                                 C
C-----------------------------------------------------------------------C
     SUBROUTINE COUL(R,VCOUL)
     IMPLICIT REAL*8(A-H,O-Z)
     COMMON/C1/ZP,ZN,ZEP,ZEN,LFION
     COMMON/C2/XLAGR(80),WLAGR(80),NLAGR
     COMMON/C4/ROP(80),RON(80)
     COMMON/C5/DFAC,PI
C
     CR=R*DFAC
     VS=0.0D0
     VCOUL=0.0D0
     DO 110 I=1,NLAGR
        RA=XLAGR(I)
        ROPP=ROP(I)
        WXA=WLAGR(I)*RA**2.0D0
```

```
         DO 120 J=1,NLAGR
               RB=XLAGR(J)
               RONN=RON(J)
               WXB=WLAGR(J)*RB**2.0D0
               POWER=DLOG(ROPP)+DLOG(RONN)
               IF(POWER.LT.-90.0D0) RONN=0.0D0
               RPB=2.0D0/(CR+RA+DABS(CR-RA))
               RNA=2.0D0/(CR+RB+DABS(CR-RB))
               IF (LFION.EQ.1) THEN
                     F1=(ZP*ZN+1)/(ZEP*ZEN*CR)
                     F2=ZN/ZEN*RPB
                     F3=ZP/ZEP*RNA
                     F4=FRPN(CR,RA,RB)
                     F=F1+F4-F2-F3
               ELSE
                     F1=1.0D0/CR
                     F4=FRPN(CR,RA,RB)
                     F=F1+F4-2.0D0*RPB
               END IF
               VS=VS+WXA*ROPP*WXB*RONN*F
120      CONTINUE
110   CONTINUE
      IF (LFION.EQ.1) THEN
         VCOUL=(16*PI*PI*VS-1.0D0/CR)*DFAC
      ELSE
         VCOUL=(16*PI*PI*VS)*DFAC
      END IF
      RETURN
      END
C-----------------------------------------------------------------------C
C S/R  CALCULATE HARTREE-FOCK AND CORRELATION ENERGY.                   C
C-----------------------------------------------------------------------C
      SUBROUTINE HUCO(R,VK,VE,VC)
      IMPLICIT REAL*8(A-H,O-Z)
      COMMON/C2/XLAGR(80),WLAGR(80),NLAGR
      COMMON/C3/XLEGD(48),WLEGD(48),NLEGD
      COMMON/C5/DFAC,PI
C
      CK=0.3D0*((3.0D0*PI*PI)**(2.0D0/3.0D0))
      CE=-0.75D0*((3.0D0/PI)**(1.0D0/3.0D0))
      VK=0.0D0
      VE=0.0D0
      DO 210 I1=1,NLAGR
         TXX=DSQRT(1+XLAGR(I1)*XLAGR(I1))
         DO 220 J1=1,NLEGD
               RA=R*(TXX+XLEGD(J1))/2.0D0
               CALL CHADEN(1,2,RA,ROHP)
               RB=R*(TXX-XLEGD(J1))/2.0D0
               CALL CHADEN(-1,2,RB,ROHN)
               SRO=ROHP+ROHN
```

```
                   IF (SRO.LT.0.1D-45) THEN
                             TKS=0.0D0
                             TES=0.0D0
                   ELSE
                             TKS=SRO**(5.0D0/3.0D0)
                             TES=SRO**(4.0D0/3.0D0)
                   END IF
                   IF (ROHP.LT.0.1D-42) THEN
                             TKP=0.0D0
                             TEP=0.0D0
                   ELSE
                             TKP=ROHP**(5.0D0/3.0D0)
                             TEP=ROHP**(4.0D0/3.0D0)
                   END IF
                   IF (ROHN.LT.0.1D-42) THEN
                             TKN=0.0D0
                             TEN=0.0D0
                   ELSE
                             TKN=ROHN**(5.0D0/3.0D0)
                             TEN=ROHN**(4.0D0/3.0D0)
                   END IF
                   FAC1=XLAGR(I1)*XLAGR(I1)-XLEGD(J1)*XLEGD(J1)+1.0D0
                   FAC2=XLAGR(I1)/TXX*WLAGR(I1)*WLEGD(J1)
                   CC=PI/4.0D0*(R**3.0D0)*FAC1*FAC2
                   TK=TKS-TKP-TKN
                   TE=TES-TEP-TEN
                   VK=VK+CC*TK
                   VE=VE+CC*TE
220         CONTINUE
210   CONTINUE
      VK=CK*VK
      VE=CE*VE
      VC=0.0D0
      DO 510 I2=1,NLAGR
          TXX=DSQRT(1+XLAGR(I2)*XLAGR(I2))
          DO 520 J2=1,NLEGD
                     RA=R*(TXX+XLEGD(J2))/2.0D0
                     CALL CHADEN(1,2,RA,ROHP)
                     RB=R*(TXX-XLEGD(J2))/2.0D0
                     CALL CHADEN(-1,2,RB,ROHN)
                     SRO=ROHP+ROHN
                     IF (SRO.LT.0.1D-50) THEN
                               TCS=0.0D0
                     ELSE
                               TCS=SRO*FCOOR(SRO)
                     END IF
                     IF (ROHP.LT.0.1D-50) THEN
                               TCP=0.0D0
```

```
               ELSE
                     TCP=ROHP*FCOOR(ROHP)
               END IF
               IF (ROHN.LT.0.1D-50) THEN
                     TCN=0.0D0
               ELSE
                     TCN=ROHN*FCOOR(ROHN)
               END IF
               FAC1=XLAGR(I2)*XLAGR(I2)-XLEGD(J2)*XLEGD(J2)+1.0D0
               FAC2=XLAGR(I2)/TXX*WLAGR(I2)*WLEGD(J2)
               CC=PI/4.0D0*(R**3.0D0)*FAC1*FAC2
               TC=TCS-TCP-TCN
               VC=VC+CC*TC
520      CONTINUE
510   CONTINUE
      RETURN
      END
C---------------------------------------------------------------C
C S/R  CALCULATE CHARGE DENSITY.                                 C
C---------------------------------------------------------------C
      SUBROUTINE CHADEN(LFPN,LFFN,YY,RO)
      IMPLICIT REAL*8(A-H,O-Z)
      COMMON/C5/DFAC,PI
      COMMON/DAION/NBASP(3),NORBP(3),INDP(10,3),BASP(10,3),
     * COEP(10,5,3),NBASN(3),NORBN(3),INDN(10,3),BASN(10,3),
     * COEN(10,5,3),NPK,NNK
C
      RO=0.0D0
      IF (LFPN.EQ.1) THEN
         DO 310 K=1,NPK
               ROL=0.0D0
               DO 320 J=1,NORBP(K)
                     POSI=0.0D0
                     DO 330 I=1,NBASP(K)
                           IF (LFFN.EQ.1) THEN
                                 FBASP=BASP(I,K)/DFAC
                           ELSE
                                 FBASP=BASP(I,K)
                           END IF
                           ZNOM=FNOM(FBASP,INDP(I,K))
                           POW=FBASP*YY
                           IF (POW.GT.90) THEN
                                 CKI=0.0D0
                           ELSE
                                 CKI=ZNOM*(YY**INDP(I,K))/DEXP(POW)
                           END IF
                           POSI=POSI+COEP(I,J,K)*CKI
330                  CONTINUE
```

```
                     IF (ABS(POSI).LT.0.1D-38) GO TO 320
                     ROL=ROL+POSI*POSI
 320           CONTINUE
               RO=RO+ROL*(2*K-1)
 310     CONTINUE
      ELSE
         DO 410 K=1,NNK
               ROL=0.0D0
               DO 420 J=1,NORBN(K)
                     POSI=0.0D0
                     DO 430 I=1,NBASN(K)
                           IF (LFFN.EQ.1) THEN
                                 FBASN=BASN(I,K)/DFAC
                           ELSE
                                 FBASN=BASN(I,K)
                           END IF
                           ZNOM=FNOM(FBASN,INDN(I,K))
                           POW=FBASN*YY
                           IF (POW.GT.90) THEN
                                 CKI=0.0D0
                           ELSE
                                 CKI=ZNOM*(YY**INDN(I,K))/DEXP(POW)
                           END IF
                           POSI=POSI+COEN(I,J,K)*CKI
 430                 CONTINUE
                     IF (ABS(POSI).LT.0.1D-38) GO TO 420
                     ROL=ROL+POSI*POSI
 420           CONTINUE
               RO=RO+ROL*(2*K-1)
 410     CONTINUE
      END IF
      RO=RO/(2.0D0*PI)
      RETURN
      END
C
C
      FUNCTION FNOM(BAS,IND)
      IMPLICIT REAL*8(A-H,O-Z)
      NN=2*(IND+1)
      DFCTO=1.0D0
      DO 510 I=1,NN
         DFCTO=DFCTO*I
 510  CONTINUE
      DIND=DBLE(IND)
      FNOM=((2.0D0*BAS)**(DIND+1.5D0))/(DFCTO**0.5D0)
      END
C
C
```

```
      FUNCTION FRPN(R,RA,RB)
      IMPLICIT REAL*8(A-H,O-Z)
      DRRA=DABS(R-RA)
      SRRA=R+RA
      IF (RB.LT.DRRA) THEN
          FRPN=2.0D0/(R+RA+DRRA)
      ELSE IF(RB.GT.SRRA) THEN
          FRPN=1.0D0/RB
      ELSE
          FRPN=(1.0D0/RA+1.0D0/RB)/2.0D0-R/4.0D0/RA/RB
     *    -(RA-RB)*(RA-RB)/(4.0D0*R*RA*RB)
      END IF
      RETURN
      END
C
C
      FUNCTION FCOOR(RO)
      IMPLICIT REAL*8(A-H,O-Z)
      PI=DACOS(-1.0D0)
      RS=(3.0D0/4.0D0/PI/RO)**(1.0D0/3.0D0)
      IF (RS.LT.0.7D0) THEN
          FCOOR=0.0311D0*DLOG(RS)-0.048D0
     *     +0.009D0*RS*DLOG(RS)-0.01D0*RS
      ELSE IF (RS.GT.0.1D+02) THEN
          FCOOR=-0.438D0/RS+1.325D0/(RS**1.5)
     *     -1.47D0/(RS**2.0)-0.4D0/(RS**2.5)
      ELSE
          FCOOR=-0.06156D0+0.01898D0*DLOG(RS)
      END IF
      END
```

INPUT DATA

(This input data is for calculating the repulsive energy between In^+ and Br^-. The order of Laguerre numerical quadratures is 80, and the one of Legendre is 48. Values in the left side are the zero points, and values in the right side are weight factors.)

```
 1 40  3  3            ***LFION,NR,NPK,NNK
80 48                  ***NLAGR,NLEGD
49.0 35.0 48.0 36.0    ***ZP,ZN,ZEP,ZEN
10.0                   ***DFAC
 5 11                                    *** S ORBITS ***  IN+
 0 50.15070  0.86984   0.01440 -0.01057 -0.00283  0.00085
 0 34.97610  0.14569   0.50458 -0.21400 -0.09452  0.02714
 1 24.55580 -0.05141  -0.13212 -0.44604 -0.20465  0.06085
 1 20.83330  0.04065  -1.06700  1.21694  0.54816 -0.16060
 2 15.34990 -0.00715  -0.01686 -0.20750 -0.04061  0.00937
 2 10.07610  0.00345  -0.00852 -1.10744 -0.74470  0.22959
 3  6.24000 -0.00994   0.04055  0.58366  1.40335 -0.41351
 3  4.39864  0.03122  -0.13043 -1.86048 -1.57045  0.18795
 4  2.64214 -0.00015   0.00046  0.00829  0.01763  0.55617
 4  1.62892  0.00002  -0.00004 -0.00114 -0.00315  0.54435
 4  4.87386 -0.02341   0.09830  1.39535  1.50078 -0.16715
 3  7                                    *** P ORBITS ***  IN+
 1 31.80050 -0.13531 -0.02976  0.01000
 1 20.93160 -0.86597 -0.48115  0.20252
 2 11.49460 -0.04141  0.66664 -0.20590
 2  9.66376  0.02603  0.43599 -0.42595
 3  7.30333 -0.00262  0.04313  0.29493
 3  5.17808  0.00041 -0.00469  0.68070
 3  3.50539  0.00006  0.00126  0.25325
 2  5                                    *** D ORBITS ***  IN+
 2 17.18530 -0.24029 -0.08709
 2  9.91941 -0.77921 -0.27952
 3  6.04509 -0.04908  0.39941
 3  3.72813  0.01005  0.56395
 3  2.29150 -0.00252  0.20448
 4 10                                    *** S ORBITS *** Br-( in lattice)
 0 32.83790 -0.80855 -0.37829  0.14605 -0.04120
 0 41.13520 -0.19674  0.02716 -0.00771  0.00058
 1 26.42870  0.00607 -0.20459  0.10114 -0.03348
 1 15.94410 -0.00564  1.05731 -0.48088  0.14987
 2 13.73830  0.00262  0.19545 -0.28102  0.09075
 2  8.75244 -0.00106  0.00594  0.54030 -0.17759
 2  5.99564  0.00048  0.00130  0.71412 -0.28975
 3  3.63572 -0.00014 -0.00027  0.00495  0.45178
 3  2.37420  0.00009  0.00013  0.00133  0.55278
 3  1.51690 -0.00003 -0.00005 -0.00023  0.15953
```

(INPUT DATA)

```
3  9                                          *** P ORBITS *** Br- in lattice
1  15.80950 -0.73379 -0.30621  0.07896
1  23.96750 -0.10307 -0.03753  0.00673
2  14.97930 -0.17237 -0.12902  0.02509
2   8.60775 -0.04791  0.41356 -0.08655
2   5.87791  0.02504  0.67051 -0.23825
3   5.16140 -0.01002  0.06117  0.06158
3   2.81552  0.00191  0.01008  0.50790
3   1.68578 -0.00091 -0.00325  0.45248
3   1.04140  0.00030  0.00110  0.17373
1  5                                          *** D ORBITS *** Br- in lattice
2   4.85590  0.46278
2   3.11959  0.11069
2   7.33254  0.31176
2  10.10240  0.19315
2  16.28710  0.02961
 0.179604233006984D-01   0.460931031330610D-01        START*LAGR80*
 0.946399129943540D-01   0.107313007783933D+00
 0.232622868125868D+00   0.168664429547948D+00
 0.431992547802387D+00   0.230088089384940D+00
 0.692828861352022D+00   0.291601302502438D+00
 0.101523255618947D+01   0.353226753575408D+00
 0.139932768784287D+01   0.414988177550940D+00
 0.184526230383585D+01   0.476909792302936D+00
 0.235320887160926D+01   0.539016218474955D+00
 0.292336468655543D+01   0.601332497447191D+00
 0.355595231404613D+01   0.663884136396681D+00
 0.425122008230988D+01   0.726697163614157D+00
 0.500944263362016D+01   0.789798189428429D+00
 0.583092153860872D+01   0.853214471438152D+00
 0.671598597785132D+01   0.916973983833893D+00
 0.766499349489177D+01   0.981105491004006D+00
 0.867833082516770D+01   0.104563862580654D+01
 0.975641480574293D+01   0.111060397300026D+01
 0.108996933712879D+02   0.117603315841226D+01
 0.121086466423657D+02   0.124195894449809D+01
 0.133837881127786D+02   0.130841533303134D+01
 0.147256659435086D+02   0.137543767574893D+01
 0.161348643716625D+02   0.144306279387849D+01
 0.176120052438144D+02   0.151132910758831D+01
 0.191577496842412D+02   0.158027677653099D+01
 0.207727999097921D+02   0.164994785280268D+01
 0.224579012045405D+02   0.172038644781283D+01
 0.242138440689586D+02   0.179163891476094D+01
 0.260414665601656D+02   0.186375404864910D+01
 0.279416568418595D+02   0.193678330603071D+01
 0.299153559649010D+02   0.201078104701134D+01
 0.319635609022089D+02   0.208580480238741D+01
 0.340873278647262D+02   0.216191556924160D+01
 0.362877759287815D+02   0.223917813882365D+01
```

(INPUT DATA)

```
 0.385660910092922D+02  0.231766146114652D+01
 0.409235302180313D+02  0.239743905144001D+01
 0.433614266517312D+02  0.247858944444973D+01
 0.458811946612789D+02  0.256119670357790D+01
 0.484843356608332D+02  0.264535099306969D+01
 0.511724445446070D+02  0.273114922289915D+01
 0.539472167895544D+02  0.281869577775934D+01
 0.568104563346362D+02  0.290810334368223D+01
 0.597640843421100D+02  0.299949384839686D+01
 0.628101489639265D+02  0.309299953469357D+01
 0.659508362574561D+02  0.318876418994712D+01
 0.691884824202363D+02  0.328694455975338D+01
 0.725255875442633D+02  0.338771197960398D+01
 0.759648311278642D+02  0.349125426598732D+01
 0.795090896290888D+02  0.359777791769613D+01
 0.831614564010537D+02  0.370751069001746D+01
 0.869252644196156D+02  0.382070461965312D+01
 0.908041123009408D+02  0.393763959771431D+01
 0.948018942159474D+02  0.405862761338354D+01
 0.989228344469506D+02  0.418401782381424D+01
 0.103171527508039D+03  0.431420264929613D+01
 0.107552984977540D+03  0.444962515053656D+01
 0.112072690484128D+03  0.459078802263618D+01
 0.116736664673504D+03  0.473826464598930D+01
 0.121551542490953D+03  0.489271277966692D+01
 0.126524665796516D+03  0.505489168534040D+01
 0.131664195252120D+03  0.522568375594272D+01
 0.136979246686937D+03  0.540612213379728D+01
 0.142480058912162D+03  0.559742640184041D+01
 0.148178202455004D+03  0.580104932137644D+01
 0.154086842281799D+03  0.601873893878099D+01
 0.160221072870096D+03  0.625262247491437D+01
 0.166598351934054D+03  0.650532173517669D+01
 0.173239071334250D+03  0.678011521200777D+01
 0.180167323049032D+03  0.708117122025415D+01
 0.187411949676964D+03  0.741389244615305D+01
 0.195008022441533D+03  0.778544154841613D+01
 0.202998984195075D+03  0.820557347814596D+01
 0.211439870494836D+03  0.868801383996162D+01
 0.220402368151736D+03  0.925286973415579D+01
 0.229983206075680D+03  0.993114471840216D+01
 0.240319087055842D+03  0.107739736414647D+02
 0.251615879330500D+03  0.118738912465097D+02
 0.264213823883199D+03  0.134228858497264D+02
 0.278766733046005D+03  0.159197801616898D+02
 0.296966511995651D+03  0.214214542964372D+02    END*LAGR80*
-0.998771007252426D+00  0.315334605230584D-02    START*LEGD48*
-0.993530172266351D+00  0.732755390127626D-02
-0.984124583722827D+00  0.114772345792345D-01
-0.970591592546247D+00  0.155793157229438D-01
```

(INPUT DATA)

```
      -0.952987703160431D+00   0.196161604573555D-01
      -0.931386690706554D+00   0.235707608393244D-01
      -0.905879136715570D+00   0.274265097083569D-01
      -0.876572020274248D+00   0.311672278327981D-01
      -0.843588261624394D+00   0.347772225647704D-01
      -0.807066204029443D+00   0.382413510658307D-01
      -0.767159032515740D+00   0.415450829434647D-01
      -0.724034130923815D+00   0.446745608566943D-01
      -0.677872379632664D+00   0.476166584924905D-01
      -0.628867396776514D+00   0.503590355538545D-01
      -0.577224726083973D+00   0.528901894851937D-01
      -0.523160974722233D+00   0.551995036999842D-01
      -0.466902904750968D+00   0.572772921004032D-01
      -0.408686481990717D+00   0.591148396983956D-01
      -0.348755886292161D+00   0.607044391658939D-01
      -0.287362487355456D+00   0.620394231598927D-01
      -0.224763790394689D+00   0.631141922862540D-01
      -0.161222356068892D+00   0.639242385846482D-01
      -0.970046992094627D-01   0.644661644359501D-01
      -0.323801709628694D-01   0.647376968126839D-01
       0.323801709628694D-01   0.647376968126839D-01
       0.970046992094627D-01   0.644661644359501D-01
       0.161222356068892D+00   0.639242385846482D-01
       0.224763790394689D+00   0.631141922862540D-01
       0.287362487355456D+00   0.620394231598927D-01
       0.348755886292161D+00   0.607044391658939D-01
       0.408686481990717D+00   0.591148396983956D-01
       0.466902904750968D+00   0.572772921004032D-01
       0.523160974722233D+00   0.551995036999842D-01
       0.577224726083973D+00   0.528901894851937D-01
       0.628867396776514D+00   0.503590355538545D-01
       0.677872379632664D+00   0.476166584924905D-01
       0.724034130923815D+00   0.446745608566943D-01
       0.767159032515740D+00   0.415450829434647D-01
       0.807066204029443D+00   0.382413510658307D-01
       0.843588261624394D+00   0.347772225647704D-01
       0.876572020274248D+00   0.311672278327981D-01
       0.905879136715570D+00   0.274265097083569D-01
       0.931386690706554D+00   0.235707608393244D-01
       0.952987703160431D+00   0.196161604573555D-01
       0.970591592546247D+00   0.155793157229438D-01
       0.984124583722827D+00   0.114772345792345D-01
       0.993530172266351D+00   0.732755390127626D-02
       0.998771007252426D+00   0.315334605230584D-02        END*LEGD48*
      0.80  0.90  1.00  1.10  1.20  1.30  1.40  1.50            **R**
      1.60  1.70  1.75  1.80  1.85  1.90  1.95  2.00
      2.05  2.10  2.15  2.20  2.25  2.30  2.35  2.40
      2.45  2.50  2.55  2.60  2.65  2.70  2.75  2.80
      2.85  2.90  2.95  3.00  3.05  3.10  3.15  3.20
```

Bibliography

[1] D.O. Pederson and J.A. Brewer, Phys. Rev. **B16**, 4546 (1977).

[2] P. Eisenberger and P.S. Pershan, Phys. Rev. **167**, 292 (1968).

[3] J.D. Kingsley and J.S. Prenner, Phys. Rev. Letters **8**, 315 (1962).

[4] J.D. Kingsley and J.S. Prenner, J. Chem. Phys. **38**, 667 (1963).

[5] U. Piekara and J.M. Langer, solid State Commun. **23**, 583 (1977).

[6] J.M. Langer, T. Langer, G. Pearson, B. Krukowska-Fulde and U. Piekara, Phys. Stat. Sol. **B66**, 537 (1974).

[7] P.F. Weller, Inorg. Chem., **4**, 1545 (1965).

[8] F. Trautweiler, F. Moser and R.P. Khosla, J. Phys. Chem. Solids **29**, 1869 (1968).

[9] I. Kunze and V. Ulrici, Phys. Status Solidi **B55**, 567 (1973).

[10] J.E. Dmochowski, J.M. Langer, Z. Kalinski and W. Jantsch, Phys. Rev. Lett. **56**, 1735 (1986).

[11] J.E. Dmochowski, W. Jantsch, D. Dobosz and J.M. Langer, Acta Phys. Polon. **A73**, 247 (1988).

[12] T.M. Lee and F. Moser, Phys. Rev. **B3**, 347 (1971).

[13] J.E. Dmochowski, I. Kosachi and J.M. Langer Radiat. Eff. Def. Solids **72**, 139 (1983).

[14] Y. Shinozuka and Y. Toyozawa, J. Phys. Sco. Japan **46**, 505 (1979).

[15] Y. Toyozawa, Phsica **116B**, 7 (1983).

[16] J.E. Dmochowski, J.M. Langer and W. Jantsch, Shallow Impurities in Semiconductors 1988, Inst. Phys. Conf. Ser. No. 95, 325 (1989).

[17] J.D. Axe, Phys. Rev. **139**, A1215 (1965).

[18] M.J. Norgett, J. Phys. C: Solid State Phys. **4**, 298-306 and 1284-1298 (1971).

[19] R.G. Gordon and Y.S. Kim, J. Chem. Phys. **56**, 3122 (1972).

[20] M. Tovar, C.A. Ramos and C. Fainstein, Phys. Rev. **B28**, 4813 (1983).

[21] C.R.A. Catlow and M.R. Hayns, J. Phys. C: Solid State Phys. *5*, L237 (1972).

[22] R.J. Kimble Jr, P.J. Welcher, J.J. Fontanella, M.C. Wintersgill and C.G. Andeen, J. Phys. C: Solid State Phys. *15*, 3441 (1982).

[23] F.S. Gourary and F.J. Adrian, Phys. Rev. **105**, 1180 (1957).

[24] C.H. Leung, G. Brunet and K.S. Song, J. Phys. C: Solid State Phys. **18**, 4459 (1985).

[25] L. Emery, M.Sc. Thesis, University of Ottawa, (1983).

[26] K.S. Song, L. Emery, G. Brunet and C.H. Leung, Nucl. Instrum. Methods **B1**, 456 (1984).

[27] L. Emery, C.H. Leung and K.S. Song, J. Phys. C: Solid State Phys. **15**, L361 (1982).

[28] R.H. Bartran, A.M. Stoneham and D. Gash, Phys. Rev. **176**, 1014 (1968).

[29] R.D. Zwicker, Phys. Rev. **B18**, 2004 (1978).

[30] E. Clementi and C. Roetti, Atomic Data and Nuclear Data Tables **14**, 177 (1974).

[31] J.K. Kübler and R.J. Friauf, Phys. Rev. **A140**, 1742 (1965).

[32] J.C. Slater and G.F. Koster, Phys. Rev. **94**, 1498 (1954).

[33] C.E. Moore, Atomic Energy Levels, NSRDS-NBS (1971).

[34] B.S. Gourary and F.J. Adrian, Solid State Phys. **10**, 128-292 (1960).

[35] H. Fröhlich, Theory of Dielectries, Clarendon Press, Oxford (1949).

[36] C. Kittel, Introduction to Solid State Physics 5th ed., John Wiley and Sons Inc., New York (1976).

[37] J.R. Tessman, A.H. Kahn and W. Shockley, Phys. Rev. **92**, 890 (1953).

[38] L. Pauling, Prog. Roy. Soc. **A114**, 181 (1927).

[39] A.M. Stoneham, Clarendon Press, Oxford (1985)

[40] Y. Cai and K.S. Song, Radiat. Eff. Def. Solids, (in press).

[41] Y. Cai and K.S. Song, J. Phys. Condens. Matter **7**, 2275-2284 (1995).

[42] M. Jaros, Deep levels in Semiconductors, Adam Hilger Ltd, (1986).

[43] S. Bednarek and J. Admowski, Acta Phys. Polon. **A79**, 393 (1991).

[44] S. Bednarek and J. Admowski, Acta Phys. Polon. **A80**, 357 (1991).

[45] J.M. Langer, Lecture Notes in Physics **122**, 123 (1980).

[46] (see for example) G.N. Martin and S. Makram-Ebeid, Deep Centres in Semiconductors ed S T Pantelides (New York: Gordon and Breach) (1986).

[47] M. Saito, A. Oshiyama and O. Sugino, Phys. Rev. **B45**, 745 (1992).

[48] L. Hesselink and M.C. Bashaw, Optical and Quantum Elctronics **25**, S611 (1993).

[49] A.I. Ryskin, A.S. Shcheulin et al., (To be published).

[50] R.A. Linke, T. Thio, J.D. Chadi and G.E. Devlin, Appl. Phys. Lett. **65**, 16 (1994).

[51] R.T. Williams and K.S. Song, J. Phys. Chem. Solids **51**, 679 (1990).

[52] see *DIETIV*, (Springer, Berlin, 1990) J. Phys. Chem. Solids **51**, 679 (1990).

[53] P.D. Townsend, R. Browning, D.J. Garland, J.C. Kelly, A. Mahjoobi, A.J. Michael and M. Saidoh, Radiat. Eff. Def. Solids **E30**, 55 (1976).

[54] D. Menzel and R. Gomer, J. Chem. Phys. **41**, 3311 (1964).

[55] P.A. Redhead, Can. J. Phys. **43**, 886 (1964).

[56] P.D. Townsend, in Sputtering by Partical bombardment II, ed. R. Behrisch (Springer, Berlin), 147 (1983).

[57] D. Pooley, Proc. Phys. Sco. (London) **87**, 245 (1966).

[58] H.N. Hersh, Phys. Rev. **148**, 928 (1966).

[59] K.S. Song and R.T. Williams, Self-Trapped Excitons (Springer Sr. Solid St. Sc. **105**, Heidelberg, (1993)).

[60] P.D. Townsend and J.C. Kelly, Phys. Lett. **A26**, 138 (1968).

[61] P.W. Palmberg and T.N. Rhodin, J. Phys. Chem. Sol. **29**, 1917 (1968).

[62] A. Schmid, P. Braunlich and P.K. Rol Phys. Rev. Lett. **35**, 1382 (1975).

[63] H. Overeijnder, M. Szymonski and de A.E. Vries, Radiat. Eff. **36**, 63 (1978).

[64] H. Overeijnder, M. Szymonski and de A.E. Vries, Radiat. Eff. Def. Solids **38**, 21 (1978).

[65] Z. Postawa and M. Szymonski, Phys. Rev. **B39**, 12950 (1989).

[66] Z. Postawa, P. Czuba, A. Poradzisz and M. Szymonski, Radiat. Eff. Def. Solids **109**, 189 (1989).

[67] M. Szymonski, J. Kolodziej, P. Czuba, P. Piatkowski, A. Poradzisz, N.H. Tolk and J. Fine, Phys. Rev. Lett. **67**, 1906 (1991).

[68] J. Kolodziej, P. Czuba, P. Piatkowski, A. Poradzisz, Z. Postawa, M. Szymonski and J. Fine, Nucl. Instr. Methods **B65**, 507 (1992).

[69] M. Szymonski, J. Kolodziej, P. Czuba, P. Piatkowski, N.H. Tolk and J. Fine, Phys. Rev. Lett. **67**, 1906 (1994).

[70] Z. Postawa, J. Kolodziej, P. Czuba, P. Piatkowski, M. Szymonski, E. Bielanska, J. Camra, T. Ciach, M. Faryna and A. Rakowska, Nucl. Instr. Methods **B78**, 314 (1993).

[71] N.H. Tolk, M.M. Traum, J.S. Kraus, T.R. Pian, W.E. Collins, N.G. Stoffel and G. Margaritondo, Phys. Rev. Lett. **49**, 812 (1982).

[72] N.H. Tolk, L.C. Feldman, J.S. Kraus, R.J. Morris, M.M. Traum and J.C. Tully, Phys. Rev. Lett. **46**, 134 (1981).

[73] R.E. Walkup, Ph. Avouris and A.P. Ghosh, Phys. Rev. Lett. **57**, 2227 (1986).

[74] Z. Postawa, J. Rutkowski, A. Poradzisz, P. Czuba and M. Szymonski, Nucl. Instr. Methods **B18**, 574 (1987).

[75] S. Hirose and M. Kamada, J. Phys. Soc. Japan Vol.**60**, 4374-4381 (1991).

[76] S. Hirose and M. Kamada, Phys. Rev. **B48**, 17641 (1993).

[77] L.F. Chen, Y. Cai and K.S. Song, Nucl. Instr. Methods **B91**, 614 (1994).

[78] E. Metthias, S. Gogoll, E. Stenzel and M. Reichling, Radiat. Eff. Def. Solids **128** 67, (1994).

[79] M. Reichling, Radiat. Eff. Def. Solids **128** 55, (1994).

[80] M.N. Kabler, Phys. Rev. **A136**, 1296 (1964).

[81] K.S. Song, A.M. Stoneham and A.H. Harker, J. Phys. Solid St. **C8**, 1125 (1975).

[82] A.M. Stoneham J. Phys. Solid St. **C7**, 2426 (1974).

[83] N. Itoh, A.M. Stoneham and A.H. Harker, J. Phys. Solid St. **C10**, 4197 (1977).

[84] M.N. Kabler and D.A. Patterson, Phys. Rev. Lett. **19** 652 (1967).

[85] G. Brunet, C.H. Leung and K.S. Song, Int'l. Conf. Defects in Insulating Crystals (Univ. Utah, Salt Lake City 1984) Abstracts, p. 51.

[86] G. Brunet, C.H. Leung and K.S. Song, Solid State Commun. **53**, 607 (1985).

[87] R.C. Baetzold and K.S. Song, J. Phys.: Condens. Matter **3**, 2499 (1991).

[88] K.S. Song and R.C. Baetzold, Phys. Rev. B **46**, 1960 (1992).

[89] A.L. Shluger, N. Itoh, V.E. Puchin and E.N. Heifets, Phys. Rev. B **44**, 1499 (1991).

[90] A.L. Shluger, R.W. Grimes and C.R.A. Catlow, J. Phys.: Condens. Matter **3**, 3125 (1991).

[91] K.S. Song, C.H. Leung and R.T. Williams J. Phys.: Condens. Matter **1**, 683 (1989).

[92] K.S. Song and Y. Kayanuma, Butsuri (Jpn) **45**, 469 (1990).

[93] H. Rabin and C.C. Klick, Phys. Rev. **117**, 1005 (1960).

[94] K. Kan'no, K. Tanaka and T. Hayashi, Rev. Solid St. Sc. **4** 383, (1990).

[95] K.S. Song and L.F. Chend, J. Phys. Soc. Japan **58**, 3022 (1989).

[96] R.T. Williams, H. Liu, G.P. Williams Jr. and K.J. Platt, Phys. Rev. Lett. **66**, 2140 (1991).

[97] M. Itoh, S. Hashimoto and N. Ohno, J. Phys. Soc. Japan **60**, 4357 (1989).

[98] P.D. Townsend, J. Phys. Solid St. **C6**, 961 (1973).

[99] Quantum Mechanical Cluster Calculations in Solid State Studies (ed. R.W. Grimes, C.R.A. Catlow and A.L. Shluger, World Scientific Pub. Singapore, 1992).

[100] K. Tanimura, T. Suzuki and N. Itoh, Phys. Rev. Lett. **68**, 635 (1992). T. Suzuki, K. Tanimura and N. Itoh (to be published).

[101] T. Tokizaki et al., Phys. Rev. Lett. **67**, 2701 (1991).

[102] V.I. Puchin, A.L. Shluger, K. Tanimura and N. Itoh, Phys. Rev. **B47**, 6226 (1993).

[103] K.S. Song, R.C. Baetzold and F. Kong, Nucl. Instr. Methods **B91**, 183 (1994).

[104] T. Suzuki et al., unpublished.

[105] W. Meise, U. Rogulis, F.K. Koschnik, K.S. Song and J.-M. Spaeth, J. Phys. Cond. Matter **6** 1815 (1994).

[106] M.P. Tosi, Solid State Phys. **16**, (Academic, New York 1964).

[107] N.F. Mott and M.J. Littleton, Trans. Faraday Soc. **34**, 485 (1938).

[108] M. Adair, M.Sc. Thesis, University of Ottawa (1986)

[109] T.L. Gilbert and A.C. Wahl, J. Chem. Phys. **55**, 5247 (1971).

[110] J.A. Pople and D.L. Bevevidge, Approximate Molecular Orbital Theory (New York: McGraw Hill 1970).

[111] Y. Cai and K.S. Song, Nucl. Instr. Methods **101**, 115 (1995).

[112] M. Szymonski, Desorption Induced by Electronic Transitions, ed. G. Betz and P. Varge, p.270 (Springer-Verlag, Berlin, 1990).

[113] P. POstawa, J. Kolodziej, G. Baran, P. Czuba, P. Piatkowski, M. Szymonski, I. Plavina and A. Popov, Nucl. Instr. Methods **B100**, 229 (1995).

[114] J. Kolodziej, Z. Postawa, P. Czuba, P. Piatkowski and M. Szymonski, Radiat. Eff. Def. Solids **128**, 47 (1994).

[115] K.S. Song and L.F. Chen, Radiat. Eff. Def. Solids **128**, 35 (1994).

[116] I. Shavitt, Method in Computational Physics Vol.2, (1963).

[117] J.E. Lösch, Tables of Higher Functions, 6th ed. McGraw-Hill Book Comp. Inc. (1960).

[118] J. Callaway, Quantum Theory of the Solid State Part A, Academic Press, (1974).

[119] K. Fukui and T. Yamabe, Intern. J. Quantum Chem. **2**, 359 (1968).

[120] G. Arfken, Mathematical Methods for Physicists 2nd ed., Academic press, (1985).